



Diploma Thesis

Electromagnetic Design Study for a 15 T Large Bore Superconducting Dipole Magnet

Nikolai Schwerg

Berlin, November 2005

Supervisors:

- **Dr.-Ing. Christine Völlinger**
AT-MAS-MA-group, CERN European Organization for Nuclear Research, Geneva, Switzerland
- **Dr. Arnaud Devred**
AT-MAS-MA-group, CERN European Organization for Nuclear Research, Geneva, Switzerland
- **Prof. Dr.-Ing. Heino Henke**
Institute for Technical Computer Science and Microelectronics,
Department of Theoretical Electrical Engineering,
Technische Universität Berlin, Berlin, Germany

Abstract

In the framework of research and development (R&D) activities at CERN the Next European Dipole (NED) program is one which is dedicated to the development of a high-field dipole magnet using Nb_3Sn superconductors. Part of the NED activities is a design study of different possible dipole configurations which is shared amongst the collaborating institutes [1]. This thesis covers the electromagnetic design study of an 88 mm large bore superconducting 15 T dipole magnet with a coil cross section in $\cos\theta$ -layer design.

Based on analytically describable geometries the sources of multipole errors are studied and elementary estimations of the magnet are carried out, *e.g.*, the required amount of superconductors or the influence of the iron yoke thickness on the field quality.

The magnet cross section for NED is optimized by means of the CERN field computation program ROXIE [2, 3]. The preliminary NED design [4] serves as starting point for the coil cross section optimization with respect to field quality and a radial positioning of the conductor blocks. Due to the high field of magnetic induction, the surrounding iron yoke saturates for high transport currents and the multipole errors vary with excitation. In order to reduce the variation, modifications of the iron yoke shape are studied, like, *e.g.*, holes punched into the yoke laminations, a change of the outer yoke contour or an inner contour of elliptical shape. For an elliptically shaped inner iron yoke contour the coil cross section is again optimized resulting in the Reference Design V. 2 for the NED collaboration.

The persistent current induced field errors are estimated for the present design and NED cable. Based on these results different compensation methods [5] are investigated including ferromagnetic shims inside the cables, mounted on the cold bore tube or on the copper wedges.

Zusammenfassung

in deutscher Sprache

Das Next European Dipole (NED) Programm dient der weiteren Erforschung von Nb₃Sn-Kabeln für die Herstellung von supraleitenden Hochfeldmagneten in Teilchenbeschleunigern. Es ist Teil der Forschungs- und Entwicklungsaktivitäten am CERN. Das NED Programm beinhaltet u.a. eine Studie unterschiedlicher Dipolkonzepte, die unter den mitwirkenden europäischen Instituten aufgeteilt wurde [1]. Diese Arbeit behandelt die elektromagnetische Designstudie eines supraleitenden 15 T Dipolmagnets mit grosser 88 mm Apertur. Dabei wurde das so genannte $\cos \theta$ -layer Design untersucht.

Vorbereitend werden mit einfachen, analytisch beschreibbaren Geometrien die Ursachen für so genannte Multipolfehler theoretisch aufgezeigt und einfache Abschätzungen für den Magneten vorgenommen: Anhand der idealen Anordnung zweier sich überschneidender Kreise wird die minimale Anzahl supraleitender Kabel zur Erreichung einer gewünschten Feldstärke für eine vorgegebene Apertur unter Einbeziehung der Kabeleigenschaften hergeleitet. Aus der allgemeinen Lösung einer ebenen, zylindersymmetrischen dreischichtigen Materialanordnung mit exzentrischem Linienstrom werden das Spiegelungsverfahren am zylindrischen Halbraum und dessen Gültigkeitsbereich hinsichtlich Mindestjochdicke und Sättigungsstrom hergeleitet.

Die Berechnung und Optimierung des Magneten erfolgt lediglich in der Ebene und wird mit Hilfe des CERN Feldberechnungsprogramms ROXIE [2, 3] durchgeführt. Als Ausgangspunkt für die Optimierung der Spulengeometrie dient hierbei ein vorläufiges Design [4], das schrittweise hinsichtlich Feldqualität und radialer Ausrichtung der Leiter verbessert wird.

Die Schwankung der Feldqualität bei variierendem Anregungsstrom wird durch die Anpassung der Form des Eisenjochs reduziert. Vorab werden verschiedene Ansätze, wie die Modifizierung der äusseren und inneren Jochkontur sowie das Stanzen von Löchern in die Eisenlaminierungen untersucht. Für die endgültige Form des Eisenjochs mit elliptischer innerer Kontur wird die Spulengeometrie reoptimiert. Dieses Design wird im weiteren Verlauf des NED-Projekts als Referenzdesign V. 2 dienen.

Die durch die Supraleitermagnetisierung hervorgerufenen Feldfehler werden für das verwendete Kabel und Design berechnet und zeigen für variierenden Strom eine Hysterese. Für den Einsatz des Magneten in einem Teilchenbeschleuniger muss die Schwankung der Feldfehler für ansteigenden Strom und Feld so gering wie möglich sein. Die Kompensation mit ferromagnetischen Plättchen innerhalb des Kabels, auf dem Strahlrohr oder zwischen den Leiterblöcken [5] wird demonstriert.

Eidesstattliche Erklärung

Die selbständige und eigenständige Anfertigung versichert an Eides statt.

Berlin, den 30.10.2005

Nikolai Schwerg

Acknowledgement

The work presented in this thesis has been carried out in the framework of the Technical Student Program at CERN in the AT-MAS group and of the NED joint research activity of CARE.

I am most grateful to my supervisor at CERN, Dr.-Ing. Christine Völlinger for giving me the opportunity to carry out this thesis work and for her outstanding support. By being always available for discussions, by sharing her professional experience and by including me into her work, she created a very pleasant and fruitful working atmosphere encouraging me to push my limits. Thanks to her, I am leaving CERN after completion of my internship, the student research project and my diploma thesis as well as with plenty of experience of presentations, conferences and publications.

I wish her and her family all the best for the future. I hope we will get again an opportunity to work together.

I want to thank Dr. Arnaud Devred from CEA and CERN for including me into the NED activities and for giving me plenty of advice for proper scientific working.

I would further like to express how much I appreciated to work with all the collaborators of the NED WGMDO.

I wish to give acknowledgements to Dr.-Ing. habil. Stephan Russenschuck from CERN for his help with the simulation program ROXIE. I got a lot of inspiration from our discussions on electromagnetic field theory and mathematics.

I very much appreciated the work in the AT-MAS group and want to thank all my colleagues for the pleasant atmosphere during my stay.

I like to thank Prof. Dr.-Ing. Heino Henke from the Technical University of Berlin for supervising this thesis and for being available for discussions in Berlin as well as on his visits to CERN.

Further I want to express my gratitude to Dr.-Ing. Manfred Filtz from the Technical University of Berlin for his willingness to be ready to listen to my ideas.

I thank my family for their unlimited support and help during my stay in Geneva. At last I thank my love Jelena not only standing the separation but encouraging me to take the opportunity to work at CERN.

Contents

List of Figures	xv
-----------------	----

List of Tables	xvii
----------------	------

1	Introduction	1
1.1	Next European Dipole	1
1.2	Basics on Superconductivity for Accelerator Magnets	2
1.2.1	Critical Current Density	2
1.2.2	Quench	3
1.3	Basic Layout of a Superconducting Magnet	4
1.4	Coil Cross Section Optimization	6
1.5	Objective of this Thesis	7
2	Specifications for the NED Magnet	9
2.1	Coil Cross Section	9
2.1.1	Cables	10
2.1.2	Wedges	12
2.1.3	Insulations	12
2.2	The Magnet Cross Section	13
2.2.1	Collar	13
2.2.2	Iron Yoke	14
2.3	Material properties	14
2.3.1	Critical Current Density	14
2.3.2	Thermal Contraction Factor	14
2.3.3	Permeability	16
2.4	Stress/Forces	17
2.5	Electromagnetic Properties	18
2.5.1	Operation Point	18
2.5.2	Reference Radius	19
3	Multipole Errors	21
3.1	Multipole Expansion	21
3.2	Multipole Error of a Single Line Current	22
3.3	Effect of Symmetries	24
3.4	Sensitivity of the Multipole Errors	26

3.5	Scaling of Multipole Errors to Different Reference Radii	27
3.6	Good-Field-Radius	29
3.7	Field Error of a Magnetic Line Dipole	29
3.8	Summary	32
4	Analytic Descriptions of the Current Distribution	33
4.1	Line Current	33
4.1.1	Fourier Expansion of the Vector Potential \mathbf{A}_l	34
	Fourier Expansion for $\rho < \rho_0$	34
	Fourier Expansion for $\rho > \rho_0$	35
4.1.2	Continuity of Both Approaches at the Boundary	35
4.2	Ideal Geometries	36
4.2.1	Cos($n\theta$)-Geometry	36
	Current Sheet	36
	Ideal Dipole of Finite Thickness	38
4.2.2	Intersecting Circles	39
	Circle of Homogeneous Current Density	40
	Two Intersecting Circles	40
4.3	Analytic Calculation of a Current Shell	42
4.3.1	Current Arc	43
4.3.2	Symmetric Current Shell	45
4.3.3	The No- B_3 -No- B_5 -Coil	46
4.4	Required Amount of Superconductors for High-field Accelerator Magnets .	47
4.4.1	Analytical Model	48
4.4.2	Graphical Solution	51
4.4.3	Estimation for NED	51
4.4.4	Sensitivity	53
4.4.5	Influence of the Iron Yoke	53
4.5	Summary	54
5	Analytic Models of the Iron Yoke	55
5.1	Circular Hollow Cylinder - Three Arbitrary Materials	55
5.1.1	Potential Approach	56
5.1.2	Field of Magnetic Induction	57
5.1.3	Fulfilling the Boundary Conditions	58
5.1.4	Resulting Vector Potential	60
5.2	Permeable Bore	61
5.2.1	Imaging Method for a Single Line Current	62
5.2.2	Material with Infinite Permeability	63
5.2.3	Saturation Current	65
5.2.4	Effect on Multipole Errors	67
5.3	Permeable Pipe	69
5.3.1	Effect on Multipole Errors	71

5.3.2	Stray Field of a Coil	72
5.4	Influence of the Steel Collar	74
5.5	Conclusions	76
6	Optimization of the Coil Cross Section	79
6.1	Optimization Process	79
6.1.1	Excitation Current	79
6.1.2	Optimization Goals	79
6.1.3	Numerical Optimization	80
6.1.4	Limit Control	80
6.1.5	Additional Properties	81
6.2	Preliminary Design	81
6.3	Resulting Coil Cross Section A	83
6.4	Resulting Coil Cross Section C	85
7	Optimization of the Iron Yoke	87
7.1	Effect of the Iron Saturation	87
7.2	Optimization Goals	90
7.3	Model of the Iron Yoke Saturation	92
7.4	Study of Different Approaches	94
7.4.1	Variation of the Outer Yoke Radius	94
7.4.2	Variation of the Outer Yoke Contour: Cut Off	96
7.4.3	Introducing Holes in the Yoke Laminations	99
7.4.4	Variation of the Inner Yoke Contour: Ellipse	103
7.5	Final Iron Yoke Shape and Optimized Coil Cross Section	104
7.6	Conclusions	108
8	Study of Persistent Current Compensation Methods	109
8.1	Effect of the Superconductor Magnetization	109
8.2	Basic Idea of Compensation	111
8.3	Model for the Contribution of Ferromagnetic Elements	112
8.3.1	Magnetic Moment of a Thin Ferromagnetic Cylinder	113
8.3.2	Multipole Contribution	113
8.4	Study of Different Approaches	114
8.4.1	Ferromagnetic Shims in Cables	115
8.4.2	Shims on Cold Bore Tube	117
8.4.3	Shims on Wedges	118
8.5	Conclusions	119
9	Conclusions	123
9.1	Analytical Results	123
9.2	Estimations	124
9.3	Numerical Results	124

9.4 Outlook	125
Bibliography	127
A Theoretical Excursions	131
A.1 Cylindrical/Polar Coordinate System	131
A.2 Magnetic Vectorpotential \mathbf{A}	132
B Values and Constants	135
B.1 Linear Approximation of the Critical Current Density for LHC	135
B.2 Scaled Allowed Multipole Errors for LHC	135
C ROXIE	137
C.1 Double Bending Fit Function	137
C.2 Added: Radial Constrain	137
C.3 Added: Good Field Radius	138
D ROXIE Input Files	139
D.1 BH-Curve	139
D.2 Cable Definition	140

List of Figures

1.1	Critical surface of NbTi strands of the LHC main bending magnets. . . .	3
1.2	Layout of the LHC main bending magnets.	5
1.3	Formation of a coil for a magnet with circular bore	6
2.1	Sketches of the keystoneed Rutherford-type cable for NED.	10
2.2	Sketch of the magnet cross section.	13
2.3	Critical current density in the non-copper area of the NED strands. . . .	15
2.4	Magnetic properties of the permeable material used for the iron yoke. . . .	17
2.5	Example and definition of the margin on the load line.	19
3.1	Ideal multipole magnets and corresponding current distribution.	23
3.2	Decrease of the multipole errors with increasing order.	24
3.3	Positions and symmetries of line currents.	25
3.4	Example for the sensitivity of the multipole errors on the position.	27
3.5	Diagram of the sensitivity of the multipole errors on the position.	28
3.6	Demonstration of the good-field-radius.	30
3.7	Geometry of a magnetic line dipole.	31
4.1	Geometry and field distribution of one arbitrary line current.	33
4.2	Geometry of an ideal $\cos \theta$ -dipole.	37
4.3	Field plot for some lower order $\cos(n\theta)$ current sheets.	38
4.4	Field plot for an ideal $\cos \theta$ dipole.	40
4.5	Geometry of two intersecting circles.	41
4.6	Field plot for an ideal dipole made of two intersecting circles.	42
4.7	Geometry of a current shell.	43
4.8	Field plot for current arcs with varying opening angles.	45
4.9	Field plot for symmetric current shells with varying opening angles. . . .	46
4.10	Field plot for the No- B_3 -No- B_5 -dipole.	47
4.11	Ideal dipole geometry of two intersecting circles.	48
4.12	Sketch for the calculation of the surface of two intersecting circles.	50
4.13	Graphical solution for the minimum amount of superconductors.	52
5.1	Geometry of a circular hollow cylinder with three different materials. . . .	55
5.2	Graph of α_{nm} and β_{nm} for different permeabilities.	60
5.3	Geometry of a single line current in a bore of permeable material.	61
5.4	Field plot of a line current inside a bore within permeable material.	63

List of Figures

5.5	Permeable bore: Definition of the angle of the field lines.	64
5.6	Permeable bore: Calculated angle of the field lines.	65
5.7	Estimation of the saturation ampere turns.	67
5.8	Infinitely permeable bore: Multipole errors versus inner bore radius.	68
5.9	Geometry of a single line current inside a permeable pipe.	69
5.10	Field plot of the magnetic induction for a pipe of permeable material.	71
5.11	Influence of the pipe thickness on the multipole errors.	72
5.12	Field plot of a coil inside a permeable pipe.	74
5.13	Stray field for different permeabilities and distances.	75
5.14	Influence of the collar on the multipole errors.	76
6.1	Coil cross section layout of the preliminary design.	82
6.2	Coil cross section layout A.	84
6.3	Coil cross section layout C.	86
7.1	CCS A with circular iron yoke: Main field and multipole variation.	88
7.2	CCS A with circular iron yoke: Variation of the relative permeability.	89
7.3	CCS A with circular iron yoke: Iron contribution to the main field.	90
7.4	CCS A with circular iron yoke: Good-field-radius	91
7.5	CCS A with circular iron yoke: Saturation history.	92
7.6	Saturation history in context of the source of multipole errors.	94
7.7	Study: Variation of the outer yoke radius.	95
7.8	Study: Cut off above the outer yoke contour.	97
7.9	Study: Cut off at the side of the outer yoke contour.	98
7.10	Definition of the hole punched into the iron yoke laminations.	99
7.11	Study: Angular sensitivitiy of punched holes.	100
7.12	Study: Radial sensitivitiy of punched holes.	101
7.13	Study: Sensitivitiy on the size of punched holes.	102
7.14	Study: Elliptical inner yoke contour.	103
7.15	CCS C with elliptical iron yoke.	105
7.16	CCS C with elliptical iron yoke: Main field and multipole variation.	106
7.17	CCS C with elliptical iron yoke: Good-field-radius.	107
8.1	CCS C with elliptical iron yoke: Persistent current induced field errors.	110
8.2	Comparison: Geometrical value and persistent currents.	112
8.3	CCS C: Analytical calculation of the field of magnetic induction.	114
8.4	Sensitivity of rel. multip. errors on position of a thin ferromag. rod.	115
8.5	CCS C with elliptical yoke: Shims in cable.	116
8.6	CCS C with elliptical yoke: Shim on CBT.	117
8.7	CCS C with elliptical yoke: Shims on copper wedges.	119
8.8	CCS C with elliptical iron yoke: Compensated pc. induced field errors.	121

List of Tables

2.1	Salient cable parameters for NED.	11
2.2	Salient parameters for the NED strands and filaments.	11
2.3	Cross sectional areas and conversion factors for NED.	12
2.4	Salient specified radii for the 88 mm NED magnet.	14
2.5	Fit parameters for the critical current density.	15
2.6	Integrated thermal contraction factors for NED.	16
2.7	Reference radii for the multipole expansion.	19
3.1	Effects of symmetries/asymmetries on certain multipole errors.	26
4.1	Minimum number of strands for a 15 T dipole made of NED strands. . . .	51
4.2	Minimum number of conductors for a 15 T dipole made of NED cables. . .	53
4.3	Sensitivity of the estimated number of conductors.	53
5.1	Added multipole error for a bore in infinitely permeable material.	69
6.1	Preliminary design: Salient parameters	82
6.2	Preliminary design: Relative multipole errors	82
6.3	CCS A: Salient parameters	84
6.4	CCS A: Relative multipole errors	84
6.5	CCS C: Salient parameters	86
6.6	CCS C: Relative multipole errors	86
7.1	CCS A: Variation of the multipoles (uncompensated).	89
7.2	CCS C with elliptical iron yoke: Salient parameter.	105
7.3	CCS C with elliptical iron yoke: Relative multipole errors.	105
7.4	CCS C with elliptical iron yoke: Variation of the multipoles.	106
8.1	CCS C with elliptical iron yoke: Multip. var. due to sc. magnetization. . .	111
8.2	CCS C with elliptical iron yoke: Multip. var. due to sc. magnetization. . .	118
B.1	High field approximation for the critical current density for LHC.	135
B.2	LHC multipole target values scaled for NED.	136
C.1	Constants used in ROXIE and the fit constants of the double bending fit. .	137

1 Introduction

In the framework of research and development (R&D) activities at CERN¹ the Next European Dipole (NED) program is one which is dedicated to the development of a high-field dipole magnet using Nb₃Sn superconductors.

Part of the NED activities is a design study of different possible dipole configurations which is shared amongst the collaborating institutes. This thesis covers the electromagnetic design study of an 88 mm large bore superconducting 15 T dipole magnet with a coil cross section in $\cos \theta$ -layer design.

1.1 Next European Dipole

For the last 30 years, superconducting magnet technology has been instrumental in the development of large particle accelerators for high energy physics. Up to now, all superconducting magnets installed in accelerators rely on NbTi conductors, whose transport-current and magnetization properties are well mastered and can be optimized and modified to achieve the high field homogeneity (of the order of 10 ppm) required for this application. The most advanced example is the Large Hadron Collider (LHC) now under construction at CERN, which will require of the order of 2000 superconducting dipole and quadrupole magnets, whose industrial production is near completion [6, 7].

The LHC superconducting magnet R&D program was successful in developing the magnets needed for this machine but it also demonstrated that the limit of what could be achieved with NbTi is reached. Hence, to go beyond LHC magnet performances and prepare for the future, a change of superconductor is necessary. The only other superconducting material that is at a mature enough state for the use in high field (10 \rightarrow 15 T range) environment while showing a high-current density (a few 100 A/mm² overall) is the inter-metallic compound Nb₃Sn. Nb₃Sn has a critical temperature and an upper critical field which are about twice those of NbTi, but it is more difficult to manufacture, and, once formed, it becomes brittle and strain sensitive. Furthermore, its magnetization properties are far less known and can result in field distortions which are one or two orders of magnitude bigger than for NbTi. Hence, designing and building Nb₃Sn accelerator-class magnets require a complete rethinking of the concepts and processes applied to NbTi magnets [6].

An EU-funded program, referred to as the Next European Dipole (NED), has been launched in 2004 to promote, in collaboration with European industries, the development of high performance Nb₃Sn conductors and study the feasibility of such magnets. The NED

¹Organisation Europeen pour la Recherche Nucleaire

program is supported by a consortium of 7 majors institutes and universities throughout Europe, led by CEA², in France, and CERN [1].

The NED program is divided into two phases: The first phase, fully funded through CARE³, encompasses three main work packages: Thermal studies and quench protection, conductor development and insulation development & implementation. It also includes a working group on magnet design and optimization (WGMDO). The Nb₃Sn conductor development will be carried through industrial sub-contracts and is aimed at a non-copper critical current density of 1500 A/mm² at 4.2 K and 15 T. The second phase of the NED program, for which funding is not yet secured, groups together all the tasks related to the detailed design, manufacturing and test of the model magnet [1].

The aim of this study done by the WGMDO⁴ is to optimize the design of high-field dipole magnets for particle accelerators, taking into account both technical and economical criteria. For the time being, the focus is on Nb₃Sn technology, but the results may also be useful for other brittle superconductors. A number of magnet configurations has been selected as candidates, including classical and novel arrangements such as: layer-type and slot-type $\cos\theta$, window-frame, common coil, motor-type, double helix, slotted dipole and ellipse-type racetrack [1].

The large aperture diameters for the study of 88 mm, 130 mm and 160 mm have been chosen according to a possible LHC interaction regions (IR) upgrade or an upgrade of the CERN cable test facility MFRESCA which is presently limited to 10 T.

1.2 Basics on Superconductivity for Accelerator Magnets

Within this thesis superconductivity and superconducting cables are mostly considered by some crucial values and reduced models only. For this reason no explanation of the physical background of superconductivity in accelerator magnets is given. Only the idea of the so-called critical surface will be sketched since it is limiting the magnet performance. In addition, the quench behavior and its implication will be mentioned. For a detailed explanation of superconductivity it is referred to [8] and for accelerator applications of superconductors to [9].

1.2.1 Critical Current Density

The capability of superconductors to carry currents is limited. The maximum current density in a superconductor decreases with increasing temperature, magnetic flux density and strain. The upper limit of these three quantities is mainly depending on the used superconducting material.

²Commissariat à l'Energie Atomique

³Collaborated Accelerator Research in Europe

⁴The working group on magnet design and optimization is made up of representatives from CCLRC, CEA, CERN, and CIEMAT.

Assuming a constant strain for the superconducting strands as well as for the superconducting cables inside the magnet during operation, the maximum current density can be expressed by means of a two dimensional function of magnetic flux density B and temperature T . It depends on the used material but also on the production process of the superconducting strands and cables.

The maximum current density is denoted as the critical current density since any further increase of any of the three quantities causes a quench. The set of all critical points gives the so-called critical surface shown in fig. 1.1. For a magnet which is operated at a constant

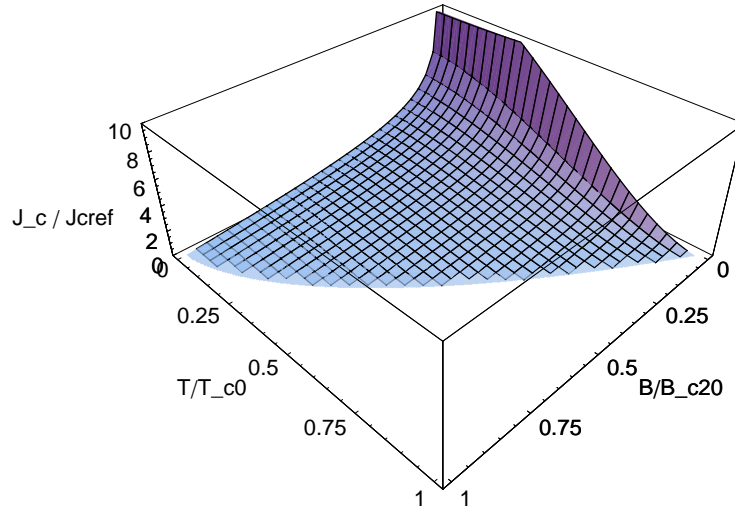


Figure 1.1: Critical surface of NbTi strands of the LHC main bending magnets.

temperature this can be further simplified to a function of critical current density versus magnetic induction $J_c(B)$.

1.2.2 Quench

The so-called quench denotes the sudden transition of the superconductor from superconducting to normally conducting state. The resistivity changes from a few femto ohm to values greater than the one of copper.

A quench is triggered when the working point exceeds the critical surface, *e.g.*, due to a rise of temperature. The temperature can be risen by additional heat created, *e.g.*, by the friction in case of an unwanted conductor movement.

The quench starts very locally and causes a turn of the current flow from the superconducting part to the copper area of the strand. Due to the higher resistivity, ohmic heating is induced. If the additional heat energy cannot immediately be transported away by the cooling system, the quench starts to propagate⁵. The heating increases the temperature in

⁵If the heat energy is small enough the strand can recover and return to superconducting state [10].

neighboring strands and cables and more and more strands quench. The complete magnet transits to normal conducting state.

For the operation and construction of superconducting magnets it is important to emphasize that a quench is an unwanted but also inevitable *modus operandi*. The design of a superconducting magnet includes always a quench protection system which prevents any permanent damage coming from a quench.

The quench starts in a very small area first. The voltage drop across the magnet begins to rise and the magnetic energy starts to discharge. The very high energy density in the quenching area can cause melting or even evaporation of the conductor material. Therefore, it is tried to spread the quench as fast as possible across the whole magnet. This is done passively by a close vicinity of the strands and the high thermal conductivity of the copper parts as well as actively by so-called quench heater creating additional heat after detecting a quench. At the same time the stored energy is discharged over a free wheeling diode.

1.3 Basic Layout of a Superconducting Magnet

Before the specifications of the different parts of the magnet are given, the basic layout of a superconducting magnet shall be explained. Since the NED magnet is still in the design phase, no specific details or drawings are available for the layout except from basic specifications (as shown in chapter 2). For this reason the fundamental layout is explained by means of the LHC main bending magnets. The studied design of a $\cos\theta$ -layer magnet in its general layout will be similar although the NED magnet is a single aperture magnet contrary to the double aperture LHC magnets.

Superconducting magnets consist of a superconducting coil around the so-called aperture, a collar of non magnetic material, a surrounding iron yoke and a container cylinder. The cross section of the LHC main bending magnets is shown in fig. 1.2. The relevant parts are denoted and will be explained in the following.

The aperture defines the space where the magnetic field can be used for experiments or to bend particles on a circular trajectory as in the LHC main bending magnets. Therefore, *e.g.*, a so-called beam pipe for the vacuum and a beam screen are inserted. The size of the aperture is given by the inner coil diameter and is very small compared to the length of the magnet. Thus most analytic calculations can be carried out for the cross section only.

The superconducting coil consists of an upper and a lower pole which are typically race-track type coils mounted below and above the aperture as shown in fig. 1.3 a). By reducing the distance of the windings to the aperture the efficiency and the magnetic main field can be increased. The windings are therefore pressed on a winding mandrel and the coil shape shown in fig. 1.3 b) is obtained. In order to leave space for the beam pipe, the coil ends are bent up/down and exposed to additional stress⁶.

Contrary to normal conducting magnets where the field quality depends on the shape of the iron poles, the quality of the magnetic field inside the aperture of a superconducting

⁶The coil end design including stress management, spacer design and multipole error correction is going to be studied after completion of the coil cross sectional design.

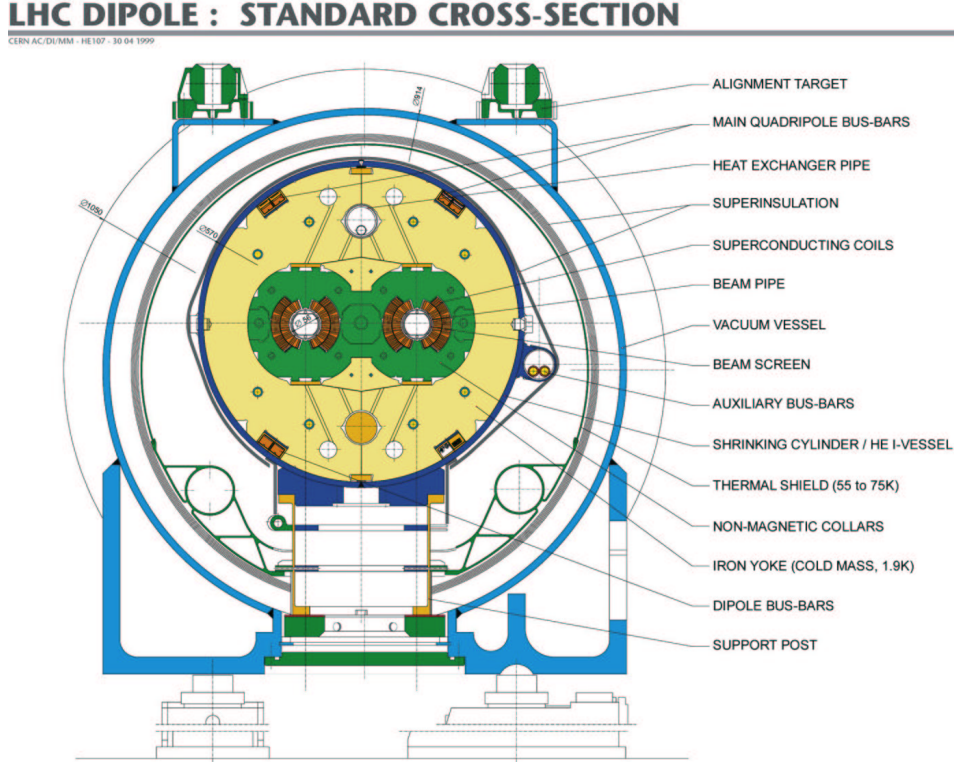


Figure 1.2: The layout of the LHC main bending magnets. All fundamental parts as the superconducting coil, the collar and the iron yoke are indicated (©CERN).

magnet depends mainly on the position of the conductors. For a dipole of $\cos\theta$ -layer design the windings are combined to blocks of different size which are distributed around the aperture in order to approximate an ideal $\cos\theta$ configuration. The space between two adjacent blocks is filled with non-magnetic material in order to hold the conductors in their positions and to improve the circular shape approximation. The field of the magnet is further increased by nesting two constructions like this - so called layers.

In between the two layers and on the outer contour of the coil, protection sheets are inserted in order to prevent any damage due to stress. Furthermore, quench heaters are included to heat the coil in case of a quench such that the quench energy spreads as fast as possible across the whole magnet.

Because of the oppositely directed currents in the coil cross section the coil is exposed to enormous LORENTZ forces pressing the coil apart. In order to prevent any conductor movement during the operation of the magnet, which could cause a quench, the coil is hold by a collar of non-magnetic material like stainless steel or aluminum. In addition, the collar is providing so-called prestress to the coil which is holding the conductors at their positions during operation.

By surrounding the coil with an iron yoke made of ferromagnetic material the field inside the aperture can be enhanced without increasing the excitation current or the number of

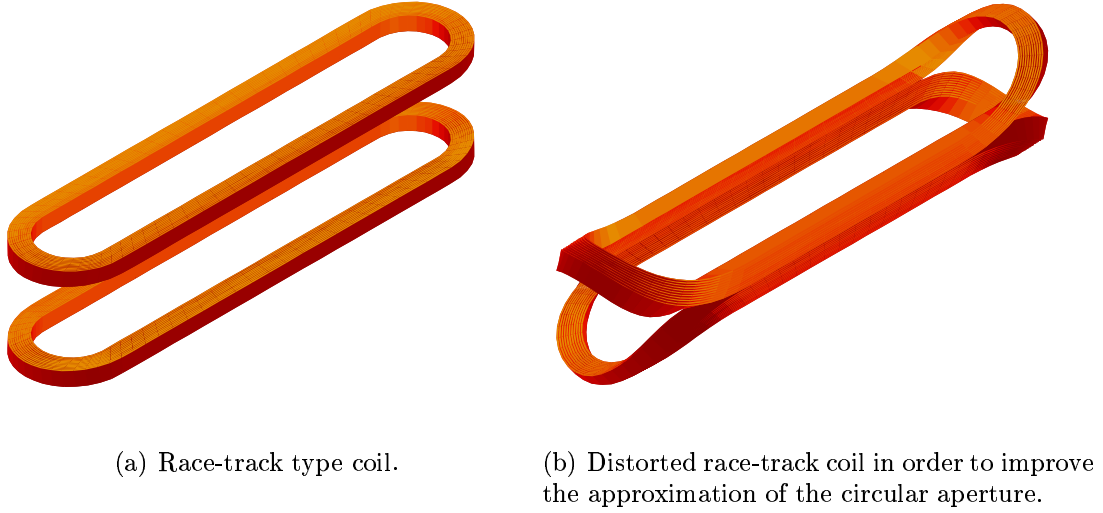


Figure 1.3: Formation of a coil for a magnet with circular bore (with the courtesy of S. Russenschuck).

superconducting cables. At the same time, the fringe field, the field outside the magnet, is reduced. The cross section of the iron yoke includes some punched holes for the heat exchanger pipe of the helium, for the bus bars which contain superconducting cable connections for other magnets and for the steering of the field quality with respect to saturation. The prestress is also applied from the shrinking cylinder outside the yoke and is, in this way, submitted by the yoke to the collar. The iron yoke can also be used as a mechanical support for the collar.

The coil, the collar and the iron yoke are incorporated into the so-called shrinking cylinder. When the magnet is cooled down to the working temperature of a few kelvin, the cylinder applies additional prestress to the iron yoke and the collar by means of thermal contraction. The cylinder also serves as container for the liquid helium which is used for the cooling of the superconducting cables. The whole structure is denoted as cold mass. The cold mass is inserted in a cryostat in order to bridge the temperature difference of around 300 K.

1.4 Coil Cross Section Optimization

As described in the previous section, a superconducting magnet consists of a large number of parts, each serving a very specific purpose and ensuring a successful operation. For an efficient design process the number of parts and different aspects needs to be reduced. Since the length of accelerator magnets is much greater than the size of the aperture, this results in the consideration of the magnet cross section only. End effects are taken into account in further optimizations.

For the application of a magnet in particle accelerators very high field strengths as well as a very high field quality are needed. The field and the field quality are mainly determined by the number and the position of the superconducting cables. Thus the first phase of the magnet design aims on the coil cross section optimization. Therefore, second order criteria like, *e.g.*, the cost of the magnet, the winding and construction process and the quench protection are only indirectly taken into account and are not subject to the first optimization process.

The optimization of the coil cross section can be subdivided into four elementary steps:

1. Determination of the required number of conductors by means of, *e.g.*, numerical calculations of a preliminary design or analytical estimations.
2. Optimization of the conductor alignment and minimization of the relative multipole errors at the operation point for a basic iron yoke.
3. Reduction of the variation of the relative multipole errors due to the iron saturation during ramp up of the field, *e.g.*, by modification of the iron yoke shape.
4. Compensation of the persistent magnetization current induced field errors by means of ferromagnetic inserts or passive superconductors.

Since step no. 3 and 4 also affect the multipole errors at high field, step no. 2 has to be repeated after every modification.

After the coil cross section optimization by means of numerical simulations has demonstrated that the requirements in field strength and quality could be met, the design process is broadened to more and more aspects like, *e.g.*, mechanical-, 3D-computations and quench protection.

1.5 Objective of this Thesis

The thesis work is carried out in collaboration with the NED activities and the practical objectives are defined by the requirements of the NED program:

1. Starting from the preliminary design [4] and relying on the specifications of the NED program the coil cross section of the $\cos \theta$ -layer configuration with 88 mm aperture is optimized. The optimization is mainly subject to the field quality at the operation point but also to design guidelines representing the experiences of the construction of previous magnets.
2. The variation of the multipole errors due to the iron saturation is compensated by means of modifications of the iron yoke shape. Therefore different approaches are studied and the coil cross section is optimized for the final yoke geometry.
3. The persistent current induced field errors are estimated for the present design and cable. Based on these results different compensation methods are investigated.

1.5. Objective of this Thesis

The numerical calculations and optimization results are supported by analytical estimations.

2 Specifications for the NED Magnet

The electromagnetic design of a magnet is subject to various restrictions like mechanical limits, material properties and field quality expectations. All these fundamental restrictions are explained in the subsequent sections. Note that, if not otherwise indicated, all numbers are given at room temperature.

2.1 Coil Cross Section

The coil cross section of the studied magnet is defined as a $\cos\theta$ layer design. It consists of two layers of superconducting cables distributed azimuthally around the aperture in order to approximate a $\cos\theta$ like current distribution. Unlike for the LHC main bending magnets, for the NED magnet the same type of cable is used for the inner and outer layer (it is not exploited that the outer layer is able to carry higher current densities due to the locally lower field).

The coil cross section is perfectly left-right anti- and up-down symmetric. For this study the asymmetries at the coil ends and at the connection of the two coil layers are neglected, thus the first quadrant of the coil cross section can be considered only.

The aperture size of the studied magnet is given to 88 mm which yields an aperture radius r_A of 44 mm, and is also defining the inner coil radius. The radial position of the outer layer r_{L2} comprises the inner layer, its insulation, an additional inter-layer insulation and eventually space for quench heaters. It is given to 73 mm [11] yielding an inter layer space of 2.6 mm. The outer coil radius is thus given to 99.4 mm.

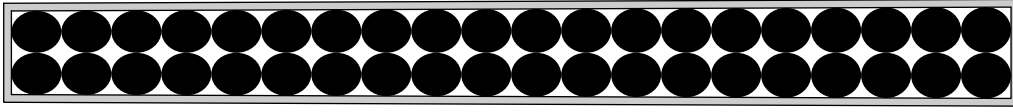
The conductors of each layer build groups of at least 1 up to 16 to 20 cables, so-called blocks. The blocks are numbered from the outer to inner layer, from the midplane to the outside. This way, block 1 is on the midplane in the outer layer and the block with the highest number is the block with the largest positioning angle in the inner layer. The space between two blocks is filled by so-called wedges made of non-magnetic and thermally well conducting copper.

The conductors and the copper wedges are insulated and glued together in a winding-curing process. For each layer they are combined to an upper and lower half pole. The four poles are again separated by insulation material and hold by the collar structure after collaring.

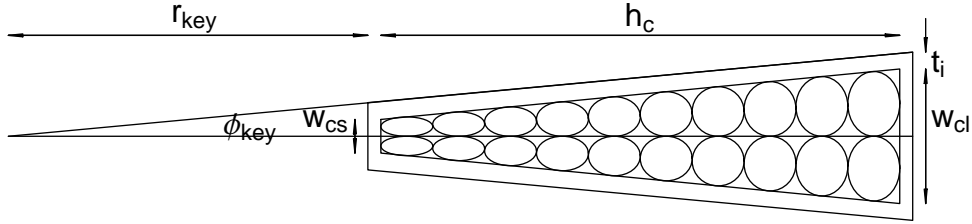
2.1.1 Cables

The used cable is of RUTHERFORD-type with a slight keystoneing. The RUTHERFORD-type cable was developed at the Rutherford Appellton Laboratory (RAL) and is made of a few tens of strands, twisted together and shaped into a two layer cable [12]¹. The cable is pressed in a slight trapezoidal shape, so-called keystoneed, in order to better approximate the round aperture like a roman arc.

Figure 2.1 a) shows a sketch of the used cable with correct aspect ratio. Figure 2.1 b) shows an exaggerated view of the keystoneing of the cable denoting all quantities. It also demonstrates the deformation of the strands which is not taken into account for this thesis.



(a) Sketch of the cable for NED with a scale of 1 : 5. All proportions are according to the specifications.



(b) Sketch of an extremely keystoneed cable showing all used quantities. The deformation of the strands is indicated.

Figure 2.1: Sketches of the keystoneed Rutherford-type cable for NED.

LEROY and VINCENT-VIRY carried out a preliminary magnetic design of the NED magnet [4] in order to derive meaningful strand and cable parameters. This resulted in the cable denoted as CK6 with the specifications given in [1] (also shown in tab. 2.1 and tab. 2.2).

The keystoneing of the cable can be further depicted by two quantities: the keystoneing angle ϕ_{key} which is given by half the angle covered by one cable and the the keystoneing radius r_{key} given by the radius of an arc made of cable elements. They are given to:

$$\phi_{\text{key}} = \arctan \frac{(w_{\text{cl}} - w_{\text{cs}})/2}{h_c} \approx 0.22^\circ, \quad (2.1)$$

$$r_{\text{key}} = \frac{w_{\text{cs}} + 2t_i}{2\phi_{\text{key}}} \approx 335 \text{ mm}. \quad (2.2)$$

The fact that the keystoneing radius r_{key} is nearly 8 times greater than the aperture radius r_A demonstrates well the necessity to insert wedges in the coil cross section in order to support a radial alignment of the conductors.

¹The RUTHERFORD-cable is similar to the also known ROEBEL-Stab [13, 14].

Table 2.1: Salient cable parameters for NED as derived in [4, CK6].

Quantity	Value	Unit
height h_c	26	mm
width (short side) w_{cs}	2.175	mm
width (long side) w_{cl}	2.375	mm
number of strands n_{st}	40	-
Degradation due to cabling	10%	-
Insulation thickness per side t_i	0.2	mm

Table 2.2: Salient parameters for the NED strands and filaments as given in [1] and [15].

Quantity	Value	Unit
Strand diameter d_{st}	1.25	mm
copper to non-copper volume ratio Cu/nonCu	1.25	-
number of filaments n_f	≈ 280	-
Non-copper critical current density J_c at 12 T and 4.2 K	3	kA/mm ²
Non-copper critical current density J_c at 15 T and 4.2 K	1.5	kA/mm ²
Outer filament diameter d_{fo}	< 50	μm
Inner filament diameter d_{fi}	≈ 31.6	μm

2.1. Coil Cross Section

For the scaling and calculation of the different commonly used current densities the cross sectional area of the strand and the cable is needed. These values are calculated by means of the basic values given in in tab. 2.1 and tab. 2.2. In addition the most commonly needed conversion factors for the current density are calculated and also shown in tab. 2.3.

Table 2.3: Various cross sectional areas of the cable and the most commonly used conversion factors.

Quantity	Formula	Value	Unit
A_{filament}	$\pi \left(\frac{d_{\text{fo}}}{2} \right)^2$	≈ 1960	μm^2
$A_{\text{filament}(\text{superconducting})}$	$\pi \left(\left(\frac{d_{\text{fo}}}{2} \right)^2 - \left(\frac{d_{\text{fi}}}{2} \right)^2 \right)$	≈ 1180	μm^2
A_{strand}	$\pi \left(\frac{D_{\text{strand}}}{2} \right)^2$	1.23	mm^2
$A_{\text{strand,non-Cu}}$	$A_{\text{strand}} \frac{1}{1+\text{Cu/nonCu}}$	0.55	mm^2
A_{strands}	$n_{\text{st}} A_{\text{strand}}$	49.09	mm^2
A_{cable}	$h_{\text{c}} \frac{w_{\text{cs}}+w_{\text{cl}}}{2}$	59.15	mm^2
$A_{\text{cable}(\text{insulated})}$	$(h_{\text{c}} + 2t_{\text{i}}) \left(\frac{w_{\text{cs}}+w_{\text{cl}}}{2} + 2t_{\text{i}} \right)$	70.65	mm^2
$F_{\text{nonCu} \rightarrow \text{superconducting}}$	$A_{\text{filament}} / A_{\text{filament}(\text{superconducting})}$	1.66	-
$F_{\text{nonCu} \rightarrow \text{strand}}$	$A_{\text{strand,non-Cu}} / A_{\text{strand}}$	0.44	-
$F_{\text{strands} \rightarrow \text{cable}}$	$A_{\text{strands}} / A_{\text{cable}}$	0.83	-
$F_{\text{cable} \rightarrow \text{cable}(\text{insulated})}$	$A_{\text{cable}} / A_{\text{cable}(\text{insulated})}$	0.84	-

For the numerical calculation by means of **ROXIE** the geometrical and electrical properties of the used cable including the insulation and the critical current density are defined in the so-called `cadata.file` (appendix D.2).

2.1.2 Wedges

For the approximation of a $\cos \theta$ -type current distribution, non current carrying areas are needed in the cross section. In addition, due to the small keystoneing of the cable, wedges are needed in order to provide a radial alignment of the conductor blocks.

The size of the wedges must not under-run a minimum thickness. Due to the enormous LORENTZ forces, the wedges are pressed against the conductors and if they are too thin, their sharp edge could cut the wedge or the conductor insulation. Therefore the minimum width of the small inner side of the wedge was set to 1.3 mm. Practically this is defined as the minimum distance of the inner insulated corners of two adjacent blocks [16].

For the compensation of persistent current induced field errors by means of ferromagnetic elements, it is possible to replace the copper wedge or part of it by a ferromagnetic material.

2.1.3 Insulations

All conductors are insulated by a wrapped up insulation tape in order to block the voltage drop between the turns in superconducting as well as in normal conducting state (quench). In addition, all surrounding parts are insulated in order to block any voltage to ground.

The electrical properties as well as the voltage drops are not considered for this study and the insulation is taken only into account by means of the required thickness.

As specified in [1] the conductors are insulated by a wrapping of 0.2 mm per side. The upper and lower half pole of the coil are insulated at the midplane also by 0.2 mm. The radial space between the coil and the collar is set to 1 mm containing the insulation to ground, the coil protection sheet and the quench heater.

The insulation of the wedges as well as the insulation in between the layers are not specified since they are represented by other specifications like the minimum radii or distances.

2.2 The Magnet Cross Section

Once the coil cross section is determined, mainly geometrical properties are important for the magnet cross section and with exception of the iron yoke no magnetic material properties are taken into account for the field calculation. Figure 2.2 shows the magnet cross section with salient radii.

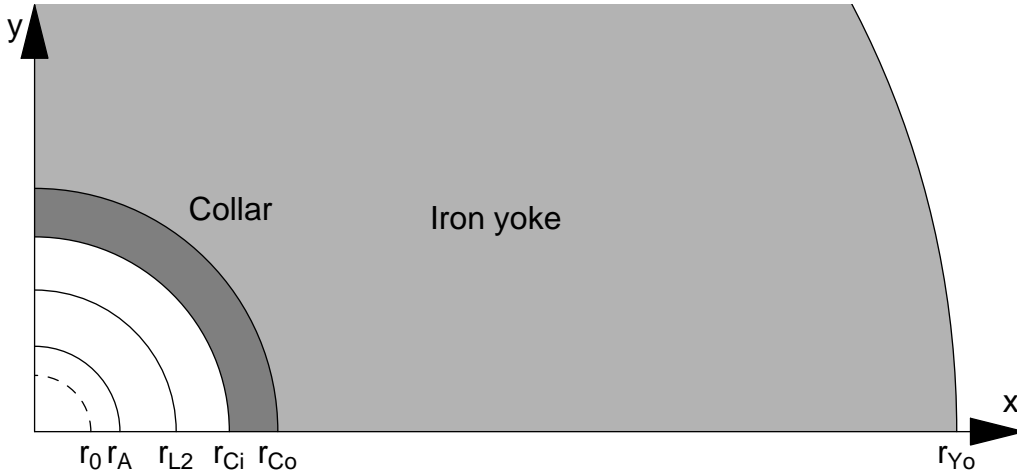


Figure 2.2: Magnet cross section with stainless steel collar and iron yoke denoting the required radii. The geometrical proportions are according to the given NED specifications.

2.2.1 Collar

From the outer coil radius of 99.4 mm the inner collar radius r_{Ci} can be determined to 100.4 mm by taking into account the 1 mm of insulation, coil and quench protection. With a minimum collar thickness of 25 mm the outer collar radius r_{Co} is given to 125.4 mm [11].

The collar is basically of circular shape and has a nose which is inserted in the coil in order to apply azimuthal prestress. For this reason, the maximum position angle of the

2.3. Material properties

coil blocks should be at around 70° to 75° and the maximum position angle of the outer layer has to be smaller than the one of the inner layer.

For the magnetic calculations the collar is only taken into account by its geometrical constraints.

2.2.2 Iron Yoke

The outer collar radius r_{Co} is also the inner yoke radius r_{Yi} and with the yoke thickness of 350 mm suggested in [4] the outer iron yoke radius r_{Yo} is given to 475.4 mm. The basic shape of the iron yoke is an ideal hollow cylinder which leaves room for the reduction of multipole variation due to iron saturation by changing the contour.

Table 2.4: Salient specified radii for the 88 mm NED magnet.

Quantity	Value	Unit
Reference radius r_0	29	mm
Aperture radius r_A	44	mm
Inner radius of outer layer r_{L2}	73	mm
Inner collar radius r_{Ci}	100.4	mm
Outer collar radius r_{Co} , inner yoke radius r_{Yi}	125.4	mm
Outer yoke radius r_{Yo}	475.4	mm

2.3 Material properties

2.3.1 Critical Current Density

For the calculation of persistent superconductor magnetization current induced field errors the so-called critical current density is needed. For the strands of the NED cable no measurement data is available at the moment and it is not expected to obtain this within the next year. For this reason the critical current density is estimated by a similar but smaller strand, stemming from an older generation [15].

Figure 2.3 shows the estimated critical current density in the non-copper part of the NED strands. For the numerical calculations the critical current density in the superconducting part of the strands is used and the shown current density is scaled by the factor $F_{\text{nonCu} \rightarrow \text{superconducting}}$. Table 2.5 shows the estimated fit parameter. The fit function and the implementation in **ROXIE** are shown in appendix C.1.

2.3.2 Thermal Contraction Factor

The used Nb_3Sn cables show superconductivity only for very low temperatures. For the operation of the magnet it needs to be cooled - for low temperature superconductors as Nb_3Sn by the cooling medium liquid helium.

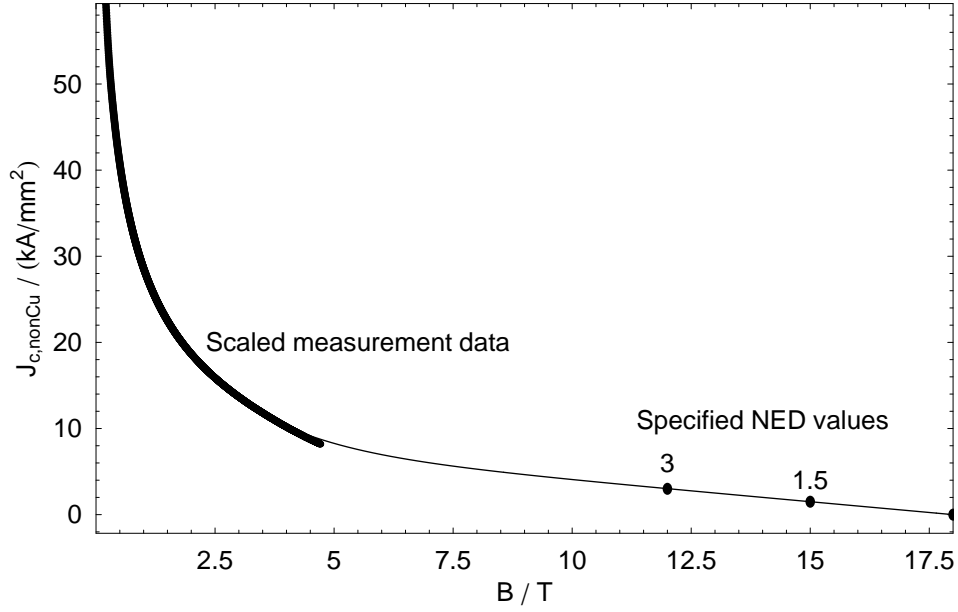


Figure 2.3: Estimated critical current density in the non-copper area of the NED strands at 4.2 K.

Table 2.5: Estimated fit parameters for the critical current density in the superconducting area $J_{c,sc}$ at 4.2 K [15] as also included in appendix D.2.

Parameter	Value	Unit
J_{c0}	15	kA/mm ²
a	0.991	-
b	3.538	T ⁻¹
c	3.810	-
d	0.527	T ⁻¹
g	1	-

Because it is more practical to thermally insulate not only the coil but the whole cold mass, all parts are subjected to thermal contractions. The different materials show different thermal contraction factors [17] (see tab. 2.6) which have to be considered especially for mechanical and stress calculations. For the magnetic design the change of the coil position and the inner yoke radius have to be taken into account. In a first approximation this is done by centric dilatation:

$$r_{\text{warm}} \rightarrow r_{\text{cold}} = r_{\text{warm}} (1 - s_{\text{thermal}}) \quad (2.3)$$

As one can see from tab. 2.6 the contraction of the coil is greater than those of the collar and the yoke and this way compressive stress is lost during cool down. This has to be compensated by additional prestress.

All geometric values given in this thesis are measured at room temperature. For the

2.3. Material properties

Table 2.6: Integrated thermal contraction factors for a temperature change from 293 K down to 4.2 K as used for NED [17].

Material	Symbol	Value
Coil	s_{coil}	$3.9 \cdot 10^{-3}$
Wedge	s_{wedge}	$3.6 \cdot 10^{-3}$
Stainless steel collar	s_{collar}	$2.9 \cdot 10^{-3}$
Iron yoke	s_{yoke}	$2.1 \cdot 10^{-3}$

numerical calculations the transformation is done by **ROXIE** independently for the coil and the iron material.

2.3.3 Permeability

The calculation of a magnet cross section compasses the calculation of the coil field and the repercussion of the magnetic materials. Therefore, only the ferromagnetic parts like the iron yoke are considered. Everything else like, *e.g.*, the conductors, the copper wedges or the collar are replaced by empty space.

The iron yoke consists of laminations of low carbon steel interlaced with insulations like the iron yoke of the LHC main bending magnets. The magnetization of the laminations shows a very narrow hysteresis which is neglected for the calculations. The stress and temperature dependency of the iron magnetization, especially the decrease of the maximum relative permeability with increasing stress [3, p. 100ff] are not taken into account.

By constructing the iron yoke of laminations, the iron yoke is anisotropic. This is numerically taken into account by means of the so-called packing factor λ which is defined by the ratio of the thickness of a slab of the yoke to the thickness l_{iron} of the slab and the empty space in between two slabs $l_{\text{non iron}}$:

$$\lambda = \frac{l_{\text{iron}}}{l_{\text{iron}} + l_{\text{non iron}}}.$$

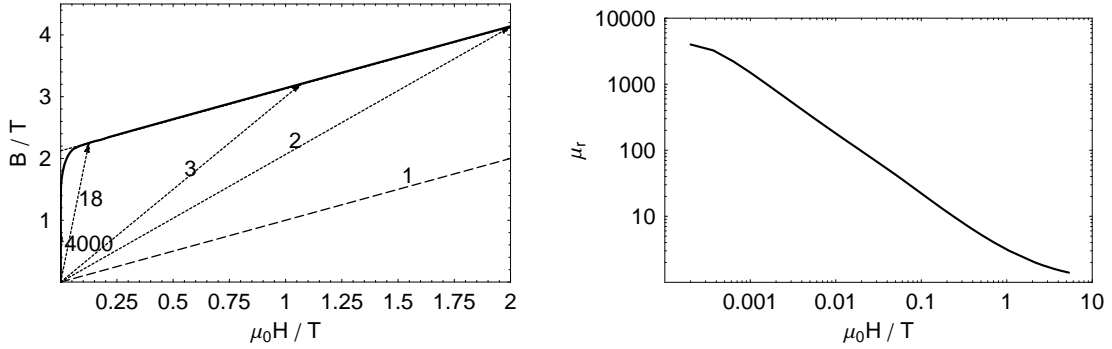
For the laminations of the LHC λ is given to 0.985 [3, p. 96]. For analytical calculations this is not taken into account.

Figure 2.4 a) shows the measured magnetic flux density versus magnetic field, the so-called BH-curve, for the iron material at a temperature of 4.2 K and zero stress. The magnetic induction increases rapidly with increasing magnetic field until the so-called saturation field B_{sat} is reached. Then the increase continues linearly with a slope of 1. For the analytical calculations the first part of the curve progression can be replaced by a linear function with a high slope of at minimum 500 which is equivalent to the relative permeability. The saturation field is given by the intersection point of the linear approximation of the high field part with the ordinate axis to $B_{\text{sat}} = 2.12 \text{ T}$.

The relative permeability μ_r is defined by the linear equation

$$\mu_r = \frac{B}{\mu_0 H}$$

what can be identified as the slope of the arrows shown in fig. 2.4 a). It can be seen that the relative permeability decreases with increasing magnetic field and tends towards 1 (indicated by the dashed line below the curve) which is also shown in fig. 2.4 b).



(a) B versus $\mu_0 H$ plot. The slope of the arrows shows the relative permeability for some arbitrary points on the graph. (b) Relative permeability μ_r , calculated from the ratio $B/(\mu_0 H)$.

Figure 2.4: Magnetic properties of the permeable material used for the iron yoke.

The shown BH-curve and the filling factor are used for all numerical calculations by means of the field computation program **ROXIE** and are denoted as BHiron2 (shown in appendix D.1). This includes the study of ferromagnetic wedges and inserts for the compensation of persistent current induced field errors.

2.4 Stress/Forces

In superconducting magnets compressive prestress is used to hold the conductors at their place during operation. In addition stress is created by the enormous LORENTZ-forces which superimpose positively in some areas of the magnet cross section like at the midplane. Furthermore the superconducting strands are sensitive to strain and the critical current density is reduced with increasing stress or a quench can be triggered. The peak stress for the NED cable is given to 150 MPa [1].

Until a detailed mechanical study of all forces and structural deformations will be done, the required prestress can be estimated only and is given to approximately 20 MPa [18]. Therefore the stress due to LORENTZ-forces shall not exceed 130 MPa.

From the magnetic induction and the excitation current the LORENTZ forces of each conductor can be calculated. By adding the azimuthal force component of all conductors of one layer and dividing by the conductor broadface given by h_c , a first approximation of

the most critical stress on the midplane can be obtained. The resulting horizontal force in the apperture is given by twice the sum of the horizontal force component of all conductors of one quadrant.

2.5 Electromagnetic Properties

For the electromagnetic optimization of the coil and magnet cross section, two main objectives are defined: A magnetic field of 15 T and a high field quality.

The high magnetic field of 15 T is specified as the peak field on any conductor for 0% margin on the load line. This working point is very critical and would not be used for regular operation, but it demonstrates well the suitability of Nb₃Sn-cable for high-field magnets. The optimizations are carried out for the operation point with a greater margin.

The field quality is expressed by means of the so-called harmonic relative multipole errors (see chapter 3). The multipole errors rely on a specified reference radius and are evaluated for a certain operation point. All multipoles are supposed to be as small as possible (of only a few units of 10^{-4} [1]) and to show a small variation during ramping up the current/field.

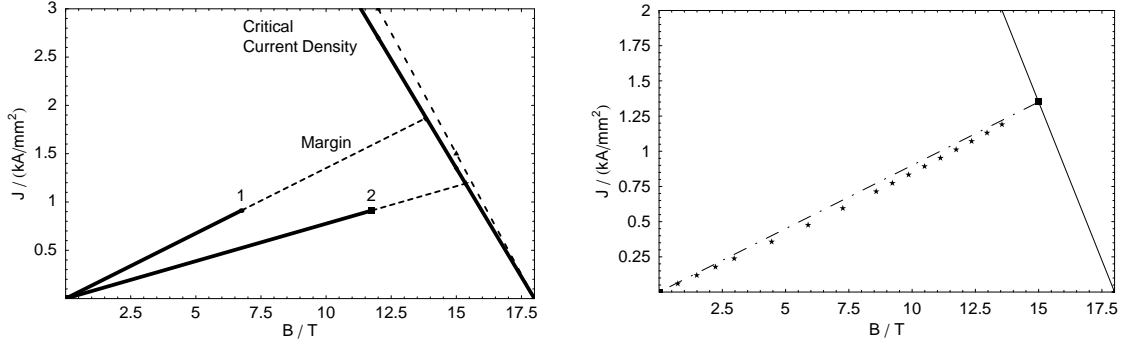
2.5.1 Operation Point

The maximum field and maximum current density in a superconductor are limited. For a given temperature this is expressed by the function of critical current density versus magnetic flux density (see section 1.2.1). For high fields and small variations the critical current density can be approximated by a straight line as shown in fig. 2.5 a). The working point of all conductors must be situated below this line and for a safe operation a certain margin should be kept.

All conductors with the same excitation current density are located on the same horizontal line in this diagram. The conductor which is exposed to the highest field is closest to the line of critical current density and shows the smallest margin. For a configuration with only one type of conductor, *e.g.*, no current grading between the layers and a single excitation current, the minimum margin is determined by a single conductor (in the figure indicated by 2).

With increasing excitation current the peak field on the conductor increases simultaneously and the working point moves towards the curve of critical current density. For linear materials the trajectory of the working point is a straight line and therefore denoted as load line. If saturation effects have to be considered the trajectory of the working point is non-linear as shown in fig. 2.5 b). Consequently this results in a change of the load line for every excitation step.

The so-called margin on the load line is the distance of the working point to its centric projection on the curve of critical current density (as shown in fig. 2.5 a)). Note that a variation of the critical current density, *e.g.* due to current degradation, changes the calculation of the margin on the load line. This is demonstrated by the dashed line in fig. 2.5 a) representing a 10% greater current density.



(a) Working point, load line and margin on the load line.

(b) Non linear trajectory of the working point due to iron saturation.

Figure 2.5: Example and definition of the margin on the load line.

For the NED magnet the temperature is set to 4.2 K and all optimizations are carried out for a margin of around 10% on the load line. The maximum available current is set to 30 kA in the conductors².

2.5.2 Reference Radius

The evaluation of the multipole errors is not done at the standard two-third of the aperture radius (as stated in [1]), but at integers in close vicinity. For the different aperture diameter used within the NED activity, these radii are given in tab. 2.7 [19].

Table 2.7: Reference radii for the multipole expansion.

Aperture diameter	Radius of reference	Unit
88	29	mm
130	43	mm
160	53	mm

²An independent powering of the inner and outer layer of the coil in order to encompass the flaw of the relatively low current density in the outer layer is not considered at the moment due to the additional problems for the winding of the coil and the connections.

3 Multipole Errors

In order to quantify the field quality of a magnet the so-called harmonic multipole errors are used. Therefore the radial¹ component of the magnetic field in the aperture is analyzed and expressed by means of a FOURIER expansion.

For the studies of certain magnet designs and for the optimization of the overall field quality of a magnet the field error induced by one single line current shall be derived. With the expression obtained in this way it is possible to show the effect of a symmetric coil layout on the multipoles and to calculate the sensitivity of the multipole errors on the conductor position.

Furthermore the expected field errors for simple geometries build of line currents can be calculated.

3.1 Multipole Expansion

For an arbitrary field of magnetic induction in a current free region the radial component is obtained from the normal field at a reference radius r_0 . Since the dependency of the normal field then yields to be 2π -periodic it can be expressed by a FOURIER expansion [20].

$$B_r(r_0, \phi) = \sum_{n=1}^{\infty} [A_n(r_0) \cos(n\phi) + B_n(r_0) \sin(n\phi)] \quad (3.1)$$

The coefficients A_n and B_n represent the contribution of the two n^{th} orthogonal ideal multipole magnets to the analyzed field and are a function of the reference radius. The B_n represent the contribution of ideal $\cos(n\theta)$ magnets² (see section 4.2.1) to the field and are denoted as "normal" components. The A_n are denoted as "skew" components

¹The choice for the radial component only does not yield any limitations: The field in the aperture can be expressed by means of the magnetic vector potential. This is given for a current free, infinite long and z -directed geometry by the scalar solution of the LAPLACE equation which azimuthally consists of a FOURIER series. The solution of this equation is either determined by the potential or by the tangential derivative on the boundary (the latter case is a bit special because an unknown superimposed constant remains and the boundary condition has to give a divergence-free field). It follows that all constants of the FOURIER expression and the general solution of the LAPLACE equation respectively can be determined in both ways.

Remark: Considering both, the radial and azimuthal field components would yield twice as many equations as necessary.

²In literature as [21] the concept of a magnet build by a $\cos(n\theta)$ depending cylindric current sheet is denoted as ideal $\cos(n\theta)$ configuration. For the motivation of the multipole errors the arbitrary angle θ is replaced by the cylindrical coordinate ϕ .

3.2. Multipole Error of a Single Line Current

and represent the contribution of ideal $\sin(n\theta)$ magnets or, more precise, $\cos(n\theta)$ magnets turned by a quarter period³.

$$A_n(r_0) = \frac{1}{\pi} \int_0^{2\pi} B_r(r_0, \phi) \cos(n\phi) d\phi, \quad (3.2)$$

$$B_n(r_0) = \frac{1}{\pi} \int_0^{2\pi} B_r(r_0, \phi) \sin(n\phi) d\phi. \quad (3.3)$$

Usually these FOURIER coefficients are normalized to the main field of the analyzed structure and then given as relative values a_n for the skew and b_n for the normal components. For a dipole with a vertical field the main component B_N is given by B_1 . The a_n and b_n are called relative harmonic multipole errors and usually expressed in units of 10^{-4} :

$$a_n = \frac{A_n(r_0)}{B_N} 10^4, \quad (3.4)$$

$$b_n = \frac{B_n(r_0)}{B_N} 10^4. \quad (3.5)$$

In this way the field in the aperture of a magnet can be split into the contribution of ideal multipole components. The field and current distribution for the first six lower order normal multipoles are shown in fig. 3.1. For the application in particle accelerators, these have to be corrected by additional corrector magnets and therefore taken into account for the design of the machine and the construction of the magnets. For each multipole certain limits are defined which must not be exceeded.

3.2 Multipole Error of a Single Line Current

The multipole errors of any geometry can be calculated in general by evaluating Eqs. (3.2) and (3.3), but for a single line current this results in rather complicated integrals. By using the FOURIER expansion of the field of a single line current derived in section 4.1.1 and comparing the coefficients the same result can be obtained much easier.

Considering a z -directed line current at a position (ρ_0, ϕ_0) , the radial magnetic induction $B_{|,r}$ at a position with a radius ρ smaller than the positioning radius ρ_0 is given by Eq. (4.4) which can be expressed as

$$B_{|,r}(\rho, \phi) = -\frac{\mu_0 I}{2\pi} \sum_{n=1}^{\infty} \frac{\rho^{n-1}}{\rho_0^n} (\sin(n\phi) \cos(n\phi_0) - \cos(n\phi) \sin(n\phi_0)) \quad (3.6)$$

by using the addition theorem of the sine-function.

³The denotation of the normal and skew multipole errors is not unique. *E.g.* in the USA the A_n denote the normal and the B_n denote the skew multipole errors.

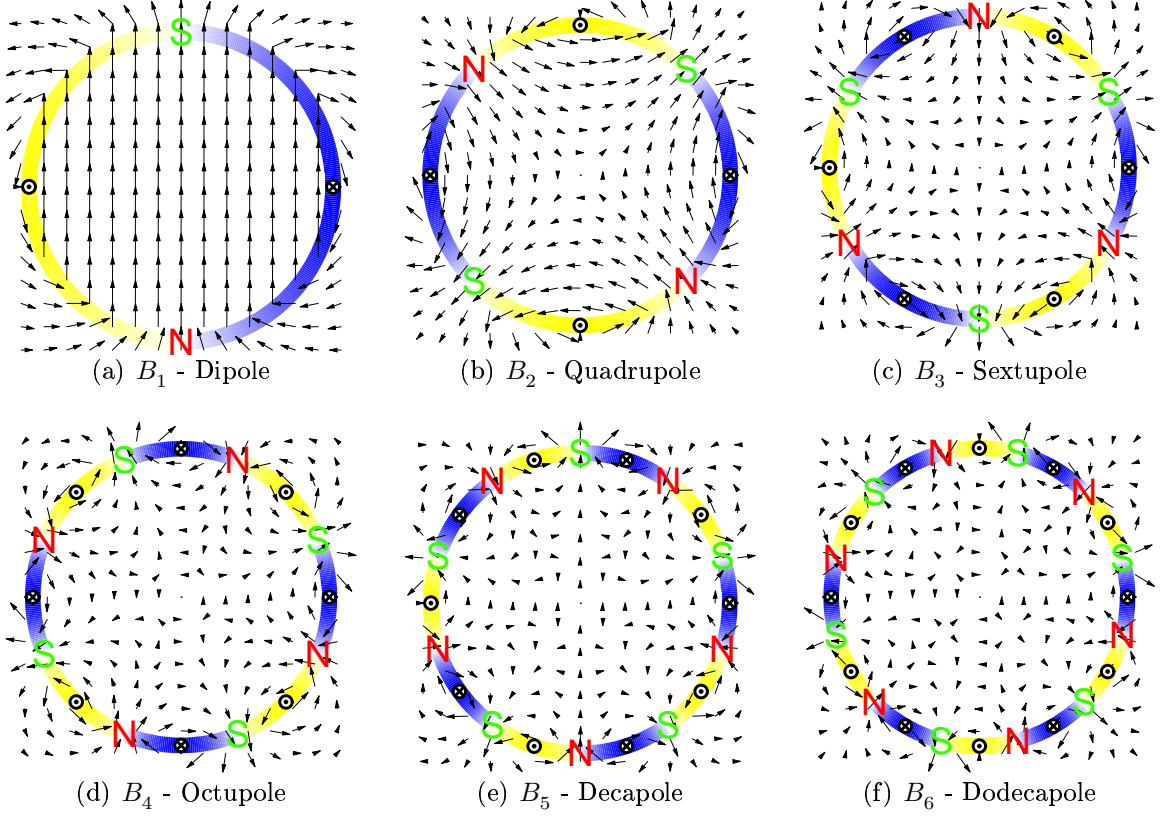


Figure 3.1: Multipoles and corresponding current distribution of the B_i ($i = 1, 2, \dots, 6$) (All B_n are positive). The skew multipoles show the same pattern but are rotated by one quarter of a period.

For a given reference radius $\rho = r_0$ the multipole coefficients A_n and B_n can be obtained by comparison of the equations (3.1) and (3.6) to:

$$A_n(r_0) = \frac{\mu_0 I r_0^{n-1}}{2\pi \rho_0^n} \sin(n\phi_0), \quad (3.7)$$

$$B_n(r_0) = -\frac{\mu_0 I r_0^{n-1}}{2\pi \rho_0^n} \cos(n\phi_0). \quad (3.8)$$

Both, normal and skew multipoles decrease in the same way with the order n due to the fact that the field inside a magnet's aperture is described and thus the ratio of the reference radius r_0 and the positioning radius ρ_0 is smaller than one. In fig. 3.2 this is shown assuming a reference radius of $2/3$ of the positioning radius which would usually only apply to the most inner strands of a magnet. For the largest part of the coil cross section the ratio of reference radius and positioning radius would be smaller than $2/3$ and therefore the decay is stronger.

With this result, the multipole errors and the main field of any structure build of parallel, indefinitely long line currents can be calculated by adding up their field errors.

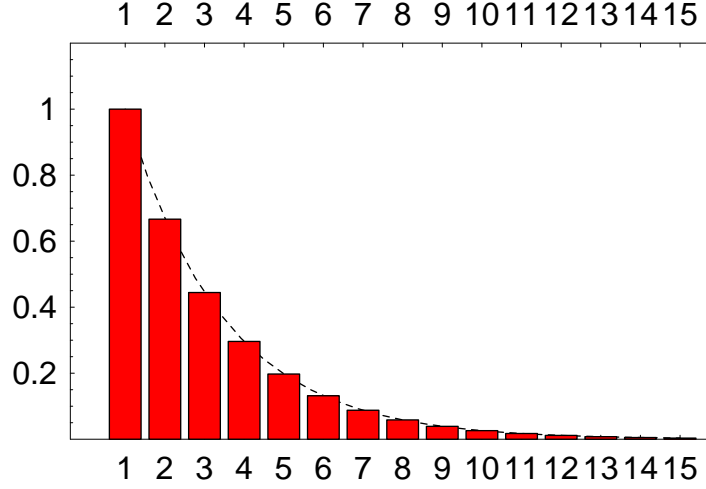


Figure 3.2: Decrease of the multipoles with increasing order. The shown example assumes a ratio of reference radius and positioning radius of 2/3.

3.3 Effect of Symmetries

The multipole errors induced by a coil cross section without iron yoke are determined by the positions of the line currents only. Deriving the Eqs. (3.7) and (3.8) for a single line current gives a sinusoidal dependence on the positioning angle which implies a certain symmetry dependency.

For the investigation of the influence of the symmetry of the current position two simple geometries consisting of only two line currents are considered and shown in fig. 3.3 a) and b): Two line currents of opposite direction and equal value positioned symmetrically to a specified plane which are denoted as anti-symmetric setup and two line currents of same direction and equal value symmetrically positioned to a specified plane which are denoted as symmetric setup⁴.

A setup of two line currents anti-symmetric to the yz -plane (fig. 3.3 a)) can be described by the two positioning angles ϕ_0 and $\pi - \phi_0$ and yields neither even normal nor odd skew multipoles.

$$A_n(r_0) = \frac{\mu_0 I r_0^{n-1}}{2\pi \rho_0^n} \sin(n\phi_0) [1 + \cos(n\pi)],$$

$$B_n(r_0) = -\frac{\mu_0 I r_0^{n-1}}{2\pi \rho_0^n} \cos(n\phi_0) [1 - \cos(n\pi)].$$

A setup of two line currents symmetric to the yz -plane can be described by the two posi-

⁴For a setup where the current sum is different from zero, the returns can be assumed symmetrically in great distance, then, due to the radial dependency of Eqs. (3.7) and (3.8) they can be neglected for the magnetic calculation

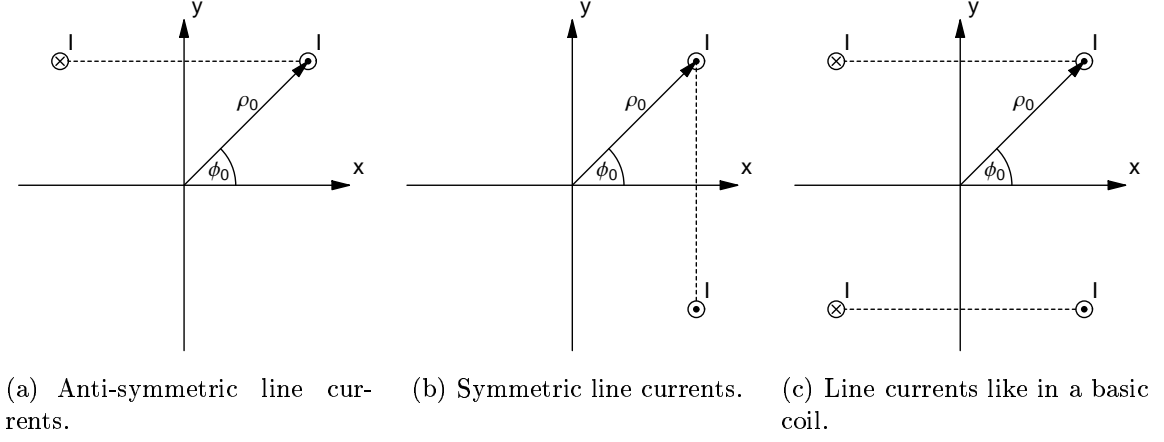


Figure 3.3: Positions and symmetries of line currents.

tioning angles ϕ_0 and $\pi - \phi_0$ and yields neither odd normal nor even skew multipoles.

$$A_n(r_0) = \frac{\mu_0 I r_0^{n-1}}{2\pi \rho_0^n} \sin(n\phi_0) [1 - \cos(n\pi)],$$

$$B_n(r_0) = -\frac{\mu_0 I r_0^{n-1}}{2\pi \rho_0^n} \cos(n\phi_0) [1 + \cos(n\pi)].$$

A setup of two line currents anti-symmetric to the xz -plane can be described by the two positioning angles ϕ_0 and $-\phi_0$ and yields no normal multipoles.

$$A_n(r_0) = 2 \frac{\mu_0 I r_0^{n-1}}{2\pi \rho_0^n} \sin(n\phi_0),$$

$$B_n(r_0) = 0.$$

A setup of two line currents symmetric to the xz -plane (fig. 3.3 b)) can be described by the two positioning angles ϕ_0 and $-\phi_0$ and yields no skew multipoles.

$$A_n(r_0) = 0,$$

$$B_n(r_0) = -2 \frac{\mu_0 I r_0^{n-1}}{2\pi \rho_0^n} \cos(n\phi_0).$$

These results are summarized in tab. 3.1. Each symmetry reduces the number of possible multipole errors by half. The characteristic of the influence is grouped by the position of the geometry to the reference system and not by the kind of symmetry.

Figure 3.3 c) shows a coil made of 4 leads symmetric to the xz -plane and anti-symmetric to the yz -plane. By combining the results above the expected multipoles can be easily obtained.

$$A_n = 0, \tag{3.9}$$

$$B_n = -2 \frac{\mu_0 I r_0^{n-1}}{2\pi \rho_0^n} \cos(n\phi_0) [1 - \cos(n\pi)]. \tag{3.10}$$

3.4. Sensitivity of the Multipole Errors

Table 3.1: Effects of symmetries/asymmetries on certain multipole errors.

	symmetric	anti-symmetric
xz -plane	$A_n = 0$	$B_n = 0$
yz -plane	$A_{n=1,3,5,..} = 0$ $B_{n=2,4,6,..} = 0$	$A_{n=2,4,6,..} = 0$ $B_{n=1,3,5,..} = 0$

These multipoles are called the "allowed" multipoles for a single aperture dipole and are in general inevitable. It is only possible to reduce them by canceling out effects.

Any multipole errors different from the allowed multipole errors are caused by asymmetries in the magnet design or resulting from production faults.

In addition to the multipole errors of the coil geometry itself, there are multipole errors caused by the iron yoke. For small fields the contribution of the iron yoke can be expressed by means of the contribution of virtual image currents. The methods derived above are still valid and all symmetries are preserved. The change of the multipole errors with excitation current and main field is linear and therefore the *relative* harmonic multipole errors are constant.

For higher magnetic fields the material of the iron yoke becomes highly non-linear and saturates. Then computations of the repercussion are carried out by means of numerical field computation methods as the Finite Element Method. Still all symmetries are preserved, but the change of the multipole errors is no longer linear and shows a certain curvature and amplitude.

3.4 Sensitivity of the Multipole Errors

For the design of a magnet the multipole errors play an important role and so it is important to know how the influence of a line current on the multipole errors depends on its position. Since magnets are build of a huge number of strands the total multipole error represents the sum of the errors of the single line currents and therefore it can be influenced by canceling out effects.

For a dipole with an up-down symmetry and a left-right anti-symmetry only odd normal multipoles exist. With Eq. (3.8) and the above shown symmetry relations the multipole errors are given by

$$B_n = -4 \frac{\mu_0 I}{2\pi} \frac{r_0^{n-1}}{\rho_0^n} \cos(n\phi_0), \quad n = 1, 3, 5, \dots \quad (3.11)$$

In figs. 3.4 a) and b) the values of the induced multipole error for each position of the xy -plane are shown in a 3D-view assuming a ratio of reference radius to aperture radius of $2/3$.

For a more detailed view fig. 3.5 shows the decrease of the multipole errors with increasing radius and the azimuthal dependency.

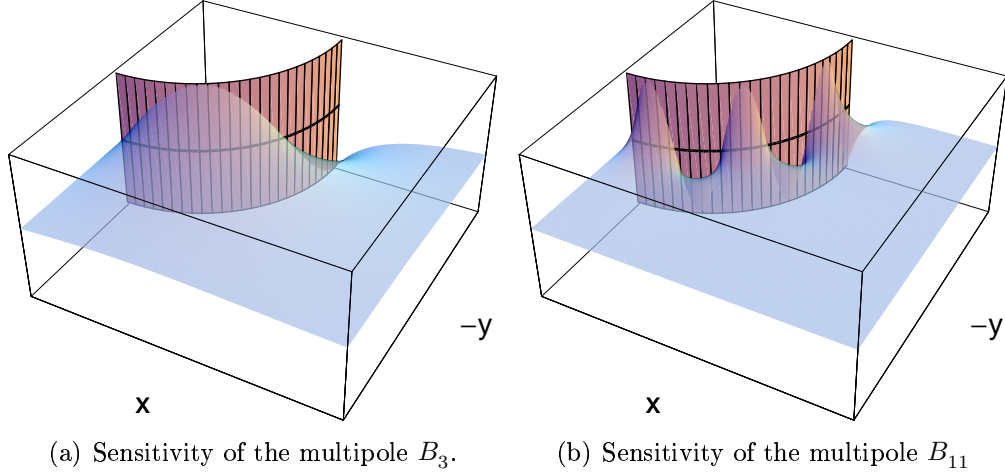


Figure 3.4: Sensitivity of the multipole error to the position of the source. The surface represents the multipole error induced by a current of strength I at this position normalized to the maximum error at $(r_A, \phi_0 = 0)$. The cylinder represents the aperture.

3.5 Scaling of Multipole Errors to Different Reference Radii

For the design of a magnet the requirements for the field quality are defined by the needs of the application and in this way the reference radius r_0 is given, too. Apart from that it might be useful to scale the multipole errors of a certain design to a different reference radius $r_{0,\text{new}}$ in order to compare two designs. Since the optimization for both designs was done for their specific reference radii, this could give only a rough estimation.

The equations for the multipole errors of a single line current (3.7) and (3.8) can be transformed to a different reference radius by extending with the fraction $(r_{0,\text{new}}/r_0)^{n-1}$. The multipole errors can be scaled to any radius by

$$A_n(r_{0,\text{new}}) = \left(\frac{r_{0,\text{new}}}{r_0} \right)^{n-1} A_n(r_0) \quad (3.12)$$

$$B_n(r_{0,\text{new}}) = \left(\frac{r_{0,\text{new}}}{r_0} \right)^{n-1} B_n(r_0) \quad (3.13)$$

In the same way it is possible to rescale the relative multipole errors.

In order to compare the NED dipole with the existing LHC main bending magnets, the target values for the LHC multipole errors are converted by means of Eq. (3.13) and shown in tab. B.2 in the appendix.

3.5. Scaling of Multipole Errors to Different Reference Radii

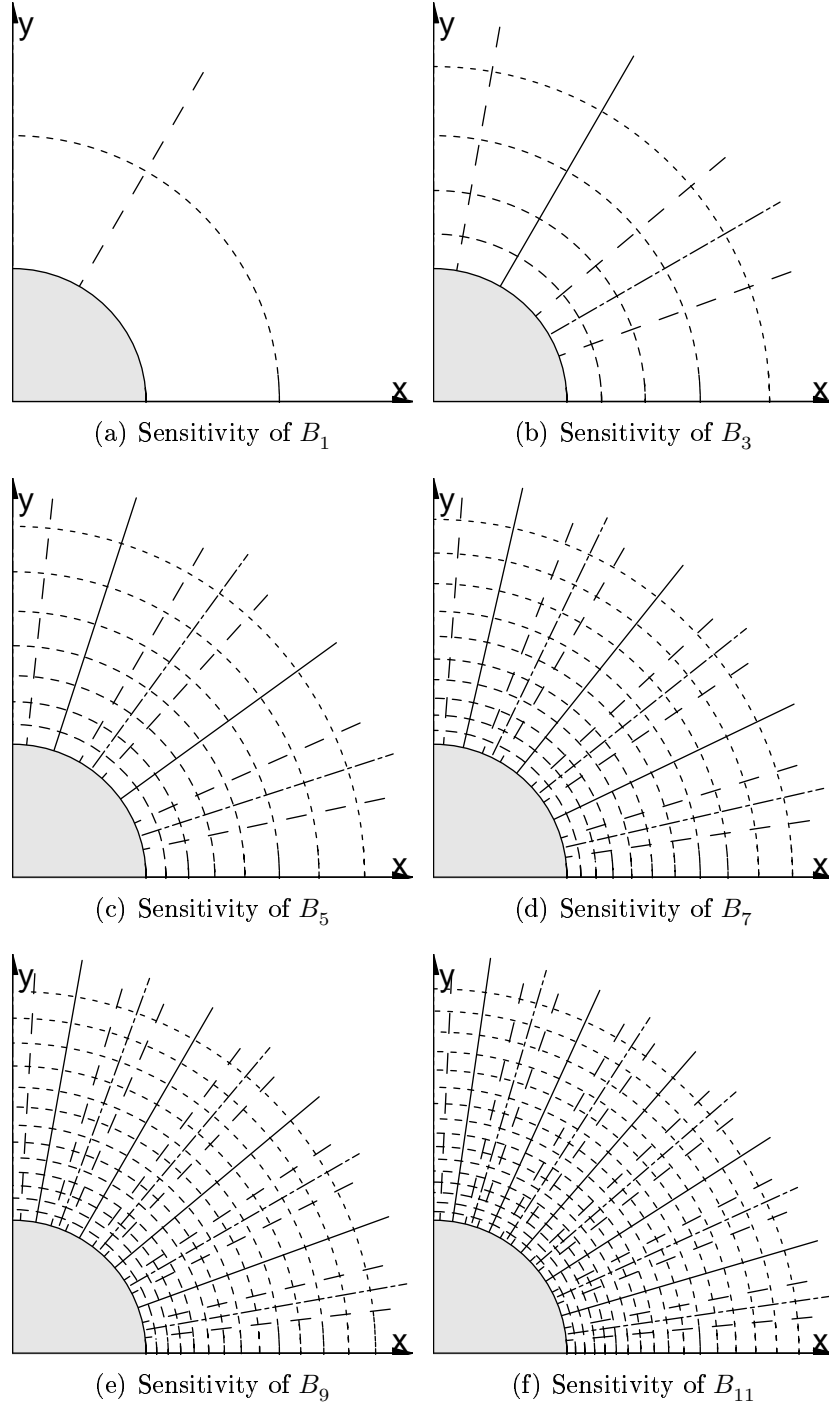


Figure 3.5: Sensitivity of the multipole error to the position of the source assuming a ratio of reference radius to aperture radius of $2/3$. The azimuthal dashed lines represent the radii where the induced multipole error decreased to the half of the value of the adjacent line. The dashed-dotted radial lines represent lines of zero multipole errors, the straight radial lines represent lines of angular extreme multipole errors and the radial dashed lines represent lines where the multipole error reduced to the half of the neighboring extreme.

3.6 Good-Field-Radius

Different magnet designs are usually qualified by their relative harmonic multipole errors. In this way, up to 10 or 20 numbers have to be taken into account and the observed differences for each multipole error have to be weighted and considered with respect to the others.

As a first and rough estimation of the field quality a so-called good-field-radius r_{gfr} shall be introduced and used within this thesis which represents the maximum radius within the aperture where the total field distortion is below a certain value.

For the introduction of the good-field-radius it shall be assumed that the magnet is *a priori* of up-down symmetry and left-right anti-symmetry. This way, the magnetic induction is given by the odd normal multipoles only. The radial component of the magnetic induction of all of these multipole configurations shows an extremum for $\phi = \pi/2$. The maximum possible distortion can be obtained by summing up the modulus of the field and thus by summing up the modulus of the normal multipoles.

By using the scaling law derived in section 3.5, the value of the sum can be changed by shifting the reference radius to different values. Defining a maximum relative field distortion of 1 unit with respect to the main field the good field radius is given by the following equation:

$$1 = \sum_{n=3,5,\dots}^N \left(\frac{r_{\text{gfr}}}{r_0} \right)^{n-1} |b_n(r_0)|. \quad (3.14)$$

Here N denotes the index of the highest order multipole error taken into account. Since all coefficients of this polynomial are by definition positive, Eq. (3.14) represents a strongly monotone function of r_{gfr} and thus the good-field-radius can be calculated easily by NEWTON's method.

Figure 3.6 shows the modulus of the field distortion for different field errors. For each of the lines a field error is assumed so that the good-field-radius is equal to half of the aperture radius r_A .

The good-field-radius calculated in this way represents the limit for the maximum distortion of the magnetic field with respect to the wanted main field. For beam dynamic needs this number carries no meaning [22].

The implementation in the field computation program **ROXIE** is documented in appendix C.3.

3.7 Field Error of a Magnetic Line Dipole

The magnetization of superconducting strands as well as of thin iron cylinders can be expressed in an approximation by the field of a magnetic dipole. This is, *e.g.*, used for the prediction of the persistent current induced field errors.

An arbitrary magnetic line dipole consists of two parallel oppositely z -directed line currents. Such a geometry can be described and calculated in the way derived above. For

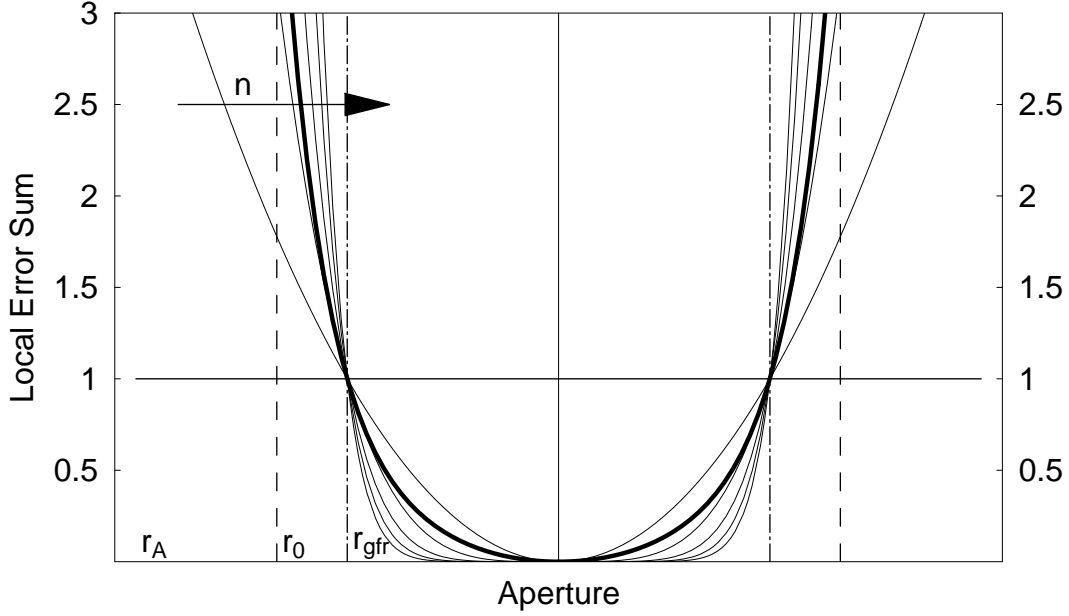


Figure 3.6: Demonstration of the good-field-radius: Modulus of the total field distortion for different types of field errors. For the thin continuous lines only one multipole error is different from zero. The value of the multipole error was chosen so that the corresponding good field radius yields half of the aperture radius r_A . In the same way but with all multipole errors with identical values the thick line is obtained. The dashed-dotted line represents the good-field-radius r_{gfr} and the dashed line represents the reference radius r_0 for the multipole computation of $2/3$ of the aperture radius.

an ideal line dipole of infinite small distance a more practical expression of the multipole errors is given in [20] and shown in this section.

An ideal magnetic dipole at (ρ_0, ϕ_0) of current I and distance d is considered (fig. 3.7). The modulus of the magnetic moment per unit length \mathbf{m}' is given by

$$|\mathbf{m}'|_{I \rightarrow \infty, d \rightarrow 0} = dI. \quad (3.15)$$

The orientation is perpendicular to the plane built by the two line currents and pointing in the direction of its magnetic induction.

Then the multipole errors created by such an ideal magnetic dipole can be expressed by

$$A_n = \frac{\mu_0 r_0^{n-1}}{2\pi \rho_0^{n+1}} n (m_{\rho_0} \cos(n\phi_0) + m_{\phi_0} \sin(n\phi_0)) \quad (3.16)$$

$$B_n = \frac{\mu_0 r_0^{n-1}}{2\pi \rho_0^{n+1}} n (m_{\rho_0} \sin(n\phi_0) - m_{\phi_0} \cos(n\phi_0)) \quad (3.17)$$

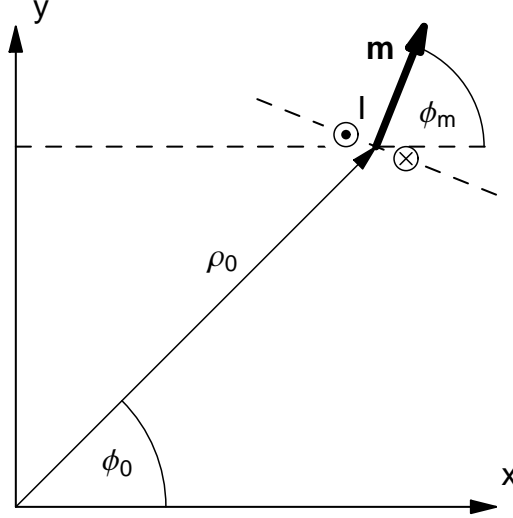


Figure 3.7: Geometry of a magnetic line dipole at the position (r_0, ϕ_0) with magnetic moment \mathbf{m}' per unit length.

where r_0 is the reference radius. The quantities m_{ρ_0} and m_{ϕ_0} denote the components of the vector of the magnetic moment \mathbf{m}' in the local orthonormal coordinate system with basis $\{\mathbf{e}_{\rho_0}, \mathbf{e}_{\phi_0}, \mathbf{e}_z\}$. For a magnetic moment given in cartesian coordinates the basis transformation reads:

$$m_{\rho_0} = |\mathbf{m}'| \cos(\phi_m - \phi_0) \quad (3.18)$$

$$m_{\phi_0} = |\mathbf{m}'| \sin(\phi_m - \phi_0) \quad (3.19)$$

where ϕ_m denotes the angle between the magnetic moment and the positive x -axis.

Comparing the multipole errors for a magnetic dipole Eqs. (3.16) and (3.17) with the multipole errors of a single line current Eqs. (3.7) and (3.8) shows that the influence of the dipole decreases one order faster with the radial distance to the center of the reference circle.

The field errors created by a setup of magnetic dipoles are also affected by symmetries. This can be shown mathematically by means of the expressions above or by using the results of the single line currents. A setup of two dipoles which magnetic momenta are directed like reversed images, can be replaced by an anti-symmetric setup of line currents and the corresponding rules apply. Considering two line dipoles with reversed image momenta and changing the orientation of one moment, yields a setup denoted as anti reversed image symmetric. This can be replaced by a symmetric geometry of line currents and the corresponding rules can be applied.

For the calculation of magnetization effects, either of superconducting strands or iron materials, the magnetic momenta are directed anti-parallel or parallel to the magnetic field. For an up-down symmetric and left-right anti symmetric dipole the magnetic field is left-right reversed image symmetric and up-down anti reversed image symmetric. For this

reason the same canceling out effects apply for the superconductor magnetization as for the position of the line currents and only the so-called allowed multipoles can be created.

3.8 Summary

The so-called *harmonic multipole errors* as they are used in this thesis are defined by the coefficients of the FOURIER expansion of the magnetic induction radial to a specified reference circle. The multipole errors normalized by the main field are denoted as *relative multipole errors* and expressed in units of 10^{-4} .

By means of the field of a single line current the sensitivity of the induced multipole errors on the conductor position with respect to the reference circle was studied. Furthermore it is shown how symmetries reduce the number of so-called *allowed multipoles* yielding only even normal multipole errors for a common single aperture dipole coil.

The dependence of the multipole errors on the reference radius was used to motivate the so-called *good-field-radius* giving one weighted measure summerizing all considered multipole errors.

The multipole errors induced by magnetic line dipoles are given. It is shown that for symmetrically positioned magnetic momenta which are directed like the field lines in a common single aperture magnet only *allowed multipoles* are created.

4 Analytic Descriptions of the Current Distribution

4.1 Line Current

The first geometry to be studied is a single line current of zero thickness and infinite length. The magnetic field is determined by the symmetry of the geometry and by means of AMPERE's law. From the ϕ -directed and $1/\rho$ radially depending magnetic field, the vector potential can be obtained by integration.

Figure 4.1 shows a line current at an arbitrary position (ρ_0, ϕ_0) , describing all geometric relations and the resulting field lines.

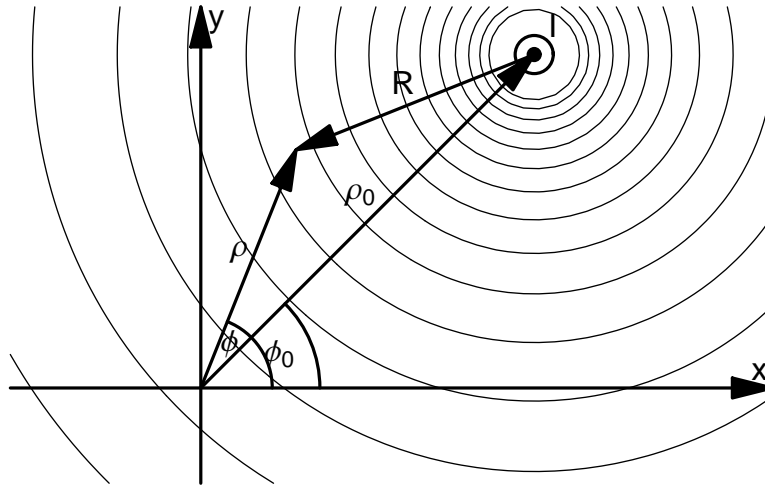


Figure 4.1: Geometry and field distribution of one arbitrary line current.

The vector potential \mathbf{A}_I of such a z -directed line current of strength I has only a z -component and is given by

$$\mathbf{A}_I(\rho) = -\frac{\mu_0 I}{2\pi} \ln \left(\frac{R}{R_0} \right) \mathbf{e}_z \quad (4.1)$$

where R denotes the distance between the position of the line current and the point where the vector potential is evaluated. The denominator R_0 denotes an arbitrary reference radius resulting from the fact that the potential was derived by integrating the magnetic field without limits. The physical meaning is discussed in appendix A.2.2.

For the following chapters the FOURIER expansion of the vector potential for one arbitrarily positioned line current is needed and shall be derived following [23].

4.1.1 Fourier Expansion of the Vector Potential $A_{|}$

In order to express the vector potential by means of the FOURIER expansion the TAYLOR series expansion of $\ln(1 - x)$ for $|x| < 1$ is used [24].

$$\ln(1 - x) = - \sum_{n=1}^{\infty} \frac{1}{n} x^n. \quad (4.2)$$

Therefore the distance R will be expressed by means of the law of cosine

$$R^2 = \rho_0^2 + \rho^2 - 2\rho_0\rho \cos(\phi - \phi_0)$$

which can be written in complex notation as

$$R^2 = \rho_0^2 + \rho^2 - \rho_0\rho e^{i(\phi-\phi_0)} - \rho_0\rho e^{-i(\phi-\phi_0)}.$$

In order to apply Eq. (4.2) the expression is split up differently for $\rho < \rho_0$ and $\rho > \rho_0$.

Fourier Expansion for $\rho < \rho_0$

Factoring out ρ_0 gives

$$R^2 = \rho_0^2 \left(1 - \frac{\rho}{\rho_0} e^{i(\phi-\phi_0)} \right) \left(1 - \frac{\rho}{\rho_0} e^{-i(\phi-\phi_0)} \right)$$

and then the logarithm term reads

$$\ln\left(\frac{R}{R_0}\right) = \ln\left(\frac{\rho_0}{R_0}\right) + \frac{1}{2} \ln\left(1 - \frac{\rho}{\rho_0} e^{i(\phi-\phi_0)}\right) + \frac{1}{2} \ln\left(1 - \frac{\rho}{\rho_0} e^{-i(\phi-\phi_0)}\right).$$

Then Eq. (4.1) can be written as

$$A_{|,z} = -\frac{\mu_0 I}{2\pi} \ln\left(\frac{\rho_0}{R_0}\right) + \frac{\mu_0 I}{2\pi} \sum_{n=1}^{\infty} \frac{1}{n} \left(\frac{\rho}{\rho_0}\right)^n \cos(n(\phi - \phi_0)), \quad \rho < \rho_0 \quad (4.3)$$

The magnetic field can be obtained by evaluating the curl of the vector potential and gives:

$$B_{|,\rho} = -\frac{\mu_0 I}{2\pi} \sum_{n=1}^{\infty} \frac{\rho^{n-1}}{\rho_0^n} \sin(n(\phi - \phi_0)), \quad (4.4)$$

$$B_{|,\phi} = -\frac{\mu_0 I}{2\pi} \sum_{n=1}^{\infty} \frac{\rho^{n-1}}{\rho_0^n} \cos(n(\phi - \phi_0)). \quad (4.5)$$

Fourier Expansion for $\rho > \rho_0$

Factoring out ρ gives

$$R^2 = \rho^2 \left(1 - \frac{\rho_0}{\rho} e^{i(\phi - \phi_0)} \right) \left(1 - \frac{\rho_0}{\rho} e^{-i(\phi - \phi_0)} \right)$$

and then the logarithm term reads

$$\ln \left(\frac{R}{R_0} \right) = \ln \left(\frac{\rho}{R_0} \right) + \frac{1}{2} \ln \left(1 - \frac{\rho_0}{\rho} e^{i(\phi - \phi_0)} \right) + \frac{1}{2} \ln \left(1 - \frac{\rho_0}{\rho} e^{-i(\phi - \phi_0)} \right).$$

From this Eq. (4.1) can be written as

$$A_{|,z} = -\frac{\mu_0 I}{2\pi} \ln \left(\frac{\rho}{R_0} \right) + \frac{\mu_0 I}{2\pi} \sum_{n=1}^{\infty} \frac{1}{n} \left(\frac{\rho_0}{\rho} \right)^n \cos(n(\phi - \phi_0)), \quad \rho > \rho_0. \quad (4.6)$$

The magnetic field can be obtained by evaluating the curl of the vector potential and gives:

$$B_{|,\rho} = -\frac{\mu_0 I}{2\pi} \sum_{n=1}^{\infty} \frac{\rho_0^n}{\rho^{n+1}} \sin(n(\phi - \phi_0)), \quad (4.7)$$

$$B_{|,\phi} = \frac{\mu_0 I}{2\pi} \frac{1}{\rho} + \frac{\mu_0 I}{2\pi} \sum_{n=1}^{\infty} \frac{\rho_0^n}{\rho^{n+1}} \cos(n(\phi - \phi_0)). \quad (4.8)$$

4.1.2 Continuity of Both Approaches at the Boundary

For the calculation of the FOURIER expansion of the vector potential of an excentric line current the space of homogeneous material was split up into two parts. The resulting fields in both subspaces need to be continuous everywhere on the boundary ($\rho = \rho_0$) except at the position of the line current.

Considering the Eqs. (4.4) and (4.7) it is obvious that the normal magnetic induction is continuous at the circular boundary, but for the tangential magnetic field this is less simple to see. The boundary condition for the magnetic field is given to

$$H_{t1} - H_{t2} = J'$$

with the two tangential, ϕ -oriented components of the magnetic field and the z -directed current sheet J' . In this way the current sheet J' represents the line current at (ρ_0, ϕ_0) . Without any limitations, ϕ_0 is set to 0 zero to simplify the further calculations.

With Eqs. (4.5) and (4.8) the expression for the current sheet J' reads as

$$J' = -\frac{I}{2\pi} \frac{1}{\rho_0} \left[1 + 2 \sum_{n=1}^{\infty} \cos(n\phi) \right]. \quad (4.9)$$

By proving the identity of the expression in squared brackets with the 2π -periodic DIRAC-delta-function $\delta(\phi)$, it is also possible to show the continuity of the tangential magnetic field. Therefore the method of orthogonal expansion is used:

$$\delta(\phi) = A_0 + \sum_{n=1}^{\infty} A_n \cos n\phi \quad (4.10)$$

$$\begin{aligned} \Leftrightarrow \int_{-\pi}^{\pi} \delta(\phi) \cos(m\phi) d\phi &= \int_{-\pi}^{\pi} A_0 \cos(m\phi) d\phi + \sum_{n=1}^{\infty} A_n \int_{-\pi}^{\pi} \cos n\phi \cos(m\phi) d\phi \\ \Leftrightarrow 1 &= \begin{cases} 2\pi A_0 & m = 0 \\ \pi A_m & m = n, m \neq 0 \end{cases} \end{aligned} \quad (4.11)$$

With the constants determined in (4.11) equation (4.10) yields the expression of the brackets divided by 2π . *q.e.d.*

4.2 Ideal Geometries

The main issues for the optimization of a coil cross section are field quality and obtainable main field. Both can be manipulated by the number of conductors used and their positioning. Nevertheless, these quantities are also depending on a large number of other factors, which, *e.g.*, give restrictions to the possible conductor positions or are just intrinsic in the design of the used cable, strand or filament. Thus a magnet made of cables is *a priori* never ideal and for a given cable an optimum has to be found in order to meet the needs.

Although ideal geometries cannot be built, their magnetic properties shall be derived in order to study different questions of superconducting magnets while reducing the number of influencing factors. Commonly known are the geometry of a circular current layer with an angular dependency of $\cos(\theta)$ and the geometry of two intersecting ellipses which shall be simplified to two intersecting circles.

4.2.1 Cos($n\theta$)-Geometry

A current layer of $\cos(\theta)$ angular dependency creates an ideal dipolar field in the inner current free region. Furthermore a current layer of $\cos(n\theta)$ angular dependency creates a perfect field of the n^{th} perfect multipole magnet like the quadrupole, sextupole and so on. In order to calculate such geometries first the field and the vector potential of a current sheet are calculated and then the current sheets are superimposed in order to get the field of a current carrying tube of inner radius a and outer radius b .

Current Sheet

Starting more general a current sheet J' of radius ρ_0 and an angular dependency $\cos(n\theta)$ is considered.

$$\mathbf{J}' = J'_0 \cos(n\theta) \mathbf{e}_z$$

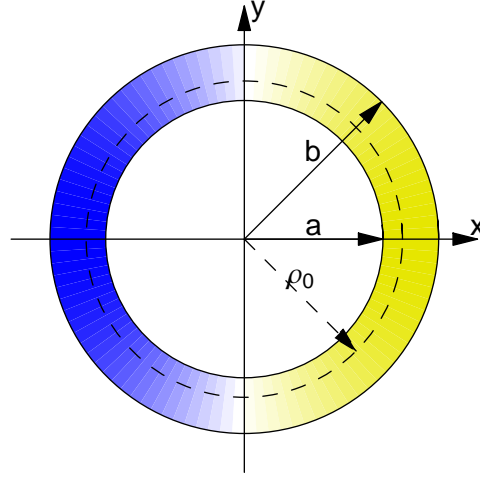


Figure 4.2: Geometry of a so-called ideal $\cos \theta$ -dipole. The colors indicate the distribution of the current density (left negative, right positive).

Using the general solution of the LAPLACE equation in cylindrical coordinates and taking out all singularities and unused constants yields one approach for the area inside the current sheet $\mathbf{A}_{O,1}$ and one for the outside area $\mathbf{A}_{O,2}$.

$$\mathbf{A}_{O,1} = \sum_{m=1}^{\infty} C_m \left(\frac{\rho}{\rho_0} \right)^m \cos(m\phi) \mathbf{e}_z, \quad (4.12)$$

$$\mathbf{A}_{O,2} = \sum_{m=1}^{\infty} D_m \left(\frac{\rho_0}{\rho} \right)^m \cos(m\phi) \mathbf{e}_z. \quad (4.13)$$

Then the field of magnetic induction is given by:

$$\mathbf{B}_{O,1} = - \sum_{m=1}^{\infty} \frac{C_m}{\rho_0} m \left(\frac{\rho}{\rho_0} \right)^{m-1} (\sin(m\phi) \mathbf{e}_\rho + \cos(m\phi) \mathbf{e}_\phi), \quad (4.14)$$

$$\mathbf{B}_{O,2} = - \sum_{m=1}^{\infty} \frac{D_m}{\rho_0} m \left(\frac{\rho_0}{\rho} \right)^{m+1} (\sin(m\phi) \mathbf{e}_\rho - \cos(m\phi) \mathbf{e}_\phi). \quad (4.15)$$

Fulfilling the boundary conditions

$$\mathbf{B}_{O,1} \cdot \mathbf{n} = \mathbf{B}_{O,2} \cdot \mathbf{n}, \quad (4.16)$$

$$\mathbf{H}_{O,2} \cdot \mathbf{t} - \mathbf{H}_{O,1} \cdot \mathbf{t} = J', \quad (4.17)$$

where \mathbf{n} denotes a vector normal and \mathbf{t} a vector tangential to the boundary. This yields

$$C_n = D_n = \frac{\mu_0 J'_0}{2n} \rho_0, \quad (4.18)$$

$$C_m = D_m = 0, \quad n \neq m. \quad (4.19)$$

So the field of the n^{th} ideal multipole magnet $\mathbf{B}_O^{(n)}$ build by a $\cos(n\theta)$ current sheet is given by:

$$\mathbf{B}_{O,1}^{(n)} = -\frac{\mu_0 J'_0}{2} \left(\frac{\rho}{\rho_0} \right)^{n-1} (\sin(n\phi) \mathbf{e}_\rho + \cos(n\phi) \mathbf{e}_\phi), \quad (4.20)$$

$$\mathbf{B}_{O,2}^{(n)} = -\frac{\mu_0 J'_0}{2} \left(\frac{\rho_0}{\rho} \right)^{n+1} (\sin(n\phi) \mathbf{e}_\rho - \cos(n\phi) \mathbf{e}_\phi). \quad (4.21)$$

For the more interesting dipole this can be further simplified and yields

$$\mathbf{B}_{O,1} = -\frac{\mu_0 J'_0}{2} \mathbf{e}_y, \quad (4.22)$$

$$\mathbf{B}_{O,2} = -\frac{\mu_0 J'_0}{2} \left(\frac{\rho_0}{\rho} \right)^2 (\sin(2\phi) \mathbf{e}_x - \cos(2\phi) \mathbf{e}_y). \quad (4.23)$$

The field of magnetic induction of some lower order $\cos(n\theta)$ current sheets are shown in fig. 4.3. It can be seen that the field strength (shading) is only radial dependent.

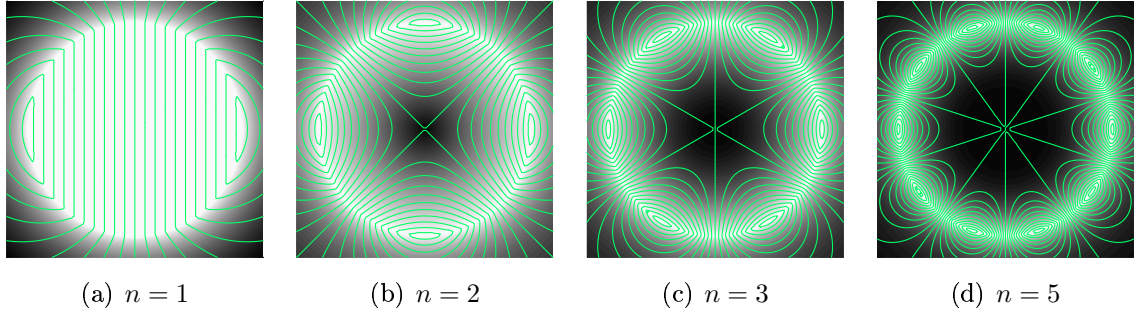


Figure 4.3: The field lines and modulus of some lower order $\cos(n\theta)$ current sheets.

Ideal Dipole of Finite Thickness

A tube of finite thickness and finite inner radius with a $\cos \theta$ current distribution as shown in fig. 4.2 can be derived from the current sheet solution by superimposing an infinite number of sheets with different radii or by simply integrating the vector potential respectively the field. Therefore the following substitution is done

$$J'_0 \rightarrow J_0 \, d\rho_0.$$

Now the solution for the vector potential consists of three parts: One inside the tube denoted by \mathbf{A}_1 , one where the current density is located denoted by \mathbf{A}_2 and one outside and also very far away from the tube denoted by \mathbf{A}_3 . For inside the tube the solution is

simply given by the integral of all $\mathbf{A}_{O,1}$ for all radii from a to b and so is the solution for outside applying the term $\mathbf{A}_{O,2}$.

$$\begin{aligned}\mathbf{A}_1 &= \int_a^b \mathbf{A}_{O,1} d\rho_0 \\ &= \frac{\mu_0 J_0}{2} (b-a) \rho \cos(\phi) \mathbf{e}_z,\end{aligned}\tag{4.24}$$

$$\begin{aligned}\mathbf{A}_3 &= \int_a^b \mathbf{A}_{O,2} d\rho_0 \\ &= \frac{\mu_0 J_0}{6} (b^3 - a^3) \frac{1}{\rho} \cos(\phi) \mathbf{e}_z.\end{aligned}\tag{4.25}$$

For the solution between the boundaries of the tube the integrals are just evaluated up to the radius where the field is needed and so the solution can be written as:

$$\begin{aligned}\mathbf{A}_2 &= \int_a^\rho \mathbf{A}_{O,2} d\rho_0 + \int_\rho^b \mathbf{A}_{O,1} d\rho_0 \\ &= \frac{\mu_0 J_0}{2} \left[\frac{1}{3} (\rho^3 - a^3) \frac{1}{\rho} + (b - \rho) \rho \right] \cos(\phi) \mathbf{e}_z.\end{aligned}\tag{4.26}$$

The expression for the magnetic induction is given by:

$$\mathbf{B}_1 = -\frac{\mu_0 J_0}{2} (b-a) \mathbf{e}_y,\tag{4.27}$$

$$\mathbf{B}_2 = -\frac{\mu_0 J_0}{2} (b-\rho) \mathbf{e}_y - \frac{\mu_0 J_0}{6} (\rho^3 - a^3) \frac{\sin(2\phi) \mathbf{e}_x - \cos(2\phi) \mathbf{e}_y}{\rho^2},\tag{4.28}$$

$$\mathbf{B}_3 = -\frac{\mu_0 J_0}{6} (b^3 - a^3) \frac{\sin(2\phi) \mathbf{e}_x - \cos(2\phi) \mathbf{e}_y}{\rho^2}.\tag{4.29}$$

The field inside the tube depends only on the thickness of the current sheet, but not on the total size.

Figure 4.4 shows the field of magnetic induction for an ideal $\cos\theta$ dipole. It can be seen that the field strength varies heavily within the coil cross section from the maximum to zero field.

4.2.2 Intersecting Circles

A second way to obtain an ideal dipole field is to use two intersecting circles of homogeneous but oppositely directed current density. In the area where both circles overlap the superimposition yields zero current and a homogeneous field. The constant current density in the current carrying areas is one interesting property of this geometry which could be used for modeling some properties of real coils.

The field of magnetic induction and the vector potential is determined by calculating both quantities for a single circle and then adding the expressions for two shifted circles.

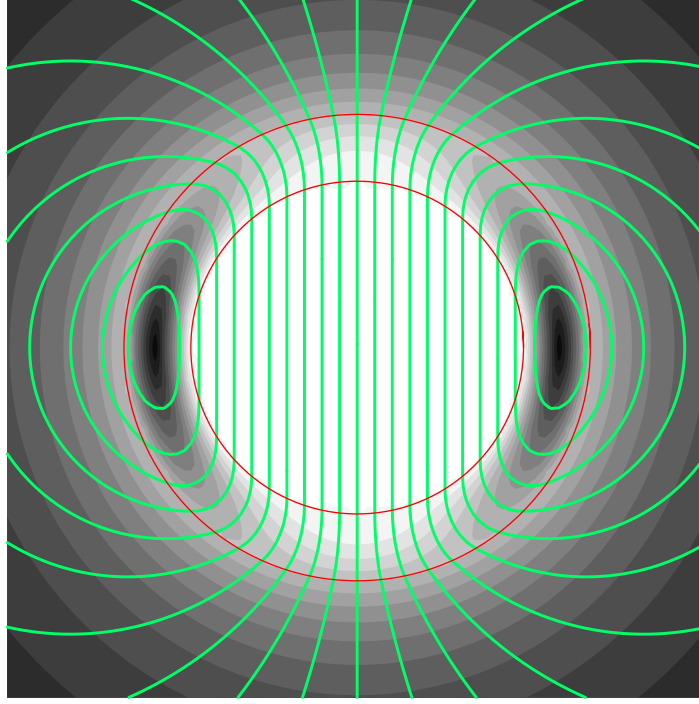


Figure 4.4: Field lines and modulus of the magnetic induction of an ideal $\cos \theta$ dipole. The field in the aperture is homogeneous. The field in the current layer varies heavily from maximum to zero field.

Circle of Homogeneous Current Density

A circular cylinder of radius a and homogeneous current density J is considered. The magnetic field can be calculated easily from AMPERE's law $\iint_A \mathbf{J} \, d\mathbf{A} = \oint_{\partial A} \mathbf{H} \, ds$. With the permeability of empty space the field of magnetic induction $\mathbf{B}_{||}$ is given by

$$\mathbf{B}_{||}(\rho) = \frac{\mu_0 J a}{2} \mathbf{e}_\phi \begin{cases} \frac{\rho}{a} & \rho \leq a \\ \frac{a}{\rho} & \rho > a \end{cases}. \quad (4.30)$$

In order to have a complete set of expressions and to be able to draw field lines, the magnetic vector potential $\mathbf{A}_{||}$ is calculated by radial integration of the negative azimuthal field.

$$\mathbf{A}_{||}(\rho) = -\frac{\mu_0 J}{4} a^2 \mathbf{e}_z \begin{cases} \left(\frac{\rho}{a}\right)^2 & \rho \leq a \\ \ln\left(\frac{a}{\rho}\right) + 1 & \rho > a \end{cases}. \quad (4.31)$$

Two Intersecting Circles

The geometry of two intersecting circles is shown in fig. 4.5. The centers of the two circles of radius a are shifted by c in opposite directions. This shift shall be denoted as displacement.

Both, vector potential and field of magnetic induction are simply given by superimposing

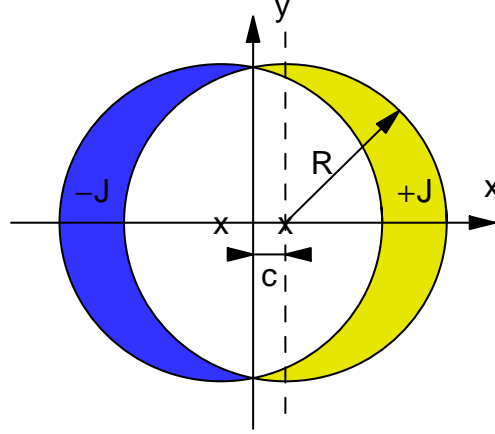


Figure 4.5: Geometry of two intersecting circles.

the terms of the displaced circles.

$$\mathbf{A} = \mathbf{A}_{||}(x - c, y) - \mathbf{A}_{||}(x + c, y), \quad (4.32)$$

$$\mathbf{B} = \mathbf{B}_{||}(x - c, y) - \mathbf{B}_{||}(x + c, y). \quad (4.33)$$

For a more detailed calculation of the field of magnetic induction the space is split up into three different parts: The area inside two circles denoted by 1, the area inside one circle denoted by 2 and the area outside both circles denoted by 3.

With the relations in appendix A.1 the field derived for one circle can be expressed in cartesian coordinates. In this way the field of magnetic induction of two intersecting circles is given by

$$\mathbf{B}_1(x, y) = -\mu_0 c J \mathbf{e}_y, \quad (4.34)$$

$$\begin{aligned} \mathbf{B}_{2,x<0}(x, y) &= \frac{\mu_0 J a}{2} \left[\left(\frac{y}{a} - \frac{ay}{(x - c)^2 + y^2} \right) \mathbf{e}_x \right. \\ &\quad \left. - \left(-\frac{x + c}{a} + \frac{a(x - c)}{(x - c)^2 + y^2} \right) \mathbf{e}_y \right], \end{aligned} \quad (4.35)$$

$$\begin{aligned} \mathbf{B}_{2,x>0}(x, y) &= \frac{\mu_0 J a}{2} \left[\left(-\frac{y}{a} + \frac{ay}{(x + c)^2 + y^2} \right) \mathbf{e}_x \right. \\ &\quad \left. - \left(\frac{x - c}{a} - \frac{a(x + c)}{(x + c)^2 + y^2} \right) \mathbf{e}_y \right], \end{aligned} \quad (4.36)$$

$$\begin{aligned} \mathbf{B}_3(x, y) &= \mu_0 J \left[\left(\frac{y}{(x + c)^2 + y^2} - \frac{y}{(x - c)^2 + y^2} \right) \mathbf{e}_x \right. \\ &\quad \left. + \left(\frac{x - c}{(x - c)^2 + y^2} - \frac{x + c}{(x + c)^2 + y^2} \right) \mathbf{e}_y \right]. \end{aligned} \quad (4.37)$$

The field inside the two circles is homogeneous and only depending on the displacement c of the center of the two circles. The radius a determines the size of the aperture.

Figure 4.6 shows the field of the magnetic induction for a dipole resulting from two intersecting circles. It can be seen that the field strength varies heavily within the current carrying domain from the maximum field to zero field.

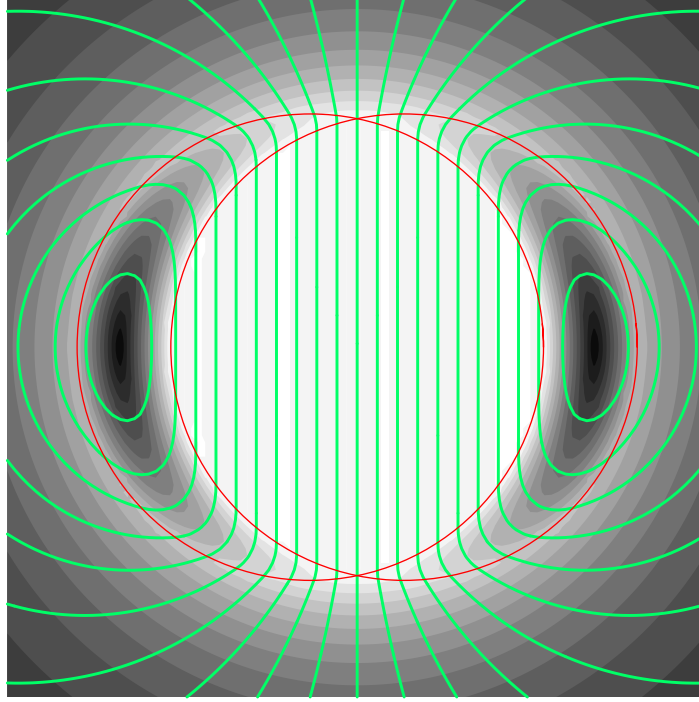
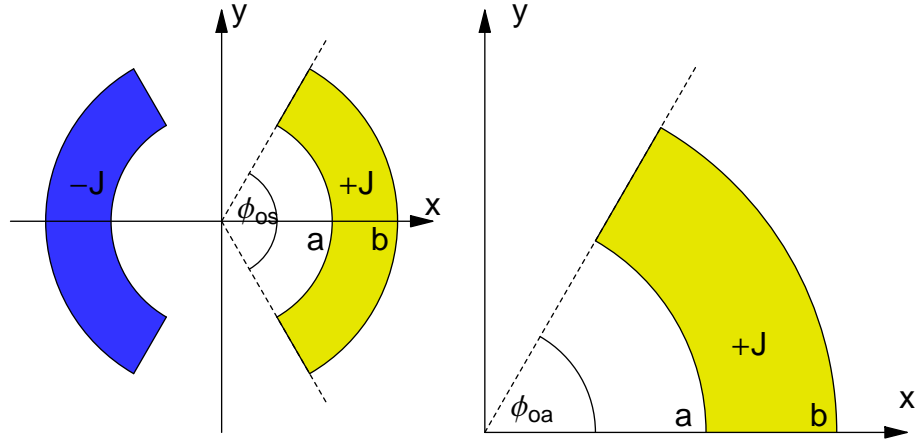


Figure 4.6: Field lines and modulus of the magnetic induction of an ideal dipole made of two intersecting circles. The field in the aperture is homogeneous. The field in the current carrying domain varies heavily from maximum to zero field.

4.3 Analytic Calculation of a Current Shell

After the introduction of geometries producing a perfect dipole field, an analytic but not ideal model of a dipole coil cross section is presented. This geometry consists of two radial current shells of opposite orientations as shown in fig. 4.7 a). The model is not representing the fact that the coil cross section of the studied magnet will be made of keystoneed, so-called RUTHERFORD cable. Since the keystoneing is much smaller than required to perfectly approximate a circular arc, the alignment of most of the cables is not radial. Nevertheless, it can be considered as a good approximation.

For the calculation of the current shell as shown in fig. 4.7 a) first only one quarter is considered. The geometry is shown in fig. 4.7 b) and is denoted as a current arc. The



(a) Symmetric current shell with opening angle ϕ_{os} and homogeneous constant current density J .

(b) Current arc which is an asymmetric but elementary part of the current shell geometry. The current density is z -directed.

Figure 4.7: Geometry of a current shell.

magnetic properties of this geometry can be varied by the geometrical quantities as the inner and outer radius denoted by a and b , the opening angle denoted by ϕ_{oa} and the z -directed current density denoted by J .

By combining and superimposing the vector potential of the current arc, a large number of different geometries can be calculated. In this way a very common analytic design for a dipole without sextupole and decapole component, denoted as *No- B_3 -No- B_5 -Coil*, can be derived and is shown below.

4.3.1 Current Arc

The field of the geometry as shown in fig. 4.7 b) can be calculated by means of BIOT-SAVART's law. A second and more practical way with respect to the calculation of multipole errors is to construct the current density of small line currents and to use the FOURIER expansion. In this way the multipole errors are indirectly calculated and the integrals are easily analytically solvable.

In section 3.2 the vector potential of a single line current is derived and the two expressions (4.3) and (4.6) can be used while replacing the current I by the product of the current density J and the differential area element $\rho_0 d\phi_0 d\rho_0$. This yields two differential vector potentials: $d\mathbf{A}_{|,(\rho_0,\phi_0)}^{\rho < \rho_0}$ for radii smaller than the radial position of the source point

4.3. Analytic Calculation of a Current Shell

and $d\mathbf{A}_{|,(\rho_0,\phi_0)}^{\rho>\rho_0}$ for bigger radii.

$$d\mathbf{A}_{|,(\rho_0,\phi_0)}^{\rho<\rho_0} = -\frac{\mu_0 J}{2\pi} \left[\ln \left(\frac{\rho_0}{R_0} \right) - \sum_{n=1}^{\infty} \frac{1}{n} \left(\frac{\rho}{\rho_0} \right)^n \cos(n(\phi - \phi_0)) \right] \rho_0 d\phi_0 d\rho_0 \mathbf{e}_z \quad (4.38)$$

$$d\mathbf{A}_{|,(\rho_0,\phi_0)}^{\rho>\rho_0} = -\frac{\mu_0 J}{2\pi} \left[\ln \left(\frac{\rho}{R_0} \right) - \sum_{n=1}^{\infty} \frac{1}{n} \left(\frac{\rho_0}{\rho} \right)^n \cos(n(\phi - \phi_0)) \right] \rho_0 d\phi_0 d\rho_0 \mathbf{e}_z \quad (4.39)$$

The vector potential of the current arc \mathbf{A}_j can be calculated by integrating the differential vector potentials over the whole current carrying area. Therefore the space is radially divided into three subspaces. The subspace below the current arc ($\rho < a < b$) which is denoted by 1, the area where the current density is located ($a < \rho < b$) which is denoted by 2 and the subspace above the current arc ($a < b < \rho$) which is denoted by 3.

$$\mathbf{A}_{j,1} = \int_a^b \int_0^{\phi_{oa}} d\mathbf{A}_{|,(\rho_0,\phi_0)}^{\rho<\rho_0} \rho_0 d\phi_0 d\rho_0 \quad (4.40)$$

$$= \mathbf{A}_{\text{inner}}(\rho_l = a) \quad (4.41)$$

$$\mathbf{A}_{j,2} = \int_a^b \int_0^{\phi_{oa}} d\mathbf{A}_{|,(\rho_0,\phi_0)}^{\rho<\rho_0} \rho_0 d\phi_0 d\rho_0 + \int_a^\rho \int_0^{\phi_{oa}} d\mathbf{A}_{|,(\rho_0,\phi_0)}^{\rho>\rho_0} \rho_0 d\phi_0 d\rho_0 \quad (4.42)$$

$$= \mathbf{A}_{\text{inner}}(\rho_l = \rho) + \mathbf{A}_{\text{outer}}(\rho_u = \rho) \quad (4.43)$$

$$\mathbf{A}_{j,3} = \int_a^b \int_0^{\phi_{oa}} d\mathbf{A}_{|,(\rho_0,\phi_0)}^{\rho>\rho_0} \rho_0 d\phi_0 d\rho_0 \quad (4.44)$$

$$= \mathbf{A}_{\text{outer}}(\rho_u = b) \quad (4.45)$$

The integral over the inner differential vector potential for a variable lower boundary $\mathbf{A}_{\text{inner}}(\rho_l)$ yields:

$$\begin{aligned} \mathbf{A}_{\text{inner}}(\rho_l) &= -\frac{\mu_0 J}{4\pi} \phi_{oa} \left[b^2 \left(\ln \left(\frac{b}{R_0} \right) - \frac{1}{2} \right) - \rho_l^2 \left(\ln \left(\frac{\rho_l}{R_0} \right) - \frac{1}{2} \right) \right] \mathbf{e}_z \\ &+ \frac{\mu_0 J}{2\pi} \sum_{n=1}^{\infty} \left[\frac{\rho^n \sin(n\phi) - \sin(n(\phi - \phi_{oa}))}{n} \mathbf{e}_z \begin{cases} b - \rho_l & n = 1 \\ \ln \left(\frac{b}{\rho_l} \right) & n = 2 \\ \frac{1}{n-2} \left(\frac{1}{\rho_l^{n-2}} - \frac{1}{b^{n-2}} \right) & n > 2 \end{cases} \right] \end{aligned} \quad (4.46)$$

The integral over the outer differential vector potential for a variable upper boundary $\mathbf{A}_{\text{outer}}(\rho_u)$ yields:

$$\begin{aligned} \mathbf{A}_{\text{outer}}(\rho_u) &= -\frac{\mu_0 J}{4\pi} (\rho_u^2 - a^2) \phi_{oa} \ln \left(\frac{\rho}{R_0} \right) \mathbf{e}_z \\ &+ \frac{\mu_0 J}{2\pi} \sum_{n=1}^{\infty} \frac{1}{n} \frac{1}{\rho^n} \frac{\sin(n\phi) - \sin(n(\phi - \phi_{oa}))}{n} \frac{1}{n+2} (\rho_u^{n+2} - a^{n+2}) \mathbf{e}_z \end{aligned} \quad (4.47)$$

Figure 4.8 shows the field of magnetic induction for current arcs of different opening angles.

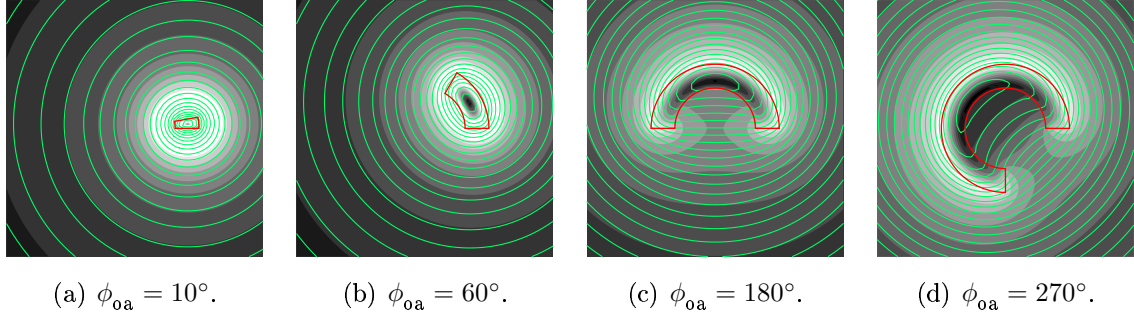


Figure 4.8: The magnetic induction of a current arc of different opening angles ϕ_{oa} . The gray scaling indicates the field modulus and the lines represent the field lines. For small angles the field is similar to the field of a single line current. For an angle of 60° the field inside the current area, approximately in the center, is minimum. For 270° the field almost vanishes inside the c-shape.

4.3.2 Symmetric Current Shell

The vector potential of a symmetric current shell can be constructed by superimposing the result of the current arc \mathbf{A}_{ζ} . The symmetric current shell is build of two arcs of oppositely directed, homogeneous current densities, symmetric to the y -axis. The opening angle is denoted by $\phi_{\text{os}} = 2\phi_{\text{oa}}$.

$$\mathbf{A}_{(\zeta)}(\rho, \phi) = \mathbf{A}_{\zeta}(\rho, \phi) + \mathbf{A}_{\zeta}(\rho, -\phi) - \mathbf{A}_{\zeta}(\rho, \pi + \phi) - \mathbf{A}_{\zeta}(\rho, \pi - \phi) \quad (4.48)$$

For the field of magnetic induction it is necessary to consider in addition to the geometrical symmetries the direction of the field of the single current arcs. This yields:

$$\mathbf{B}_{(\zeta)}(\rho, \phi) = \mathbf{B}_{\zeta}(\rho, \phi, \phi_{\text{oa}}) - \mathbf{B}_{\zeta}(\rho, -\phi, -\phi_{\text{oa}}) + \mathbf{B}_{\zeta}(\rho, \pi + \phi, \phi_{\text{oa}}) - \mathbf{B}_{\zeta}(\rho, \pi - \phi, -\phi_{\text{oa}}) \quad (4.49)$$

Figure 4.9 shows the field of magnetic induction for different opening angles ϕ_{os} . It can be seen that the homogeneity of the field inside the aperture is best for an opening angle of 120° . All geometries show a field maximum at the inner corner and a minimum at approximately the center of the current region on the x -axis (field drain).

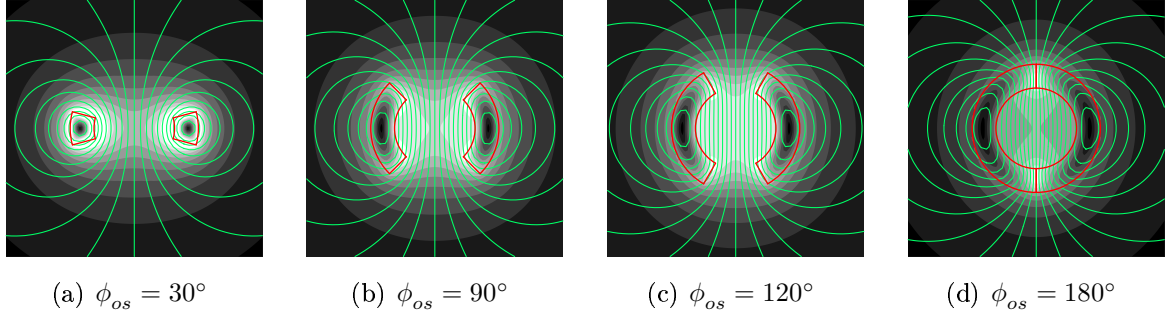


Figure 4.9: Field of magnetic induction of the symmetric current shells of different opening angles ϕ_{os} . The grayscale indicates the field modulus and the light lines represent the field lines.

4.3.3 The No- B_3 -No- B_5 -Coil

As the field of any current density can be derived by integrating the field of infinitely small current pieces, the field error of such a geometry can also be calculated by integrating the field errors of these pieces. From Eq. (3.8) the multipole error B_n of a symmetric coil can be expressed as:

$$B_n = -2 \frac{\mu_0 J}{\pi} \iint_{A_{coil}} \left(\frac{r_0}{\rho_0} \right)^{n-1} \cos(n\phi_0) d\phi_0 d\rho_0, \quad n = 3, 5, ..$$

Making use of the azimuthal cosine dependency of the multipole errors, some can be suppressed by choosing a design where they cancel out. In this way, any design is free of B_3 if it is symmetric to 30° in the first quadrant.

Starting with a geometry of a symmetric current shell of an opening angle of 120° yields no B_3 . With a current free region symmetric to 30° the multipole error B_5 can be eliminated. Therefore the equation

$$B_5 = 0 = \int_{0^\circ}^{30^\circ - \phi_g} \cos(5\phi_0) d\phi_0 + \int_{30^\circ + \phi_g}^{60^\circ} \cos(5\phi_0) d\phi_0$$

is solved and yields a size of $\phi_g = 6^\circ$. This coil can be constructed by superimposing three current shells. The vector potential is given by:

$$\mathbf{A}_{noB_3noB_5} = \mathbf{A}_{()}(\rho, \phi, \phi_{cs} = 120^\circ) - \mathbf{A}_{()}(\rho, \phi, \phi_{cs} = 72^\circ) + \mathbf{A}_{()}(\rho, \phi, \phi_{cs} = 48^\circ) \quad (4.50)$$

Figure 4.10 shows the field of magnetic induction for a geometry producing no B_3 and B_5 multipole components.

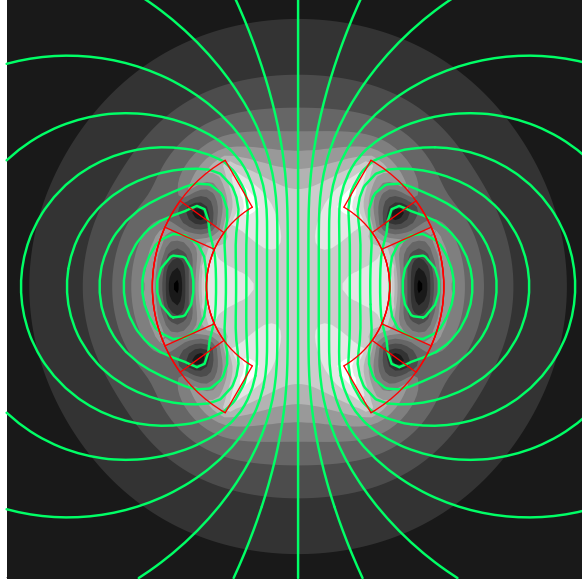


Figure 4.10: Magnetic induction of the geometry producing no B_3 and B_5 multipole component. The grayscale indicates the field modulus and the light lines represent the field lines.

Depending on the application, a startup design for the optimization can be chosen following the principles described above.

4.4 Estimation of the Required Amount of Superconductors for High-field Accelerator Magnets

For the construction of superconducting dipole magnets, different approaches have been studied [21], *e.g.*, the intersecting ellipses, the common coil and the $\cos \theta$ configuration. All these geometries mainly vary in the way how the superconducting cables are distributed around the aperture.

Since the cost of a superconducting magnet depends heavily on the amount of superconducting cable used for the coil winding, it has to be taken into account if different designs are compared and evaluated.

The magnetic field which can be obtained with a certain magnet configuration depends on the powering current and on the maximum allowed current density in the strands. For superconductors the maximum current density depends among other quantities like stress and temperature on the applied magnetic flux density and decreases with increasing field [9]. Therefore a gain in main field strength can only be achieved by increasing the cross sectional area of the coil once the maximum current density is reached.

The cable design also plays a crucial role for the required amount of superconductors. Although the cable consists just of a certain number of strands, the overall current *density* in the cable cross section reduces due the greater cross sectional area. The cable insulation reduces the current density even further. Finally, the maximum current density of the strands is reduced by broken filaments [12], depending on the cabling process and the cable keystoneing.

In the following, the minimum amount of superconductors required for the construction of a dipole of given main field strength and aperture size is derived by means of an ideal dipole model. The result is depicted by applying the specifications of the NED cable [1].

4.4.1 Analytical Model

The superconducting magnet coil is modeled by means of the ideal geometry of two intersecting circles shown in fig. 4.11, where R denotes the radii of the two circles, $2c$ the distance of the centers of the circles and J the modulus of the oppositely directed and homogeneous current densities. For this configuration the peak field on conductor is located at the boundary of the aperture and it is equal to the center/main field.

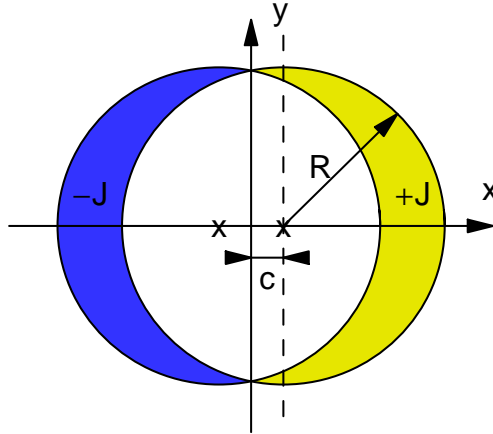


Figure 4.11: Ideal dipole geometry of two intersecting circles.

The center field of two intersecting circles is given by

$$B = \mu_0 J c, \quad (4.51)$$

and depends only on the distance of the circle centers $2c$ and the modulus of the current density J . As will be shown later, the radius of the circles R results from the chosen aperture size.

By incorporating the superconducting coil into an iron yoke the obtainable field for a given excitation current is enhanced. The effect of the iron yoke can be described by a

constant offset to the main/peak field which is considered by means of a constant k_I . This way the peak field of such a geometry inside an iron yoke reads:

$$B_{\text{peak}} = \mu_0 k_I J c. \quad (4.52)$$

The maximum current density a superconductor is able to carry depends on temperature and applied magnetic induction. It is denoted by the critical current density $J_c(B, T)$. For this estimation the linear approximation of the critical current density in the superconducting strands at high field is used keeping the temperature constant. Note that this is different from the commonly used critical current density in the non-copper area of the strand¹.

$$J_{\text{strand}}(B) = J_0 - \frac{\Delta J}{\Delta B}(B - B_0) \quad (4.53)$$

where J_0 denotes the critical current density at a magnetic flux density B_0 and $\Delta J/\Delta B$ is the slope of the critical current density curve at B_0 .

This way the estimation can be carried out assuming a dipole geometry built of superconducting strands only. By considering the reduction of the maximum overall current density in superconducting cables due to the greater cross sectional area of the cable, the cable insulation, and the degradation due to cabling, the estimation can be carried out for realistic cable configurations. This way, the effective maximum overall current density which depends on the peak field in the conductor is given to

$$J_{\text{eff}}(B_{\text{peak}}) = k J_{\text{strand}}(B_{\text{peak}}) \quad (4.54)$$

with

$$k = k_{\text{cab}} k_{\text{ins}} k_{\text{deg}}, \quad (4.55)$$

where the factor k_{cab} is the ratio of the area covered by strands to the total area of the cable and k_{ins} is given by the ratio non-insulated to insulated areas in the cable. The degradation due to cabling k_{deg} is taken from the cable specifications.

By applying the maximum current density, Eq. (4.54), to the obtainable peak field of two intersecting circles, Eq. (4.52), the required circle off-centering $2c$ is given to:

$$c = \frac{B_{\text{peak}}}{\mu_0 \lambda J_{\text{strand}}(B_{\text{peak}})}. \quad (4.56)$$

The influence of the iron yoke and the reduction of the current density in the cables is expressed by the factor $\lambda = k_I k$. This result is independent of the size of the aperture and the radii of the two circles.

¹The critical current density in the strand J_{strand} can be obtained from the current density in the non-copper area $J_{\text{non-Cu}}$ by multiplication with the filling factor:

$$J_{\text{strand}}(B) = \frac{1}{1 + \frac{C_{\text{Cu}}}{\text{non-Cu}}} J_{\text{non-Cu}}(B)$$

where $\frac{C_{\text{Cu}}}{\text{non-Cu}}$ denotes the copper to non-copper ratio.

The aperture radius r_A is given by the greatest circle which can be nested in the center current free region. This way, for a given aperture radius r_A and displacement c , the radius of the intersecting circles R results to

$$R = c + r_A. \quad (4.57)$$

All parameters of the ideal intersecting circles configuration are fully determined and the required amount of superconductors can be calculated by means of the total area.

For the calculation of the total cross sectional area A_{con} covered by the current density J , *i.e.*, superconducting strand material, the geometrical relations are shown in fig. 4.12. One quarter of the total area indicated by $\langle 1 \rangle$ is given by the difference of the two sectors

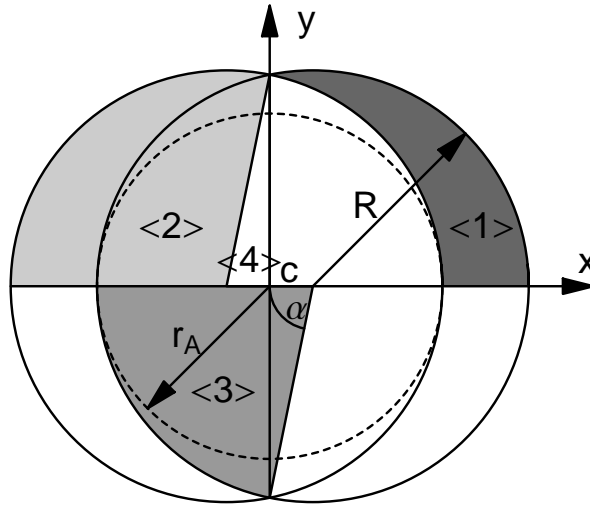


Figure 4.12: Geometry of two intersecting circles. Using the two shaded areas and the two triangles the area covered by the current density J can be calculated.

of a circle indicated by $\langle 2 \rangle$ and $\langle 3 \rangle$ and twice the area of the triangle indicated by $\langle 4 \rangle$.

$$A_{\text{con}} = 4(A_{\langle 2 \rangle} - A_{\langle 3 \rangle} + 2A_{\langle 4 \rangle}). \quad (4.58)$$

The area of the sectors can be easily calculated by their fraction of a full circle and the triangle is given by means of PYTHAGOREAN's law:

$$\begin{aligned} A_{\langle 2 \rangle} &= \frac{\pi - \alpha}{2} R^2, \\ A_{\langle 3 \rangle} &= \frac{\alpha}{2} R^2, \\ A_{\langle 4 \rangle} &= \frac{1}{2} c \sqrt{R^2 - c^2}. \end{aligned}$$

By expressing the angle α in terms of the two quantities R and c the total area is finally given by:

$$A_{\text{con}}(c, R) = 4 \left[\left(\frac{\pi}{2} - \arccos \left(\frac{c}{R} \right) \right) R^2 + c \sqrt{R^2 - c^2} \right]. \quad (4.59)$$

With Eq. (4.57) the total area given in Eq. (4.59) can be written as

$$A_{\text{con}}(c, r_A) = 4 \left[\left(\frac{\pi}{2} - \arccos \left(\frac{c}{c + r_A} \right) \right) (c + r_A)^2 + cr_A \sqrt{2 \frac{c}{r_A} + 1} \right]. \quad (4.60)$$

Note, that this equation merely depends on the aperture radius r_A and the off-centering c which is resulting from the requested strength of the main field in Eq. (4.51).

4.4.2 Graphical Solution

The graphical solution of Eqs. (4.56) and (4.60) is depicted in fig. 4.13 by means of a set of characteristic curves using the strand specifications of the NED cable [1]. The lower diagram gives the value for the distance of the circles to the center c depending on the wanted main/peak field B_{peak} , the critical current density of the used strand J , the reduction of current density due to the used cable and the influence of the iron yoke (both expressed by λ). The upper diagram gives the required cross sectional area A_{con} depending on the aperture radius r_A and the distance c .

The required amount of superconductors can be estimated by means of elementary algebraic operations only: After calculating the factor λ , describing the cable and the influence of the iron yoke, the distance c is determined by the intersection point of the wanted main field and the λ -line. From this point the vertical lines give the parameter c . The total cross sectional area can be read of easily and the number of conductors per quadrant is obtained by division by four times the conductor cross sectional area.

4.4.3 Estimation for NED

The specifications of the NED strand [1] are applied to the approach derived above and the number of strands are calculated for a dipole of 15 T peak field B_{peak} .

Based on the numerical results obtained for the $\cos \theta$ -layer design with 44 mm aperture radius the contribution of the iron yoke to the peak field at maximum excitation is assumed to be of 20% yielding $k_{\text{I}} = 1.2$. The required minimum number of strands for the three aperture diameters used within the NED program are given in tab. 4.1.

Table 4.1: Required minimum number of strands per quadrant for a 15 T dipole made of NED strands.

Aperture diameter r_A in mm	88	130	160
Number of strands	1418	1933	2299

For the $\cos \theta$ -layer design an insulated, keystoneed RUTHERFORD-type cable is used. With the specifications given in [1], the constants describing the reduction of the current density due to the cable geometry can be calculated and yields $k_{\text{cab}} = 0.830$ and $k_{\text{ins}} = 0.838$. The maximum degradation due to cabling is specified to be of 10% taken into account by

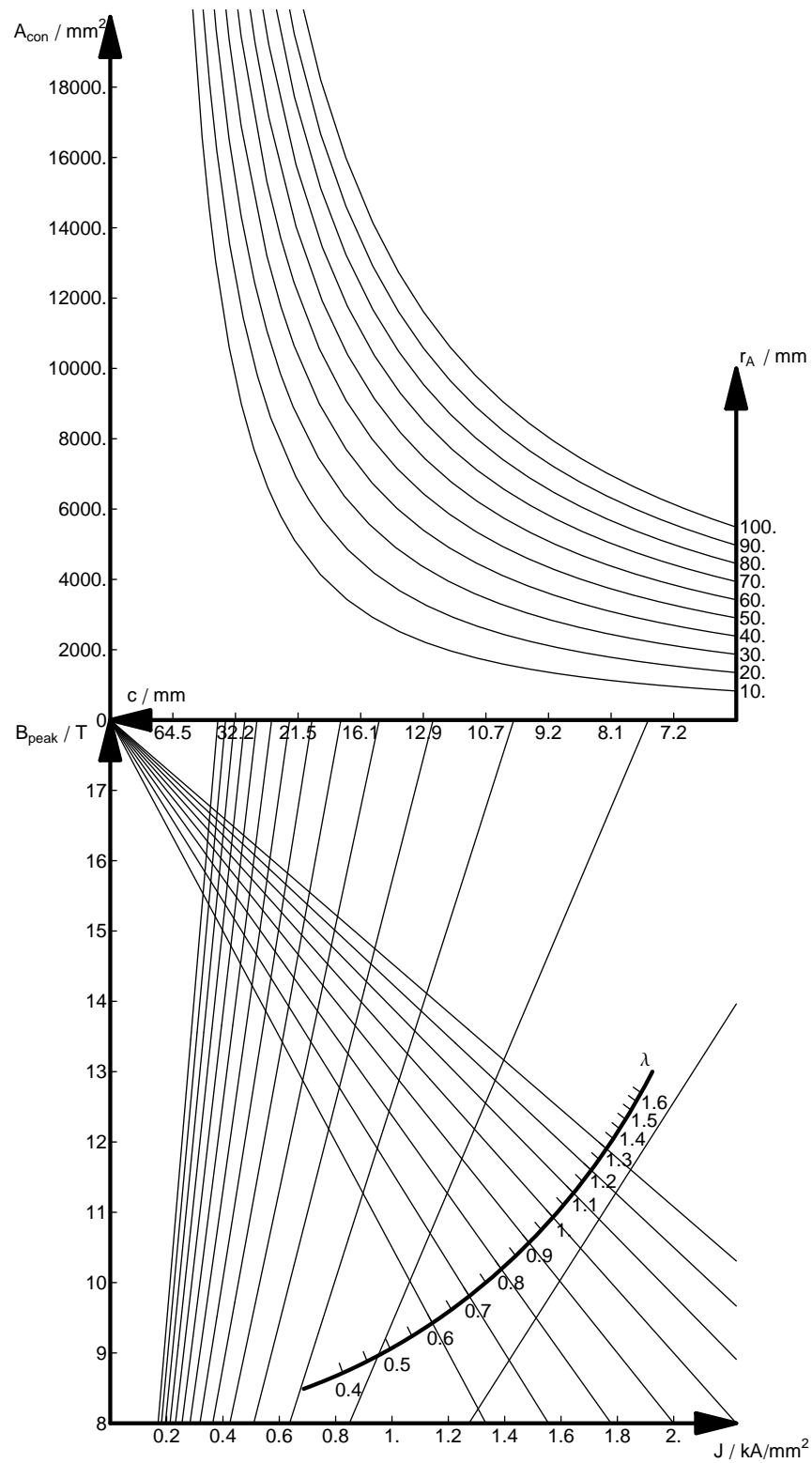


Figure 4.13: Set of characteristic curves for the estimation of the minimum cross sectional area of high-field dipole geometries using the NED strand.

Table 4.2: Required minimum number of conductors per quadrant for a 15 T dipole made of keystone NED cables.

Aperture diameter r_A in mm	88	130	160
Number of conductors (not insulated)	43	57	68
Number of conductors (insulated)	45	60	70

$k_{\text{deg}} = 0.9$. The resulting minimum number of conductors, insulated and non-insulated, are shown in tab. 4.2.

Comparing these results with the results of the preliminary design for NED published by LEROY and VINCENT-VIRY [4], they obtain similar but smaller values in order to reach the same peak field. The comparison with the model of an ideal $\cos \theta$ configuration as used by CASPI [25] yields a greater cross sectional area which also gives a greater number of conductors if it is reduced to an equivalent area of constant current density.

4.4.4 Sensitivity

As one can see from the graphical approach shown in fig. 4.13, for high fields B the distance of the circles $2c$ is very sensitive on small variations of the assumed values. Consequently, the term of the cross sectional area further amplifies these variations.

For the NED 88 mm 15 T dipole the sensitivity of the different parameters is demonstrated. The influence of a variation of $\pm 1\%$ of the values assumed above is calculated and shown in tab. 4.3. It can be seen that the number of conductors scales directly with the wanted peak field. The contribution of the iron yoke and the degradation are also influencing the results. However, changes of the aperture radius, *e.g.*, due to thermal contraction, are negligible.

Table 4.3: Variation of the estimated number of conductors for a change of the assumed values by 1%.

Parameter	Influence on the number of conductors
r_A	$\pm 0.7\%$
λ	$\pm 1.3\%$
B_{peak}	$\pm 8\%$

4.4.5 Influence of the Iron Yoke

The set of characteristic curves is now used to demonstrate the iron yoke contribution on a magnet design applying the rule-of-thumb. As suggested by TODESCO and DEVRED, the iron yoke for the current NED design could be left away in order to cut the saturation induced field errors. This idea is resulting from the facts that firstly the removal of the iron yoke reduces the main field without changing the current density in the conductors.

Secondly, the iron yoke contribution to the total aperture field for the NED design can be compensated up to 3% by an increase of the excitation current in order to keep the peak field value. Their estimations can be fully verified for the NED 88 mm 15 T dipole by means of the shown set of characteristic curves.

From the diagram it can be seen that the missing 3% in main field, nearly 0.5 T, can only be compensated for if the number of superconductors in the cross-section is increased. For the design of the 15 T, 88 mm aperture dipole for NED, nearly 28% more conductors are needed to keep the aperture field if the iron yoke is removed compared to the traditional design with iron yoke. This corresponds to a minimum number of 58 conductors per quadrant which could impossibly be put into the cross section due to space limitations.

4.5 Summary

The magnetic field of the elementary geometry of superconducting magnets, the single line current, was calculated. For an eccentric line current, this result was expressed by means of the FOURIER expansion. By proofing the continuity of the found FOURIER expansion, an expression for the DIRAC-delta-function could be found.

For analytical estimations the magnetic vector potential of two perfect dipole geometries, the intersecting circles and the $\cos(\theta)$ configuration was calculated. More general, the field of a $\cos(n\theta)$ current sheet could be calculated yielding the ideal multipole configurations.

By means of the calculation of an circular arc of homogeneous current density, the field of simple analytic but not ideal dipole configurations could be found. The analytical solution for a dipole geometry made of currents arcs with neither sextupole nor decapole component was obtained.

The intersecting circles geometry was used for the estimation of the minimum number of conductors required to achieve a certain peak or main field, respectively. The approach takes into account the critical current density of the used cable, current density degradations and the influence of the iron yoke.

5 Analytic Models of the Iron Yoke

The superconducting coil of an accelerator magnet is usually surrounded by magnetic material, the iron yoke, in order to enhance the field in the aperture and to reduce the fringe field outside of the magnet. For the calculation of the effect of the iron yoke on the field distribution and field quality of superconducting coils as a first approximation a circular hollow cylinder of high permeable material could be used. In the following the field distribution in such a geometry for one line current will be solved and then be used to derive the imaging method for cylindrical problems and to investigate the influence of the yoke radius and yoke thickness on the field quality and main field strength.

5.1 Circular Hollow Cylinder - Three Arbitrary Materials

A circular hollow cylinder of permeability μ_2 with inner radius a and outer radius b is filled with a material of permeability μ_1 and surrounded by a material of permeability μ_3 . Inside the hollow cylinder one line current I is arbitrarily placed at $x = r_I$ as shown in fig. 5.1.

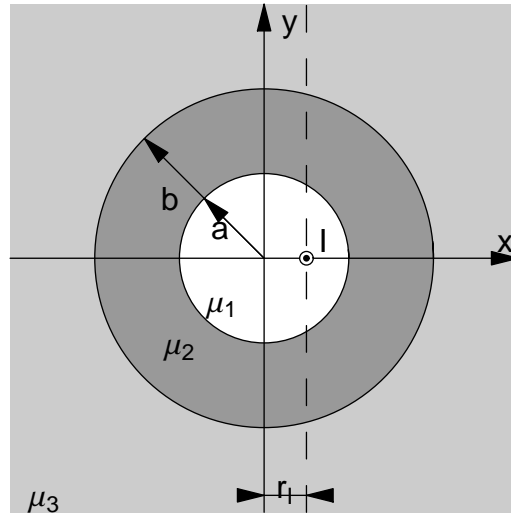


Figure 5.1: Geometry of a circular hollow cylinder of inner radius a and outer radius b . The tube is filled by a material of permeability μ_2 and surrounded by two materials of different permeabilities (μ_1 inside and μ_3 outside).

5.1.1 Potential Approach

The field distribution will be expressed by means of the vector potential \mathbf{A} . For the area denoted by 1 inside the hollow cylinder the vector potential \mathbf{A}_1 consists of the primary potential of the line current \mathbf{A}_l and of the secondary potential $\mathbf{A}^{(1)}$ describing the repercussion of the iron on the inner field. In the areas 2 and 3 the field is created by the line current and the effect of the different materials and is expressed by the potentials $\mathbf{A}_2 = \mathbf{A}^{(2)}$ and $\mathbf{A}_3 = \mathbf{A}^{(3)}$.

$$\mathbf{A}_1 = \mathbf{A}_l + \mathbf{A}^{(1)}.$$

$\mathbf{A}^{(i)}$ with $n = 1, 2, 3$ denotes potential approaches which constants need to be determined in the following.

A z -directed line current can be expressed by a z -directed vector potential. Since all other vector potentials are created by the reaction on the primary potential, all are z -directed, too. Consequently only the z -component of the vector potentials is considered.

In section 4.1 the vector potential of a single line current at an arbitrary radial position r_I was derived and expressed by means of the FOURIER expansion. In order to determine the constants of the approaches the vector potential needs to be evaluated at the inner radius a , *i.e.*, for radii bigger than the position of the line current. For the determination of multipole errors the potential is also needed for smaller radii.

$$\begin{aligned} A_{l,z} &= -\frac{\mu_1 I}{2\pi} \ln \left(\frac{\sqrt{(x - r_I)^2 + y^2}}{R_0} \right) \\ &= -\frac{\mu_1 I}{2\pi} \begin{cases} \ln \left(\frac{r_I}{R_0} \right) - \sum_{n=1}^{\infty} \frac{1}{n} \left(\frac{\rho}{r_I} \right)^n \cos(n\phi) & \rho < r_I \\ \ln \left(\frac{\rho}{R_0} \right) - \sum_{n=1}^{\infty} \frac{1}{n} \left(\frac{r_I}{\rho} \right)^n \cos(n\phi) & \rho > r_I \end{cases}. \end{aligned} \quad (5.1)$$

The secondary potentials can be expressed by the general solution of the LAPLACE-equation in cylindrical coordinates.

$$\begin{aligned} A_z^{(i)} &= \frac{\mu_i I}{2\pi} \left(A_0^{(i)} + B_0^{(i)} \ln \left(\frac{\rho}{R_0} \right) \right) (C_0^{(i)} + D_0^{(i)} \phi) \\ &+ \frac{\mu_i I}{2\pi} \sum_{n=1}^{\infty} \frac{1}{n} \left(A_n^{(i)} \left(\frac{\rho}{r_I} \right)^n + B_n^{(i)} \left(\frac{r_I}{\rho} \right)^n \right) (C_n^{(i)} \cos(n\phi) + D_n^{(i)} \sin(n\phi)). \end{aligned} \quad (5.2)$$

Before the constants of these approaches are determined by fulfilling the boundary conditions, the number of unknowns can be reduced by qualitative thoughts:

One line current placed somewhere on the x -axis is surrounded by circular field lines which are always perpendicular to the x -axis. Although the field distribution is changed by the repercussion of the hollow cylinder, this characteristic will stay unchanged and so the field of the magnetic induction will be only azimuthal for $\phi = 0$ and $\phi = \pi$. For this reason all sine-terms and the linearly ϕ -dependent term vanish.

$$D_0^{(1,2,3)} = 0, \quad (5.3)$$

$$D_n^{(1,2,3)} = 0. \quad (5.4)$$

In area 1 only one line current exists and so there is no singularity in the origin. The vector potential shows finite values.

$$B_0^{(1)} = 0, \quad (5.5)$$

$$B_n^{(1)} = 0. \quad (5.6)$$

For very big radii all fields should vanish and so the term with ρ^n has to be cancelled in area 3.

$$A_n^{(3)} = 0. \quad (5.7)$$

With these first constants the approaches can be reduced and the following constants can be defined:

$$\begin{aligned} L_0^{(1)} &= A_0^{(1)} C_0^{(1)}, & E_n^{(1)} &= A_n^{(1)} C_n^{(1)}, \\ L_0^{(2)} &= A_0^{(2)} C_0^{(2)}, & K_0^{(2)} &= B_0^{(2)} C_0^{(2)}, & E_n^{(2)} &= A_n^{(2)} C_n^{(2)}, & F_n^{(2)} &= A_n^{(2)} C_n^{(2)}, \\ L_0^{(3)} &= A_0^{(3)} C_0^{(3)}, & K_0^{(3)} &= B_0^{(3)} C_0^{(3)}, & F_n^{(3)} &= B_n^{(3)} C_n^{(3)}. \end{aligned}$$

Then the secondary vector potentials read:

$$A_z^{(1)} = \frac{\mu_1 I}{2\pi} \left[L_0^{(1)} + \sum_{n=1}^{\infty} \frac{1}{n} E_n^{(1)} \left(\frac{\rho}{r_I} \right)^n \cos(n\phi) \right], \quad (5.8)$$

$$A_z^{(2)} = \frac{\mu_2 I}{2\pi} \left[L_0^{(2)} + K_0^{(2)} \ln \left(\frac{\rho}{R_0} \right) + \sum_{n=1}^{\infty} \frac{1}{n} \left(E_n^{(2)} \left(\frac{\rho}{r_I} \right)^n + F_n^{(2)} \left(\frac{r_I}{\rho} \right)^n \right) \cos(n\phi) \right] \quad (5.9)$$

$$A_z^{(3)} = \frac{\mu_3 I}{2\pi} \left[L_0^{(3)} + K_0^{(3)} \ln \left(\frac{\rho}{R_0} \right) + \sum_{n=1}^{\infty} \frac{1}{n} F_n^{(3)} \left(\frac{r_I}{\rho} \right)^n \cos(n\phi) \right]. \quad (5.10)$$

5.1.2 Field of Magnetic Induction

The magnetic induction in the three areas is given by the curl of the vector potentials and yields:

$$B_{1,r}^{\rho < r_I} = -\frac{\mu_1 I}{2\pi} \sum_{n=1}^{\infty} (1 + E_n^{(1)}) \frac{\rho^{n-1}}{r_I^n} \sin(n\phi), \quad (5.11)$$

$$B_{1,\phi}^{\rho < r_I} = -\frac{\mu_1 I}{2\pi} \sum_{n=1}^{\infty} (1 + E_n^{(1)}) \frac{\rho^{n-1}}{r_I^n} \cos(n\phi), \quad (5.12)$$

$$B_{1,r}^{\rho > r_I} = -\frac{\mu_1 I}{2\pi} \sum_{n=1}^{\infty} \left(\frac{r_I^n}{\rho^{n+1}} + E_n^{(1)} \frac{\rho^{n-1}}{r_I^n} \right) \sin(n\phi), \quad (5.13)$$

$$B_{1,\phi}^{\rho > r_I} = \frac{\mu_1 I}{2\pi} \frac{1}{\rho} + \frac{\mu_1 I}{2\pi} \sum_{n=1}^{\infty} \left(\frac{r_I^n}{\rho^{n+1}} - E_n^{(1)} \frac{\rho^{n-1}}{r_I^n} \right) \cos(n\phi). \quad (5.14)$$

$$B_{2,r} = -\frac{\mu_2 I}{2\pi} \sum_{n=1}^{\infty} \left(E_n^{(2)} \frac{\rho^{n-1}}{r_I^n} + F_n^{(2)} \frac{r_I^n}{\rho^{n+1}} \right) \sin(n\phi), \quad (5.15)$$

$$B_{2,\phi} = -\frac{\mu_2 I}{2\pi} K_0^{(2)} \frac{1}{\rho} - \frac{\mu_2 I}{2\pi} \sum_{n=1}^{\infty} \left(E_n^{(2)} \frac{\rho^{n-1}}{r_I^n} - F_n^{(2)} \frac{r_I^n}{\rho^{n+1}} \right) \cos(n\phi). \quad (5.16)$$

$$B_{3,r} = -\frac{\mu_3 I}{2\pi} \sum_{n=1}^{\infty} F_n^{(3)} \frac{1}{\rho^{n+1}} \sin(n\phi), \quad (5.17)$$

$$B_{3,\phi} = -\frac{\mu_3 I}{2\pi} K_0^{(3)} \frac{1}{\rho} + \frac{\mu_3 I}{2\pi} \sum_{n=1}^{\infty} F_n^{(3)} \frac{r_I^n}{\rho^{n+1}} \cos(n\phi). \quad (5.18)$$

5.1.3 Fulfilling the Boundary Conditions

All fields have to fulfill the boundary condition of continuous normal magnetic induction due to the zero divergence. Following AMPERE's law the tangential magnetic field is also continuous, if there are no current sheets on the boundary.

For infinite long geometries of which the cross section is considered only, this can be expressed by the vector potential (see appendix A.2.1) as:

$$\mathbf{B}_1|_{\partial_{12}} \cdot \mathbf{n} = \mathbf{B}_2|_{\partial_{12}} \cdot \mathbf{n} \rightarrow A_1|_{\partial_{12}} = A_2|_{\partial_{12}}, \quad (5.19)$$

$$\mathbf{H}_1|_{\partial_{12}} \times \mathbf{n} = \mathbf{H}_2|_{\partial_{12}} \times \mathbf{n} \rightarrow \frac{1}{\mu_1} \frac{\partial \mathbf{A}_1}{\partial n} \Big|_{\partial_{12}} = \frac{1}{\mu_2} \frac{\partial \mathbf{A}_2}{\partial n} \Big|_{\partial_{12}}. \quad (5.20)$$

Here ∂_{12} denotes the boundary between area 1 and 2, \mathbf{n} denotes a normal vector perpendicular to the boundary and $\partial/\partial n$ denotes its normal derivative ($\mathbf{n} \cdot \nabla$).

The considered geometry has one circular boundary at $\rho = a$ and one at $\rho = b$. This yields in general four equations. Furthermore, on the boundary the two vector potentials/magnetic fields are the FOURIER expansion of the same function/quantity and thus show the same coefficients. The four equations can therefore be split up in one set of four equations for each order of the member of the series. More practical, they are split up in one set for the members of order zero and one set for the members of n^{th} order.

The boundary condition $A_{z,1}|_{\rho=a} = A_{z,2}|_{\rho=a}$ yields:

$$L_0^{(1)} - \ln\left(\frac{a}{R_0}\right) = \frac{\mu_2}{\mu_1} \left(L_0^{(2)} + K_0^{(2)} \ln\left(\frac{a}{R_0}\right) \right), \quad (5.21)$$

$$\left(\frac{r_I}{a}\right)^n + E_n^{(1)} \left(\frac{a}{r_I}\right)^n = \frac{\mu_2}{\mu_1} \left(E_n^{(2)} \left(\frac{a}{r_I}\right)^n + F_n^{(2)} \left(\frac{r_I}{a}\right)^n \right). \quad (5.22)$$

The boundary condition $-\frac{1}{\mu_1} \frac{\partial A_{z,1}}{\partial \rho} \Big|_{\rho=a} = -\frac{1}{\mu_2} \frac{\partial A_{z,2}}{\partial \rho} \Big|_{\rho=a}$ yields:

$$\frac{1}{a} = -K_0^{(2)} \frac{1}{a}, \quad (5.23)$$

$$-E_n^{(1)} \frac{a^{n-1}}{r_I^n} + \frac{r_I^n}{a^{n+1}} = -E_n^{(2)} \frac{a^{n-1}}{r_I^n} + F_n^{(2)} \frac{r_I^n}{a^{n+1}}. \quad (5.24)$$

The boundary condition $A_{z,2}|_{\rho=b} = A_{z,3}|_{\rho=b}$ yields:

$$\frac{\mu_2}{\mu_3} \left(L_0^{(2)} + K_0^{(2)} \ln \left(\frac{b}{R_0} \right) \right) = L_0^{(3)} + K_0^{(3)} \ln \left(\frac{b}{R_0} \right), \quad (5.25)$$

$$\frac{\mu_2}{\mu_3} \left(E_n^{(2)} \left(\frac{b}{r_I} \right)^n + F_n^{(2)} \left(\frac{r_I}{b} \right)^n \right) = F_n^{(3)} \left(\frac{r_I}{b} \right)^n. \quad (5.26)$$

The boundary condition $-\frac{1}{\mu_2} \frac{\partial A_{z,2}}{\partial \rho}|_{\rho=b} = -\frac{1}{\mu_3} \frac{\partial A_{z,3}}{\partial \rho}|_{\rho=b}$ yields:

$$-K_0^{(2)} \frac{1}{b} = -K_0^{(3)} \frac{1}{b}, \quad (5.27)$$

$$-E_n^{(2)} \frac{b^{n-1}}{r_I^n} + F_n^{(2)} \frac{r_I^n}{b^{n+1}} = F_n^{(3)} \frac{r_I^n}{b^{n+1}}. \quad (5.28)$$

The two systems, one consisting of the four equations (5.21), (5.23), (5.25) and (5.27), the other consisting of the four equations (5.22), (5.24), (5.26) and (5.28), are solved either by GAUSS' method or by inversion of the matrix of the linear system. The system of the members of zero order is over determined and one of the three constants $L_0^{(1,2,3)}$ is free of choice. Following the argumentation in appendix A.2.2 the constant $L_0^{(3)}$ is set to zero.

In order to simplify the results and for coherence with literature [26] the constants α_{nm} and β_{nm} are defined for each boundary. Figure 5.2 shows the plot of both constants for different values for the corresponding permeabilities.

$$\alpha_{nm} = \frac{\mu_n - \mu_m}{\mu_n + \mu_m}, \quad (5.29)$$

$$\beta_{nm} = \frac{2\mu_n}{\mu_n + \mu_m}. \quad (5.30)$$

This way the solution for the unknown constants reads:

$$L_0^{(1)} = \frac{\mu_1 - \mu_2}{\mu_1} \ln \left(\frac{a}{R_0} \right) + \frac{\mu_2 - \mu_3}{\mu_1} \ln \left(\frac{b}{R_0} \right), \quad (5.31)$$

$$K_0^{(2)} = -1, \quad L_0^{(2)} = \frac{\mu_2 - \mu_3}{\mu_2} \ln \left(\frac{b}{R_0} \right), \quad (5.32)$$

$$K_0^{(3)} = -1, \quad L_0^{(3)} = 0, \quad (5.33)$$

$$E_n^{(1)} = -\frac{\alpha_{12} \left(\frac{r_I}{a} \right)^{2n} + \alpha_{23} \left(\frac{r_I}{b} \right)^{2n}}{1 + \alpha_{12}\alpha_{23} \left(\frac{a}{b} \right)^{2n}}, \quad (5.34)$$

$$E_n^{(2)} = -\frac{\alpha_{23}\beta_{12} \left(\frac{r_I}{b} \right)^{2n}}{1 + \alpha_{12}\alpha_{23} \left(\frac{a}{b} \right)^{2n}}, \quad F_n^{(2)} = \frac{\beta_{12}}{1 + \alpha_{12}\alpha_{23} \left(\frac{a}{b} \right)^{2n}}, \quad (5.35)$$

$$F_n^{(3)} = \frac{\beta_{12}\beta_{23}}{1 + \alpha_{12}\alpha_{23} \left(\frac{a}{b} \right)^{2n}}. \quad (5.36)$$

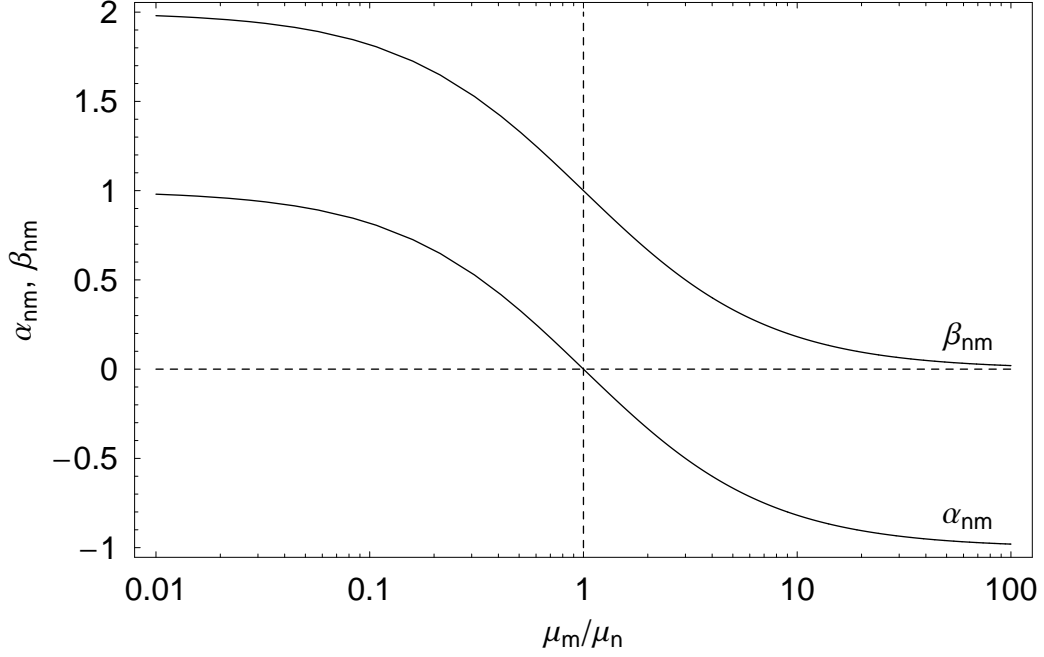


Figure 5.2: Values of the constants α_{nm} and β_{nm} for different permeabilities. The relation, $\beta_{nm} = \alpha_{nm} + 1$, can easily be observed.

5.1.4 Resulting Vector Potential

With the constants derived above the vector potential is given for all three areas to:

$$\begin{aligned}
 A_{1,z}^{\rho < r_I} &= \frac{(\mu_1 - \mu_2)I}{2\pi} \ln\left(\frac{a}{R_0}\right) + \frac{(\mu_2 - \mu_3)I}{2\pi} \ln\left(\frac{b}{R_0}\right) - \frac{\mu_1 I}{2\pi} \ln\left(\frac{r_I}{R_0}\right) \\
 &+ \frac{\mu_1 I}{2\pi} \sum_{n=1}^{\infty} \frac{1}{n} \left(\left(\frac{\rho}{r_I}\right)^n - \frac{\alpha_{12} \left(\frac{\rho}{a^2/r_I}\right)^n + \alpha_{23} \left(\frac{\rho}{b^2/r_I}\right)^n}{1 + \alpha_{12}\alpha_{23} \left(\frac{a}{b}\right)^{2n}} \right) \cos(n\phi), \quad (5.37)
 \end{aligned}$$

$$\begin{aligned}
 A_{1,z}^{\rho > r_I} &= \frac{(\mu_1 - \mu_2)I}{2\pi} \ln\left(\frac{a}{R_0}\right) + \frac{(\mu_2 - \mu_3)I}{2\pi} \ln\left(\frac{b}{R_0}\right) - \frac{\mu_1 I}{2\pi} \ln\left(\frac{\rho}{R_0}\right) \\
 &+ \frac{\mu_1 I}{2\pi} \sum_{n=1}^{\infty} \frac{1}{n} \left(\left(\frac{r_I}{\rho}\right)^n - \frac{\alpha_{12} \left(\frac{\rho}{a^2/r_I}\right)^n + \alpha_{23} \left(\frac{\rho}{b^2/r_I}\right)^n}{1 + \alpha_{12}\alpha_{23} \left(\frac{a}{b}\right)^{2n}} \right) \cos(n\phi), \quad (5.38)
 \end{aligned}$$

$$\begin{aligned}
 A_{2,z} &= \frac{(\mu_2 - \mu_3)I}{2\pi} \ln\left(\frac{b}{R_0}\right) - \frac{\mu_2 I}{2\pi} \ln\left(\frac{\rho}{R_0}\right) \\
 &+ \frac{\mu_2 I}{2\pi} \sum_{n=1}^{\infty} \frac{1}{n} \frac{-\alpha_{23}\beta_{12} \left(\frac{\rho}{b^2/r_I}\right)^n + \beta_{12} \left(\frac{r_I}{\rho}\right)^n}{1 + \alpha_{12}\alpha_{23} \left(\frac{a}{b}\right)^{2n}} \cos(n\phi). \quad (5.39)
 \end{aligned}$$

$$\begin{aligned}
 A_{3,z} &= -\frac{\mu_3 I}{2\pi} \ln \left(\frac{\rho}{R_0} \right) \\
 &+ \frac{\mu_3 I}{2\pi} \sum_{n=1}^{\infty} \frac{1}{n} \frac{\beta_{12} \beta_{23} \left(\frac{r_I}{\rho} \right)^n}{1 + \alpha_{12} \alpha_{23} \left(\frac{a}{b} \right)^{2n}} \cos(n\phi).
 \end{aligned} \tag{5.40}$$

These results can easily be generalized to geometries with a single line current at any position (r_I, ϕ_I) in area 1 by rotating the coordinate system. Mathematically this is given by the substitution

$$\phi \rightarrow \phi - \phi_I.$$

5.2 Permeable Bore

A common way to approximate the effect of a circular iron yoke of superconducting magnets is to replace the yoke by a permeable area with a bore [23]. This approach is valid for iron material with linear behavior, *i.e.*, for fields smaller than the saturation field strength (see section 5.2.3), and for a yoke size thick enough to close most of the field lines inside (see also section 5.3.1).

For the solution of the general problem of three materials, there are three ways to describe the bore inside the permeable area. It can be either assumed that area 1 and 2 or that area 2 and 3 are of the same material properties. Furthermore the geometry is given for an inner radius a equaling the outer radius b and $\mu_2 \neq \infty$. All three approaches yield the same result and so they are an excellent test for the derived terms.

Without any limitations, the permeabilities of the areas 2 and 3 are chosen to be of the same value ($\mu_2 = \mu_3$). The simplified geometry is shown in fig. 5.3. The constants α_{nm}

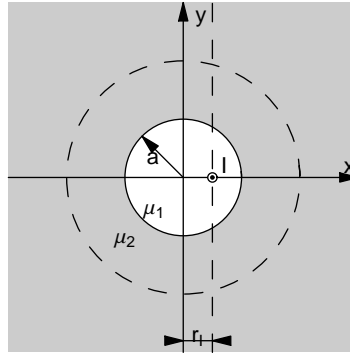


Figure 5.3: Geometry of a single line current in a bore of permeable material.

and β_{nm} then are given by:

$$\alpha_{12} = \frac{\mu_1 - \mu_2}{\mu_2 + \mu_1}, \quad \beta_{12} = \frac{2\mu_1}{\mu_2 + \mu_1}, \tag{5.41}$$

$$\alpha_{23} = 0, \quad \beta_{23} = 1. \tag{5.42}$$

This significantly simplifies the terms for the vector potential. So the denominator containing the two constants α_{12} and α_{23} becomes 1 and the solution for area 2 and 3 are then identical. The resulting vector potentials read

$$A_{\text{Bore},1,z}^{\rho < r_I} = \frac{(\mu_1 - \mu_2)I}{2\pi} \ln\left(\frac{a}{R_0}\right) - \frac{\mu_1 I}{2\pi} \ln\left(\frac{r_I}{R_0}\right) + \frac{\mu_1 I}{2\pi} \sum_{n=1}^{\infty} \frac{1}{n} \left(\left(\frac{\rho}{r_I}\right)^n - \alpha_{12} \left(\frac{\rho}{a^2/r_I}\right)^n \right) \cos(n\phi), \quad (5.43)$$

$$A_{\text{Bore},1,z}^{\rho > r_I} = \frac{(\mu_1 - \mu_2)I}{2\pi} \ln\left(\frac{a}{R_0}\right) - \frac{\mu_1 I}{2\pi} \ln\left(\frac{\rho}{R_0}\right) + \frac{\mu_1 I}{2\pi} \sum_{n=1}^{\infty} \frac{1}{n} \left(\left(\frac{r_I}{\rho}\right)^n - \alpha_{12} \left(\frac{\rho}{a^2/r_I}\right)^n \right) \cos(n\phi), \quad (5.44)$$

$$A_{\text{Bore},2,z} = -\frac{\mu_2 I}{2\pi} \ln\left(\frac{\rho}{R_0}\right) + \beta_{12} \frac{\mu_2 I}{2\pi} \sum_{n=1}^{\infty} \frac{1}{n} \left(\frac{r_I}{\rho}\right)^n \cos(n\phi), \quad (5.45)$$

$$A_{\text{Bore},3,z} = A_{\text{Bore},2,z}. \quad (5.46)$$

5.2.1 Imaging Method for a Single Line Current

Investigating equations (5.43) to (5.46) in terms of the vector potential of a single line current $A_{|,z}(x, y)$ like the primary potential and using the relation $1 = \beta_{nm} - \alpha_{nm}$ yields

$$A_{\text{Bore},1,z}(x, y) = L_0^{(1)} + A_{|,z}(x - r_I, y) - \alpha_{12} A_{|,z}(x - a^2/r_I, y), \quad (5.47)$$

$$A_{\text{Bore},2,3,z}(x, y) = \beta_{12} A_{|,z}(x - r_I, y) + \alpha_{12} A_{|,z}(x, y). \quad (5.48)$$

The expressions for the vector potential include the permeability constant of the corresponding area. This way all terms in the expression for area 1 include μ_1 .

The vector potential within the bore is then given by the primary potential and the potential of a virtual image current at the distance a^2/r_I as given by the imaging method.

The interpretation of the result for the vector potential outside the bore is twofold. On the one hand one could say the term with β is given by the imaging method and the term with α is necessarily added in order to balance the current sum inside the bore to I . On the other hand and for the author's opinion more preferably, the α term can be interpreted as the image current of the closing lead in infinite distance. By means of the imaging method this would be placed in the center.

Following the second argumentation all plain geometries are *a priori* of zero current and charge sum and the parts not considered and placed somewhere very far away have to be taken into account for imaging purposes.

For a continuous vector potential the constant $L_0^{(1)}$ is needed. For the magnetic field and the field of magnetic induction it is of no meaning and therefore does not need to be taken into account for the physical interpretation of the equations above.

In fig. 5.4 a) to c) the field distribution of one single line current is shown for three different outer permeabilities. It can be seen from the plots that the more the outer permeability outranges the inner, the more the field density outside increases compared to inside. Seen from the outer area, this feature results from the fact, that the virtual line current that is placed in the center is weighted with the increasing factor $\mu_2\alpha_{12}$. At the same time the field density inside the bore increases only slightly. Note that this effect occurs only if the current sum inside the bore is different from zero. Otherwise, the centered line currents cancel out.

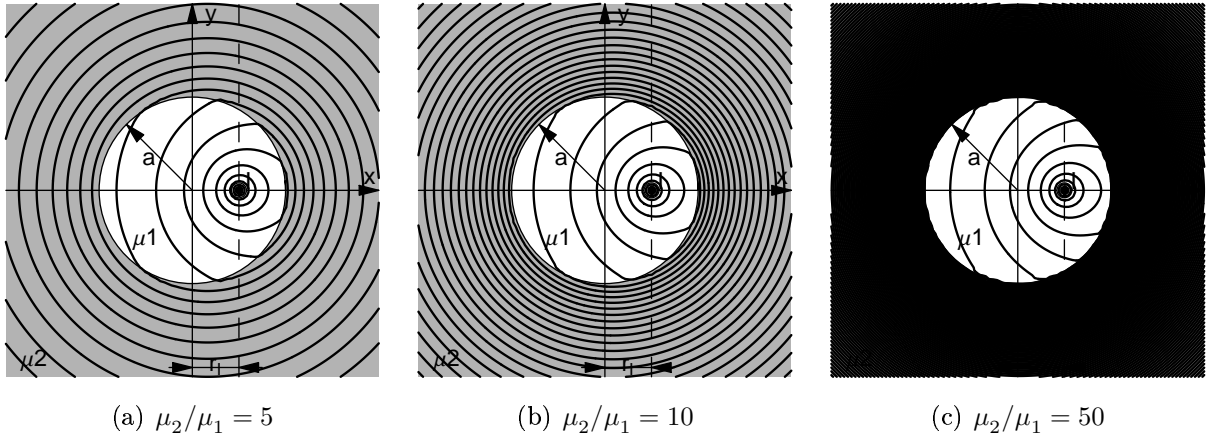


Figure 5.4: Field distribution of the magnetic induction for a line current inside a bore within permeable material. With increasing value of μ_2 the field density in area 2 increases, too.

5.2.2 Material with Infinite Permeability

At a first glance it might seem impossible to put a single line current into a bore within infinitely permeable material because either AMPERE's law or the boundary conditions of orthogonal field lines would be violated.

Following HENKE [26, p. 163], the boundary conditions for a geometry free of current sheets can also be written as

$$\frac{\tan \theta_1}{\tan \theta_2} = \frac{H_{t1}/H_{n1}}{H_{t2}/H_{n2}} = \frac{\mu_1}{\mu_2}. \quad (5.49)$$

Here H_{ti} denotes the tangential and H_{ni} denotes the normal component of the magnetic field on the boundary of area i . The angles θ_i denote the angle between the field/field lines and the normal vector on the boundary. The definition of the angles is also shown in fig. 5.5.

With an outer area of infinite permeability, the quotient of the two tangents is given to zero. This could be either obtained by an inner angle θ_1 of zero which means that the

inner field lines run *perpendicular* to the boundary, or by an outer angle θ_2 of $\pi/2$ which means that field lines outside run *parallel* to the boundary of the bore.

From Eqs. (5.44) and (5.45) the magnetic field can be derived.

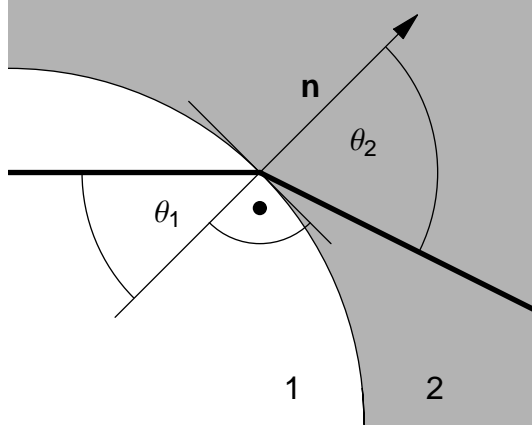


Figure 5.5: Definition of the angles of the field lines by means of a normal vector \mathbf{n} perpendicular to the contour. The two areas 1 and 2 are shown in different colors.

$$H_{1,\rho}^{\rho > r_I} = -\frac{I}{2\pi} \sum_{n=1}^{\infty} \left(\frac{r_I^n}{\rho^{n+1}} - \alpha_{12} \frac{\rho^{n-1}}{(a^2/r_I)^n} \right) \sin(n\phi), \quad (5.50)$$

$$H_{1,\phi}^{\rho > r_I} = \frac{I}{2\pi} \frac{1}{\rho} + \frac{I}{2\pi} \sum_{n=1}^{\infty} \left(\frac{r_I^n}{\rho^{n+1}} + \alpha_{12} \frac{\rho^{n-1}}{(a^2/r_I)^n} \right) \cos(n\phi), \quad (5.51)$$

$$H_{2,\rho}^{\rho > r_I} = -\beta_{12} \frac{I}{2\pi} \sum_{n=1}^{\infty} \frac{r_I^n}{\rho^{n+1}} \sin(n\phi), \quad (5.52)$$

$$H_{2,\phi}^{\rho > r_I} = \frac{I}{2\pi} \frac{1}{\rho} + \beta_{12} \frac{I}{2\pi} \sum_{n=1}^{\infty} \frac{r_I^n}{\rho^{n+1}} \cos(n\phi). \quad (5.53)$$

Calculating the arc tangent of the field components at $\rho = a$ and evaluating the limit for $\mu_2 \rightarrow \infty$ yields the two angles $\theta_{1,2}$:

$$\begin{aligned} \theta_1(\phi) &= \lim_{\mu_2 \rightarrow \infty} \arctan \left(\frac{H_{1,\phi}(\rho = a)}{H_{1,\rho}(\rho = a)} \right) \\ &= \arctan \left(\frac{1}{-2 \sum_{n=1}^{\infty} \left(\frac{r_I}{a} \right)^n \sin(n\phi)} \right) \end{aligned} \quad (5.54)$$

$$\begin{aligned} \theta_2(\phi) &= \lim_{\mu_2 \rightarrow \infty} \arctan \left(\frac{H_{2,\phi}(\rho = a)}{H_{2,\rho}(\rho = a)} \right) \\ &= \lim_{\mu_2 \rightarrow \infty} \arctan \left(\frac{1}{\beta_{12} \rightarrow 0} \right) = \frac{\pi}{2} \end{aligned} \quad (5.55)$$

As shown in Eqs. (5.54) and (5.55), for a single line current in a permeable bore with $\mu \rightarrow \infty$ the latter case is applicable and the field lines are not perpendicular. Fig. 5.6 shows the angle of the field lines at the inner circular boundary of the bore.

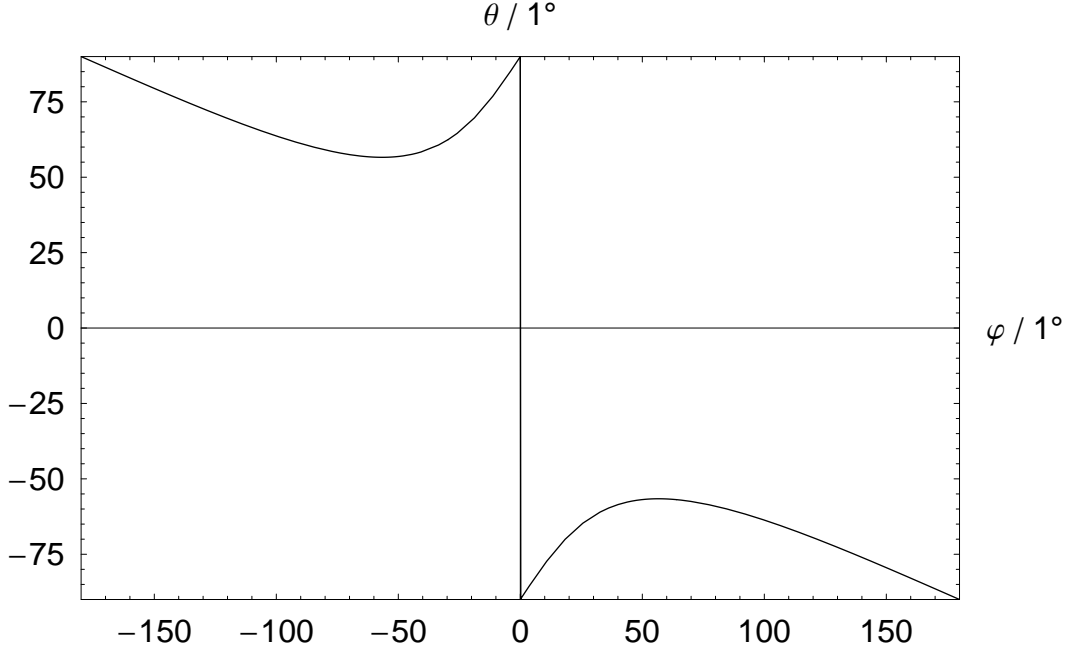


Figure 5.6: Angle of the field lines at the inner boundary of the circular bore in infinitely permeable material.

5.2.3 Saturation Current

For the derivation of the general solution of the three material problem and the imaging method the assumption of linear and homogeneous materials was made. For realistic materials as the magnetic steel of the iron yoke of the NED or LHC dipole this is only valid as long as the magnetic field stays below the value where the yoke material starts to behave non-linearly and saturates. Thus the analytical model is limited by the so-called saturation field strength and the corresponding saturation current.

The saturation current can be obtained by increasing the current of any given geometry until the maximum field inside the material reaches the saturation field. For this purpose, the iron is modeled by means of a bore of radius a in a material of linear and homogeneous permeability μ_{lin} , allowing to derive a closed expression for the saturation current. In order to keep the calculation as general and simple as possible, no specific coil cross section layout is considered, instead two line currents are placed symmetrically at $x = \pm r_P$. The field of the magnetic induction in the permeable material can easily be calculated by means of the imaging method

$$\mathbf{B}_{\text{iron}}(x, y) = \beta_{12} (-\mathbf{B}_|(x + r_P, y) + \mathbf{B}_|(x - r_P, y))$$

where \mathbf{B}_l denotes the field of magnetic induction of a single line current in μ_2 and β_{12} is given by Eq. (5.30).

The field maximum is expected in close vicinity to the coil, located on the boundary. By using the FOURIER expansion of the two line currents, the two maxima of the modulus on the boundary can be identified on the x -axes. Due to the symmetry of the coil the field of magnetic induction on the axis is only y -directed (or $-y$ -directed) and the modulus of the field is given by the modulus of the y -component.

$$\begin{aligned} \max_{\rho=a} |\mathbf{B}_{\text{iron}}| &= |B_{\text{iron},y}(x = \pm a, 0)| \\ &= \beta_{12} \frac{\mu_{\text{lin}} I}{\pi} \frac{r_P}{a^2 - r_P^2} \end{aligned} \quad (5.56)$$

For high values of μ_{lin} the product $\mu_{\text{lin}}\beta_{12}$ can be replaced by μ_0 (for $\mu_{\text{lin}} = 50\mu_0$ the factor gives already $\approx 0.98\mu_0$). Substituting the current I by the ampere turns NI (with N the number of turns and I the current per turn) and setting $B_{\text{sat}} = \max_{\rho=a} |\mathbf{B}_{\text{iron}}|$, the ampere turns per position radius NI/r_P are given to

$$\frac{NI}{r_P} = \pi \frac{B_{\text{sat}}}{\mu_0} r_P \left(\left(\frac{a}{r_P} \right)^2 - 1 \right). \quad (5.57)$$

In a second approach the saturation ampere turns shall be given by means of a set of characteristic curves. This way the saturation current can be read off with respect to the used permeability, the saturation magnetic induction and the two geometric quantities that are the inner yoke and the mean positioning radius of the coil. For this purpose a symmetric geometry of 25 positive and negative line currents is considered. They are angularly evenly distributed along $\pi/3$ at a positioning radius r_M and shape a dipolar coil like for the cosine θ design. The field of this geometry is still expressible by means of analytical formulae, but because of the awkward terms, the evaluation will be done by a computer program and only the final result is shown, omitting the equations.

The maximum of the modulus induction of this geometry is also situated on the x -axis, except if the yoke is too close to the coil, in which case two maxima exist next to the x -axis. In order to avoid this special case, the calculation is carried out for a more realistic ratio of inner yoke radius to positioning radius between 1.1 and 2.5.

As for the simple geometry above, the resulting field is not independent of the radial position of the line currents and the evaluation is done for coil radii r_M from 0.02 m up to 0.15 m. For real coil geometries this would be the mean positioning radius.

The set of characteristic curves is shown in fig. 5.7. The ampere turns for a given geometry are given by the ratio of the saturation field of the material and the value read off from the plot (result in MA).

Since the field of the considered geometry depends linearly on the used ampere turns the current does not need to be taken into account for the drawing of the plot, and the curves are shown for 1 MA of ampere turns. In this way the lines indicate the saturation field per 1 MA of ampere turns.

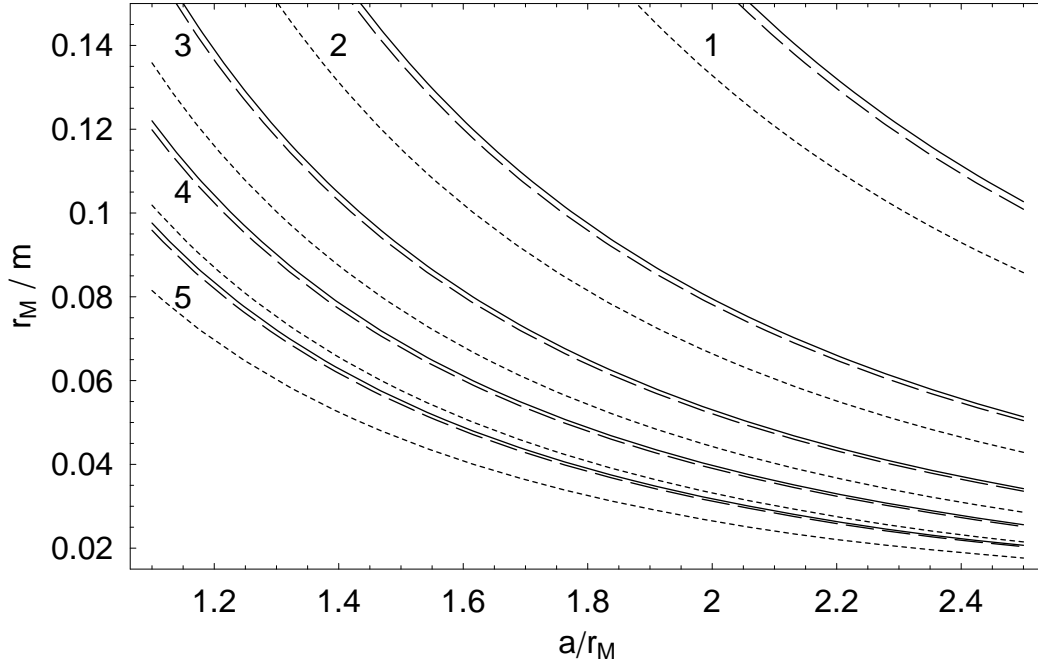


Figure 5.7: Saturation ampere turns for different permeabilities, different mean radii of the coil r_M and different inner yoke radii a . The calculation was carried out for an excitation current of 1 MA. The continuous lines represent a relative permeability of 500, the dashed lines of 50, and the dotted lines of 5. Higher permeabilities do not show any difference to the values for 500. Always three lines of different permeabilities form a group representing the saturation field strength B_{sat} with the value indicated in T/MA.

For an exemplary calculation a coil of 90 conductors and a mean positioning radius of 0.075 m is considered. The relative permeability of the iron yoke is chosen to be 500, the saturation field set to 2 T, and the inner yoke radius to 0.125 m. For this geometry, the closed expression yields a current of 7.4 kA. From the set of characteristic curves a value of 3 T/MA can be read off which is equivalent to a conductor current of 7.4 kA and shows the good agreement of the two approaches for high permeabilities.

5.2.4 Effect on Multipole Errors

In section 3.2 it was shown that the multipole errors of a single line current can be derived by comparing the expression for the radial field with the general multipole expansion. Furthermore it was shown that a geometry of an up-down symmetry only gives normal multipole errors which are at maximum for zero positioning angle of the line current.

In order to reduce the degrees of freedom for this estimation a single line current at an arbitrary position on the x -axis is assumed and only the position with respect to the bore radius and the permeability are varied. For a more general result considering the

positioning angle as well, the same approach could be used by applying the sine addition theorems (see also 5.1.4).

Deriving the normal magnetic induction from Eq. (5.43), the normal multipole errors are given to

$$B_{n,\text{Bore}} = -\frac{\mu_1 I}{2\pi} \frac{r_0^{n-1}}{r_I^n} \left(1 - \alpha_{12} \left(\frac{r_I}{a} \right)^{2n} \right). \quad (5.58)$$

where r_0 denotes the reference radius. This result can easily be split into the multipole error induced by the line current $B_{n,|}$ and the added $\Delta B_{n,\text{Bore}}$ of the virtual image current. Then the added relative normal multipole error reads

$$\frac{B_{n,\text{Bore}} - B_{n,|}}{B_{n,|}} = \frac{\Delta B_{n,\text{Bore}}}{B_{n,|}} = -\alpha_{12} \left(\frac{r_I}{a} \right)^{2n}. \quad (5.59)$$

Figure 5.8 shows the dependence of the added multipole error on the inner bore radius for a material with infinite permeability.

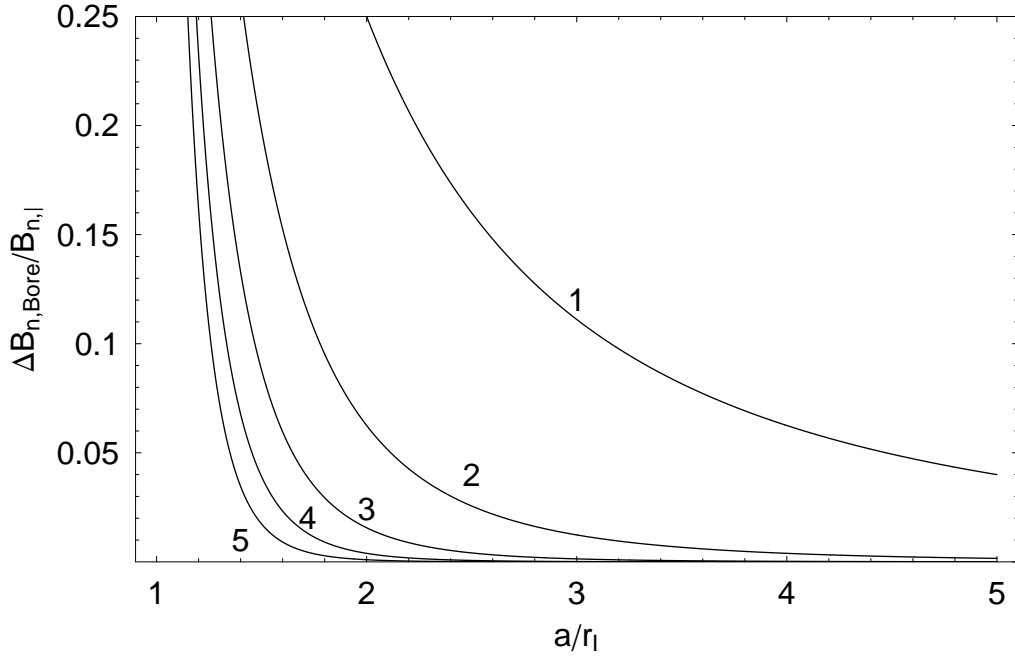


Figure 5.8: For a line current inside a circular bore within a material with infinite permeability, multipole errors are induced by the line current and its virtual image current. The dependence of the the additional multipole errors on the inner bore radius with respect to the positioning radius of the considered strand is shown.

Table 5.1 shows the effect on the multipole errors if a coil geometry is put into a bore within material with an infinite permeability and a mean positioning radius of half the

bore radius. The numbers illustrate that even under perfect conditions the influence of the permeable material reduces fast with increasing multipole order and that the contribution of the permeable yoke to the main field is only of approximately 25% at most. For a realistic yoke which in addition shows saturation effects, this contribution is even smaller.

Table 5.1: Added multipole error for a bore within material with infinite permeability and an assumed mean positioning radius of half the bore radius.

n	1	2	3	4	5
$\Delta B_{n,\text{Bore}}/B_{n, }$	0.250	0.063	0.016	0.004	0.001

From tab. 5.1 it is also possible to estimate the influence of the iron yoke on the relative multipole errors b_n . The relative multipole errors are normalized to B_1 and so they decrease for increasing B_1 . Of all multipoles the main field B_1 is affected most and therefore the contribution of the iron yoke reduces the modulus of the relative multipole errors.

5.3 Permeable Pipe

The iron yoke of real superconducting magnets is more or less a pipe of a high permeable material. This is usually modeled by means of the imaging method or calculated with the finite element method. In order to determine the applicability of the imaging method and to give an analytical expression, the solution shall be derived directly from the general solution for circular geometries (section 5.1.4).

For this purpose, the general geometry is simplified by setting the permeabilities of area 1 and 3 identical ($\mu_1 = \mu_3$) and the permeability of area 2 to a higher value ($\mu_2 > \mu_1$). All other quantities remain unchanged. The geometry of the single line current inside the permeable pipe is shown in fig. 5.9.

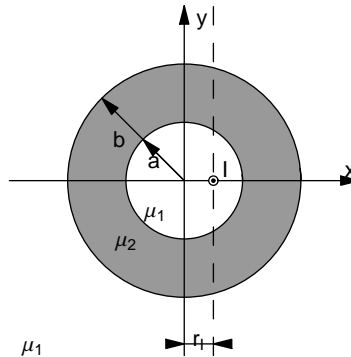


Figure 5.9: Geometry of a single line current inside a permeable pipe.

5.3. Permeable Pipe

With the assumptions given above, the constants α_{nm} and β_{nm} read:

$$\alpha_{12} = \frac{\mu_1 - \mu_2}{\mu_2 + \mu_1}, \quad \beta_{12} = 1 + \alpha_{12}, \quad (5.60)$$

$$\alpha_{23} = -\alpha_{12}, \quad \beta_{23} = 1 - \alpha_{12}, \quad (5.61)$$

and the vector potentials result to:

$$\begin{aligned} A_{1,z}^{\rho < r_I} &= \frac{(\mu_1 - \mu_2)I}{2\pi} \ln\left(\frac{a}{b}\right) - \frac{\mu_1 I}{2\pi} \ln\left(\frac{r_I}{R_0}\right) \\ &+ \frac{\mu_1 I}{2\pi} \sum_{n=1}^{\infty} \frac{1}{n} \left(\left(\frac{\rho}{r_I}\right)^n - \alpha_{12} \frac{\left(\frac{\rho}{a^2/r_I}\right)^n - \left(\frac{\rho}{b^2/r_I}\right)^n}{1 - \alpha_{12}^2 \left(\frac{a}{b}\right)^{2n}} \right) \cos(n\phi), \end{aligned} \quad (5.62)$$

$$\begin{aligned} A_{1,z}^{\rho > r_I} &= \frac{(\mu_1 - \mu_2)I}{2\pi} \ln\left(\frac{a}{b}\right) - \frac{\mu_1 I}{2\pi} \ln\left(\frac{\rho}{R_0}\right) \\ &+ \frac{\mu_1 I}{2\pi} \sum_{n=1}^{\infty} \frac{1}{n} \left(\left(\frac{r_I}{\rho}\right)^n - \alpha_{12} \frac{\left(\frac{\rho}{a^2/r_I}\right)^n - \left(\frac{\rho}{b^2/r_I}\right)^n}{1 - \alpha_{12}^2 \left(\frac{a}{b}\right)^{2n}} \right) \cos(n\phi), \end{aligned} \quad (5.63)$$

$$\begin{aligned} A_{2,z} &= \frac{(\mu_2 - \mu_3)I}{2\pi} \ln\left(\frac{b}{R_0}\right) - \frac{\mu_2 I}{2\pi} \ln\left(\frac{\rho}{R_0}\right) \\ &+ \frac{\mu_2 I}{2\pi} \sum_{n=1}^{\infty} \frac{1}{n} \beta_{12} \frac{\alpha_{12} \left(\frac{\rho}{b^2/r_I}\right)^n + \left(\frac{r_I}{\rho}\right)^n}{1 - \alpha_{12}^2 \left(\frac{a}{b}\right)^{2n}} \cos(n\phi). \end{aligned} \quad (5.64)$$

$$A_{3,z} = -\frac{\mu_1 I}{2\pi} \ln\left(\frac{\rho}{R_0}\right) + \frac{\mu_1 I}{2\pi} \sum_{n=1}^{\infty} \frac{1}{n} \frac{\beta_{12}(1 - \alpha_{12}) \left(\frac{r_I}{\rho}\right)^n}{1 - \alpha_{12}^2 \left(\frac{a}{b}\right)^{2n}} \cos(n\phi). \quad (5.65)$$

As could be expected, the influence of the permeable pipe vanishes for $a = b$ with $\mu_2 \neq \infty$ and also for $\mu_2 = \mu_1$. For $b \rightarrow \infty$ the Eqs. (5.62) to (5.65) transform to the expressions for the bore in permeable area given in Eqs. (5.44) and (5.46). Furthermore the expressions are in good agreement with the results published in literature as [27].

In fig. 5.10 the distribution of the magnetic induction is shown for three pipes of different permeabilities. It can be seen that for increasing permeability of the pipe more and more magnetic flux is concentrated in the pipe walls like for the permeable core of toroidal coils. Mathematically this is related to the same fact as explained for the permeable bore and it also vanishes if the current sum inside the pipe is set to zero.

Considering Eq. (5.65) for a pipe made of infinitely permeable material, it can be seen that the field of the line current outside the pipe is not screened, but the virtual position of the line current is moved towards the pipe center. This observation is in agreement with $\oint \mathbf{H} \cdot d\mathbf{s} = I$.

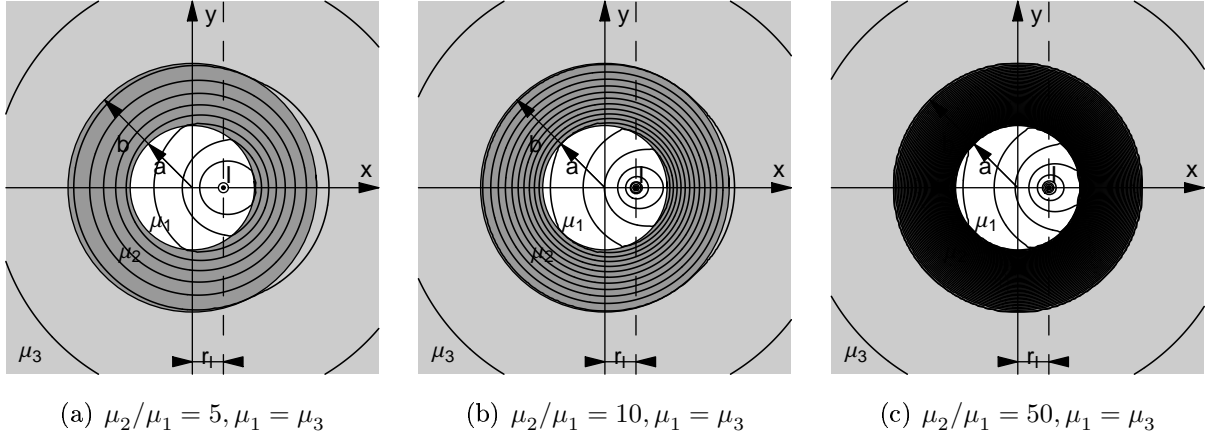


Figure 5.10: Field distribution of the magnetic induction for a line current inside a pipe of permeable material.

5.3.1 Effect on Multipole Errors

For the effect on the multipole errors, the radial field is needed and can be derived from the vector potential obtained from Eq. (5.62). Then the normal multipole errors are given by

$$B_{n,\text{Pipe}} = -\frac{\mu_1 I r_0^{n-1}}{2\pi r_I^n} \left(1 - \alpha_{12} \frac{\left(\frac{r_I}{a}\right)^{2n} - \left(\frac{r_I}{b}\right)^{2n}}{1 - \alpha_{12}^2 \left(\frac{a}{b}\right)^{2n}} \right). \quad (5.66)$$

The difference to the multipole error calculated by means of the imaging method is given by:

$$\Delta B_{n,\text{Pipe}} = B_{n,\text{Pipe}} - B_{n,\text{Bore}} \quad (5.67)$$

$$= \alpha_{12} \frac{1 - \alpha_{12}^2}{1 - \alpha_{12}^2 \left(\frac{a}{b}\right)^{2n}} \left(\frac{r_I}{b}\right)^{2n}. \quad (5.68)$$

For materials of high permeability the influence of the pipe thickness is very small since in this case α_{12} is close to -1 and for $a < b$ the fraction is smaller than 1. In this way the deviation is mainly driven by the fraction $(r_I/b)^n$ with $b \geq a > r_I$.

In fig. 5.11 the relative deviation $(\Delta B_{n,\text{Pipe}}/B_{n,\text{Bore}})$ of the multipole errors for a pipe with finite thickness compared to the multipole errors of a bore is shown. The positioning radius r_I is set to half the inner pipe radius. The dashed lines indicate a relative deviation of -0.1% and the continuous lines of -1% . It can be seen that for yokes of an outer radius of more than three times the inner radius the modulus of the deviation is smaller than 1% for all multipoles. Furthermore it can be seen that for high permeabilities and therefore values of α close to -1 the absolute deviation is much smaller even if the outer radii are only 1.5 times the inner radius. Generally the influence of the pipe thickness is strongly

depending on the order of the multipole error and for thick pipes it is only significant up to the order of 3.

In order to show how to use fig. 5.11 one example is given: Considering a yoke of outer radius 2.5 times the inner radius and an α of -0.8 this yields a deviation of little more than -1% for the main field (B_1) because it is inside and close to the continuous line indicated by 1 and an absolute deviation of less than 0.1% for all other multipoles since the point is outside all higher order dashed lines.

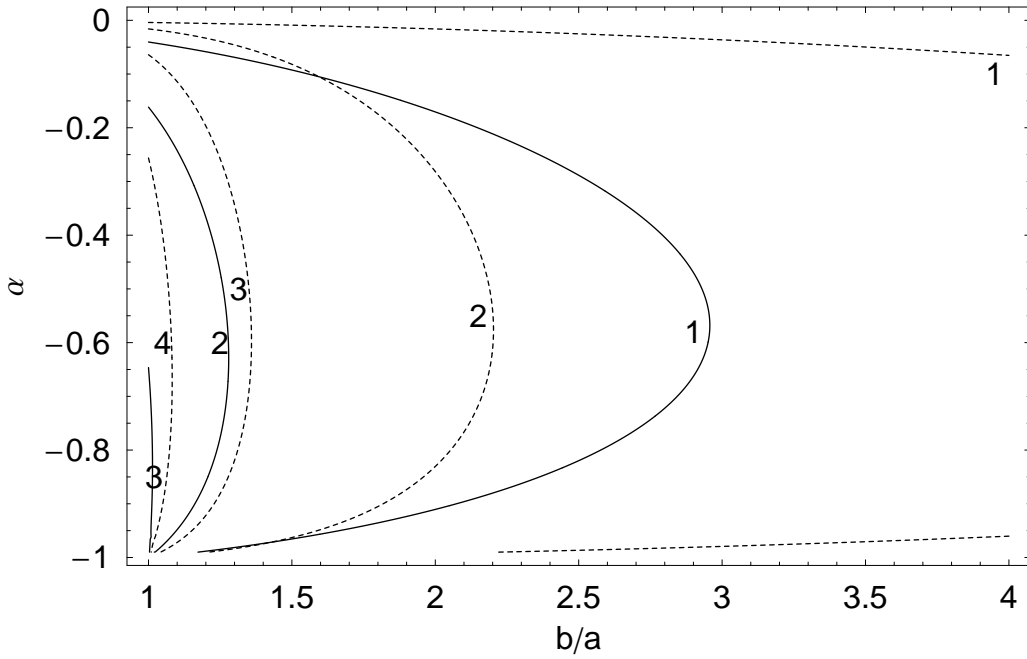


Figure 5.11: The relative deviation of the multipole errors for a pipe of varying thickness and permeability compared to a bore of fixed inner radius. The positioning radius r_I is assumed to be half the inner pipe radius a . The parameter α denotes the imaging coefficient as defined in Eq. (5.29). The continuous lines indicate a deviation of -1% compared to the calculation with the imaging method. The dashed lines indicate a deviation of -0.1% . The numbers denote the order of the multipole error.

Multipole errors decrease with increasing order and as a consequence of the negative contribution of the pipe terms the modulus of the relative multipole errors b_n increases if the yoke thickness has to be considered.

5.3.2 Stray Field of a Coil

For the operation of superconducting magnets it is important to make sure that the field outside the magnet, the so-called stray field, does not exceed certain limits. This stray

field could cause problems with other electrical devices, cause movements of iron parts or even effect the health of persons exposed to it [28].

It is obvious that the strength of the stray field increases with increasing main field and therefore it is most severe for a magnet operated at maximum field. As mentioned above, for high fields the iron saturation has to be taken into account and a calculation has to be done by means of numerical field computation.

Nevertheless, an analytical expression shall be derived from the expressions obtained before to be used for first estimations and investigations. Therefore a coil of two leads is considered in order to represent the bipolar character of symmetric coils.

From Eq. (5.65) the outer vector potential and the field of magnetic induction of a coil can be obtained.

$$A_{3,z} = \frac{\mu_1 I}{2\pi} \sum_{n=1}^{\infty} \frac{1}{n} \frac{\beta_{12}(1 - \alpha_{12})}{1 - \alpha_{12}^2 \left(\frac{a}{b}\right)^{2n}} \left(\frac{r_I}{\rho}\right)^n \cos(n\phi) [1 - \cos(n\pi)] \quad (5.69)$$

$$B_{3,\rho} = -\frac{\mu_1 I}{2\pi} \sum_{n=1}^{\infty} \frac{\beta_{12}(1 - \alpha_{12})}{1 - \alpha_{12}^2 \left(\frac{a}{b}\right)^{2n}} \frac{r_I^n}{\rho^{n+1}} [1 - \cos(n\pi)] \sin(n\phi) \quad (5.70)$$

$$B_{3,\phi} = \frac{\mu_1 I}{2\pi} \sum_{n=1}^{\infty} \frac{\beta_{12}(1 - \alpha_{12})}{1 - \alpha_{12}^2 \left(\frac{a}{b}\right)^{2n}} \frac{r_I^n}{\rho^{n+1}} [1 - \cos(n\pi)] \cos(n\phi) \quad (5.71)$$

Figure 5.12 shows the field distribution of a symmetric coil of two leads in an iron pipe with a relative permeability of 10. The stray field is easily observeable.

As shown in appendix A.1 the modulus of a vector field in cylindrical coordinates is given by the square root of the sum of the components squared. The squaring of the sum terms is done by mutually multiplying all members. With the coefficients k_{nm} given by

$$k_{nm}(\rho) = \beta_{12}^2 (1 - \alpha_{12})^2 \frac{(1 - \cos(n\pi))(1 - \cos(m\pi))}{\left(1 - \alpha_{12}^2 \left(\frac{a}{b}\right)^{2n}\right) \left(1 - \alpha_{12}^2 \left(\frac{a}{b}\right)^{2m}\right)} \frac{r_I^{2n}}{\rho^{n+m+2}} \quad (5.72)$$

which is only different from zero for odd m and n , the modulus reads

$$|\mathbf{B}| = \frac{\mu_1 |I|}{2\pi} \sqrt{\sum_{n=1}^{\infty} \sum_{m=1}^{\infty} k_{nm} \cos((n-m)\phi)}. \quad (5.73)$$

In fig. 5.13 the maximum of the modulus of the stray field is displayed for different outer yoke radii and permeabilities. The inner yoke radius is of 125 mm which is similar to the radius used for the NED 88 mm aperture dipole. The line currents of ± 1 A are placed at $r_I = a/2$. Assuming a linear material the results can be scaled to any currents (or ampere turns).

It has to be emphasized that due to saturation effects at high fields the stray field of real geometries will exceed the values given above.

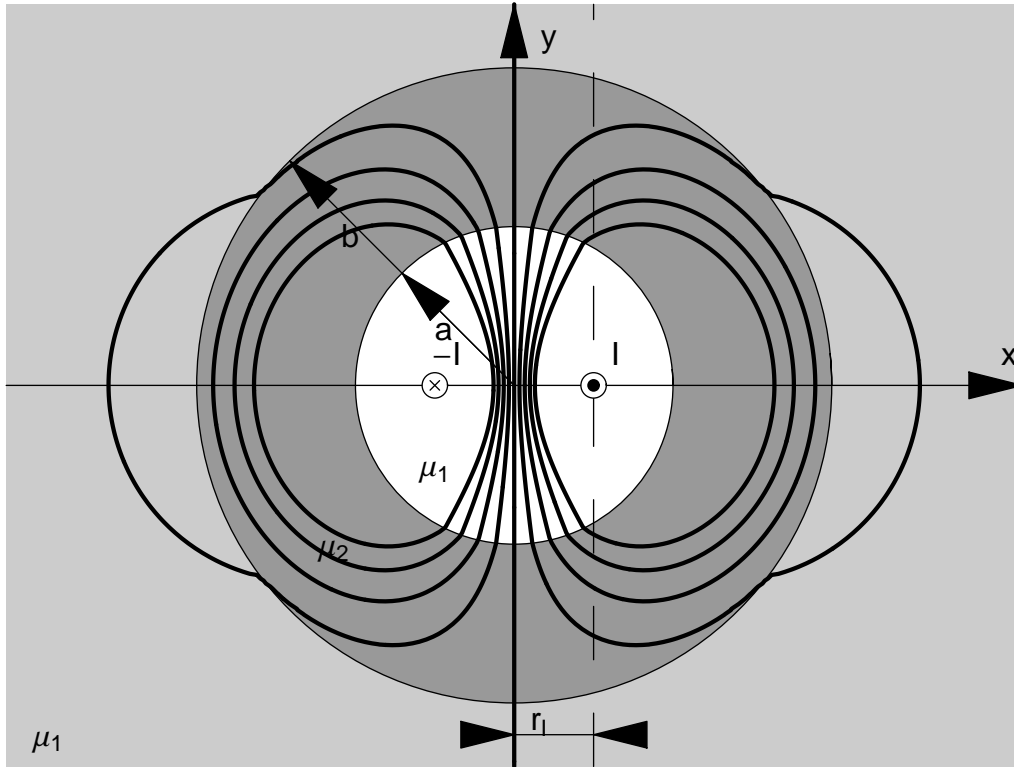


Figure 5.12: Field distribution of the magnetic induction for a coil in a permeable pipe. The positioning radius is half the inner yoke radius. The outer yoke radius is twice the inner yoke radius and the permeability of the pipe is 10 times bigger than the permeability of the air domain.

In [29, p. 228] JACKSON calculates the screening of the magnetic field of a line current due to a surrounding permeable cylinder by using the scalar potential approximation of a line dipole of first order, and gives the screening factor F to

$$F = \frac{4\mu_r b^2}{(\mu_r + 1)^2 b^2 - (\mu_r - 1)^2 a^2}.$$

This equals the first coefficient ($n = 1$) of the vector potential given in Eq. (5.69) and confirms the results.

5.4 Influence of the Steel Collar

Superconducting coils are usually surrounded by rigid force-retaining structures in order to withstand the enormous LORENTZ forces and to provide prestress to the coil. The force-retaining structure usually consists of a combination of a collar made of stainless steel or aluminum and a surrounding iron yoke made of magnetic steel. This method increases the

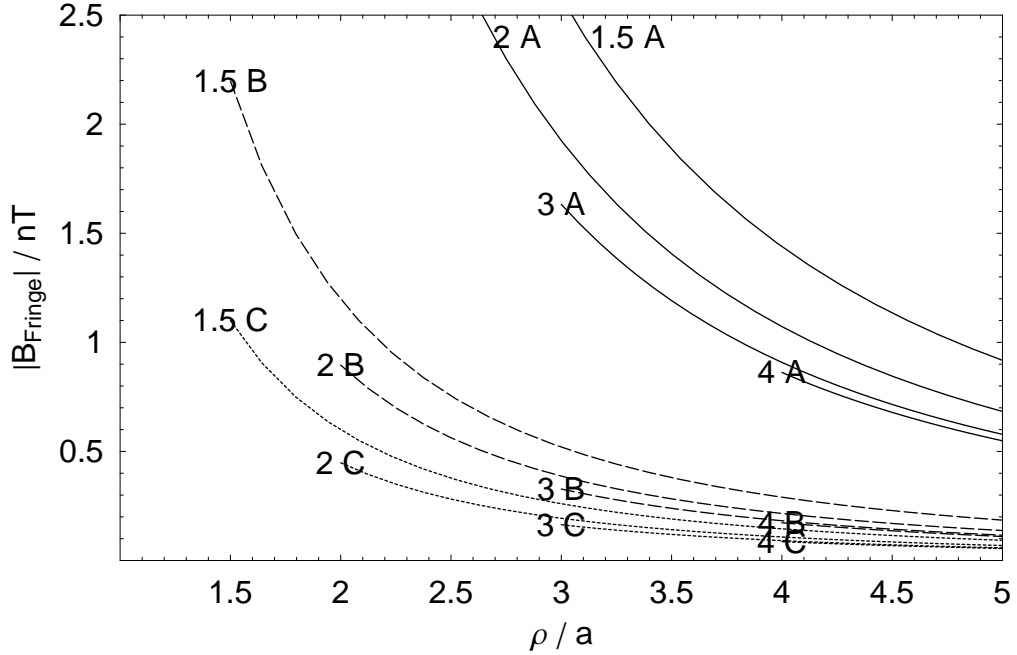


Figure 5.13: Modulus of the stray field along the x -axis for different outer pipe radii and pipe permeabilities. The numbers indicate the outer pipe radii in fractions of the inner pipe radius. The capital letters indicate the used relative permeability of the pipe material ($A = 500$, $B = 2500$ and $C = 5000$). The inner pipe radius a is 125 mm, the current I is 1 A and the position of the currents r_I is $a/2$.

minimum distance between the iron yoke and the coil and the collar represents a second material to be modeled independently.

A rough estimation of the influence of the collar on the multipole errors is given by modeling a circular collar (neglecting, *e.g.*, the nose in the center of the two coils) by means of the general solution of the three material problem derived above. From Eq. (5.37), the radial magnetic field and the normal multipole errors can be calculated.

$$B_{n,\text{Collar}} = -\frac{\mu_1 I r_0^{n-1}}{2\pi r_I^n} \left(1 - \frac{\alpha_{12} \left(\frac{r_I}{a}\right)^{2n} + \alpha_{23} \left(\frac{r_I}{b}\right)^{2n}}{1 + \alpha_{12}\alpha_{23} \left(\frac{a}{b}\right)^{2n}} \right) \quad (5.74)$$

Figure 5.14 shows the relative deviation of the multipole errors if calculated with and without collars made of material with low permeability. The mean positioning radius r_I of the coil is set to 0.075 m and the inner collar radius a is set to 0.1 m. The inner yoke radius b is given by the varied collar thickness d to $b = a + d$. The relative permeability of the iron yoke is set to 500 while the permeability of the collar is also varied. It can be seen that the influence of the collar material on the multipole errors decreases strongly with increasing multipole order. For materials with a relative permeability below 2 the contribution of the collar is completely negligible.

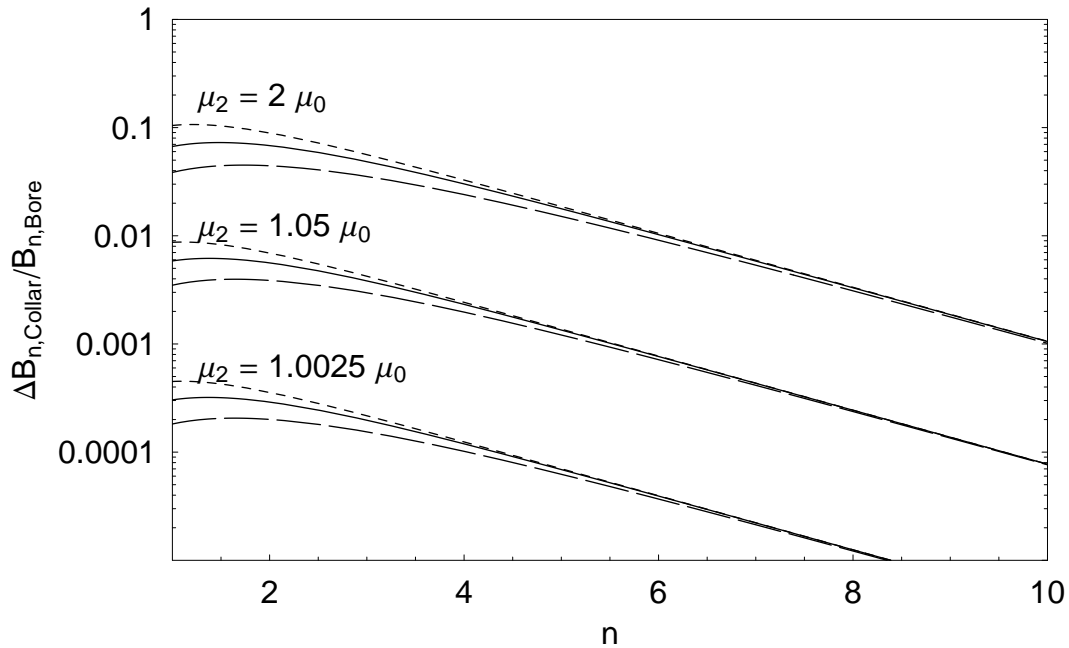


Figure 5.14: Influence of the collar on the multipole errors. The continuous lines represent a geometry of inner collar radius a of 0.1 m and collar thickness d of 0.025 m. For the dotted lines the collar thickness is increased to $d = 0.05$ m while for the dashed lines the collar thickness is decreased to $d = 0.0125$ m.

5.5 Conclusions

For a very general geometry like an excentric line current placed in a circular domain and surrounded by two materials of different permeabilities, a general solution for the magnetic field is found. This was used to derive the solution for a single line current

- inside a bore in permeable material,
- inside a pipe of permeable material, and
- inside a pipe of low permeability surrounded by a higher permeability.

The solution can be used to decide whether the iron yoke in magnet applications can be modeled analytically and whether a steel collar has to be considered in the calculation. In this way the so-called imaging method for a single line current in a circular bore was derived and it could be shown that

- it is possible to fulfill the boundary conditions for a single line current in a bore within material with infinite permeability without violating AMPERE's law, and
- that the closing lead, usually not considered for the calculation of a single line current, becomes important when the imaging method is applied.

Using the imaging method,

- the influence of the iron yoke on the multipole errors could be modeled, and
- the limitations of the model due to the iron saturation could be estimated.

For the latter two geometries it is shown,

- that for the radii and permeabilities commonly used for the iron yoke of superconducting magnets, the imaging method is sufficient to calculate the effect of the iron yoke on the multipole errors in the non saturated state,
- how to estimate the stray field and how it decreases with increasing distance to the yoke, and
- that for the commonly used low permeabilities of the collar material the collar does not need to be considered within the analytical calculations.

The validity of the imaging method for the modeling of superconducting magnets has been shown and the limiting factors as the yoke thickness and the maximum allowed current, the saturation current, were pointed out.

6 Optimization of the Coil Cross Section

The field quality in superconducting magnets is dominated by the position of the superconducting cables and only little influenced by the shape of the iron yoke. Thus the first priority to achieve a good field quality is to optimize the coil cross section layout. Consequently, after defining the number of conductors in order to obtain a certain main field by means of a preliminary design or by means of an analytical estimation as shown in section 4.4, the conductor positioning is optimized for operation point values.

All modifications of the magnet, *e.g.*, a change of the shape of the iron yoke, a change of the working point which means to operate with a different iron saturation or the insertion of ferromagnetic elements, cause changes in the multipole errors. This makes an iteration of the optimization process of the coil cross section necessary.

6.1 Optimization Process

The optimization of the coil cross section of a superconducting high-field magnet is subdivided into four main steps which are repeated until the wanted result could be obtained: Determination of the excitation current, setting of the parameter ranges and weights of the objectives in order to achieve the optimization goals, numerical optimization and control of the geometrical, magnetical and mechanical constraints.

6.1.1 Excitation Current

Since the optimization is carried out at the operation point at high field, the surrounding iron yoke partly saturates and the non-linearity of the permeability has to be taken into account. The iron saturation depends on the conductor layout and the excitation current and thus all modifications result in a change of magnetic field and field quality. For this reason, before and after every optimization run the margin on the load line has to be checked and adapted by means of the excitation current.

6.1.2 Optimization Goals

The main optimization goals for the coil cross section are to obtain a high main field, low relative multipole errors and radially aligned blocks. The limits for the field and the field

quality depend on the application. In the optimization presented in this thesis, it is tried to reduce all relative multipole errors as much as possible.

The aimed radial alignment results from mechanical reasons: As described in section 1.3, the coil shapes around the aperture and the beam pipe. At the coil ends, the windings have to bent up and mechanical strain is applied to the superconducting cable. Due to the strain sensitivity of superconductivity, this increases the probability for a quench of the superconductor in the region considered. For radial aligned blocks, the strain in the coil head winding is smaller compared to non-radial, flat coils.

Considering the coil cross section, non-radial blocks are sheared due to the winding process with the winding mandrel and thus create a saw tooth pattern at the inner and the outer radius. In combination with the LORENTZ forces and the prestress, this can cause very high local stresses. In addition the shear creates free space at the outer radius which could allow conductor movements.

6.1.3 Numerical Optimization

The field calculation and the optimization of the coil cross section is carried out using the field computation program **ROXIE**. For the simulation, the coil winding process is reproduced by means of a virtual winding mandrel and the coil cross section can be described by the inner radii of the layers and the positioning and inclination angles of the blocks. Based on this, the conductor positioning algorithm calculates the position of each conductor. This way the number of degrees of freedom is reduced to three per block: The number of turns respectively conductors and the two angles.

Since it is not possible to have intersecting conductors and since the available space close to the aperture is limited, these quantities are not fully independent, *e.g.*, using a block with a big number of conductors limits the number of conductors of the other blocks of the same layer.

For the optimization of the coil cross section the optimization algorithm **EXTREME** is used. Based on a given parameter range including a starting point and the definition of weighted objectives it performs an elaborated search for a minimum [23]. By modifying the limits and weights, the results can be fine-tuned.

6.1.4 Limit Control

After the coil cross section was modified, the results have to be checked for their conformity with the specifications. This includes a geometrical check of the size of the wedges and the opening radius of the coil for the collar nose, the check of the maximum stress and of the margin on the load line. In an additional calculation it is checked whether the modified design is still able to reach a peak field of 15 T at 0% margin on the load line.

6.1.5 Additional Properties

For the comparison of different designs, further quantities are calculated which are not directly subject to the optimization.

Due to the critical current density of superconducting magnets, the operation is limited to certain maximum fields. The peak field on any conductor determines the maximum current and thus the performance of the magnet. By means of the peak field to main field ratio the efficiency of the conductor distribution can be depicted.

By calculating the stored energy, a first impression of the challenges of the quench protection can be received. In the first moment of a quench the stored energy starts to discharge in the very small, normal conducting part of the magnet and can cause severe damage. From the energy and the used currents the inductance can be obtained.

6.2 Preliminary Design

At the beginning of the NED program, a preliminary magnet design was carried out by LEROY and VINCENT-VIRY in order to determine meaningful cable and strand parameters [4]. This resulted in the NED cable specified above and the coil cross section shown in fig. 6.1. The conductor positions were not optimized neither according to the radial constraints nor to field quality.

Since the preliminary design was carried out, the specifications of the NED magnet (shown in chapter 2) have been modified, *e.g.*, the thickness of the midplane insulation and the inner radius of the iron yoke were increased. Moreover the thermal contraction factor for the coil material was increased. These modifications result in a change of the presented electromagnetic properties and emphasize the necessity of a re-optimization.

Salient electromagnetic properties and the field quality expressed by means of the relative multipole errors of the preliminary design are shown in tabs. 6.1 and 6.2. The corrected inner yoke radius and the contraction factor are taken into account but not the greater thickness of the midplane insulation.

The preliminary magnet design is able to reach a peak field of more than 15 T but shows very big relative multipole errors. The radial alignment of the blocks is not sufficient and could cause problems for the head windings.

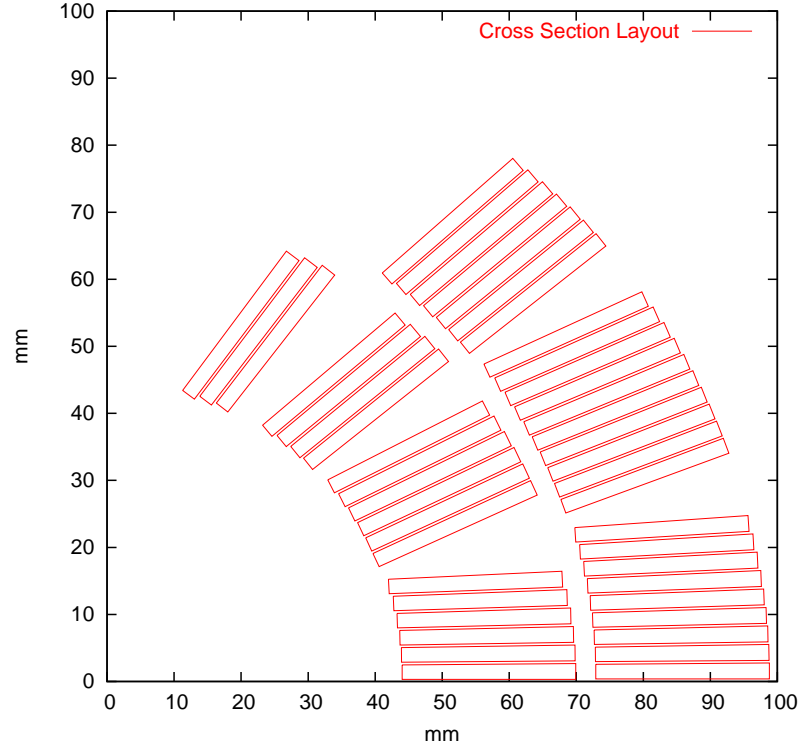


Figure 6.1: Coil cross section layout of the preliminary design.

Table 6.1: Salient electromagnetic properties of the preliminary design at a margin on the load line of 10.0%.

Quantity	Value	Unit
Excitation current	25395	A
Main field B_1	-13.03	T
Peak field on conductor B_{peak}	13.61	T
Peak field / main field	1.045	-
Stored magnetic energy per unit length	1.454	MJ/m
Inductance per unit length	4.510	mH/m
Horizontal force F_x per side and per unit length	13.00	MN/m
Stress on the midplane (inner layer)	-114.5	MPa
Stress on the midplane (outer layer)	-118.8	MPa
Excitation current at 0% margin on the load line	28560	A
Peak field at 0% margin on the load line	15.09	T

Table 6.2: Relative multipole errors b_n in units for the preliminary design in a circular iron yoke at a margin on the load line of 10.0%.

b_3	b_5	b_7	b_9	b_{11}	b_{13}	b_{15}
-30.970	-2.371	6.856	1.924	1.532	-0.163	0.160

6.3 Resulting Coil Cross Section A

Starting with the preliminary design the coil cross section was optimized mainly subject to the reduction of the relative multipole errors. Within this process the number of conductors in the upper blocks (block 3, 6 and 7) was reduced and one conductor was moved from the inner to the outer layer. The total number of conductors did not changed. This way, more space could be obtained in the inner layer and the radial alignment of the blocks could be improved by means of the radial constraint described in appendix C.2.

Tables 6.3 and 6.4 show salient electromagnetic parameters and the relative multipole errors at a margin on the load line of 10.56%. A further decrease of the margin could not be obtained.

Compared to the preliminary design the so-called coil cross section A (CCS A) shows much smaller multipole errors except for b_{11} which is still around 1 to 2 units. The radial alignment of the blocks could be improved. The peak field at 0% margin on the load line is smaller than that of the preliminary design but still above 15 T. This decrease can be explained by the new distribution of the conductors which shows less conductors in the most efficient region close to the midplane (also shown in the multipole sensitivity plot fig. 3.5 a)) and for which one conductor was moved from the inner to the outer layer.

The main field to peak field ratio could be decreased resulting in a higher main field although the margin on the load line is bigger than for the preliminary design.

The increase of the stored magnetic energy and the inductance is related to the higher excitation current.

The CCS A is considered feasible and is used for the study of the iron yoke saturation, although it shows some issues which have to be revised: The inclination of the block 5 is rather small and should be increased. The distance between block 2 and 3 is very big causing a lower efficiency and a big copper wedge.

6.3. Resulting Coil Cross Section A

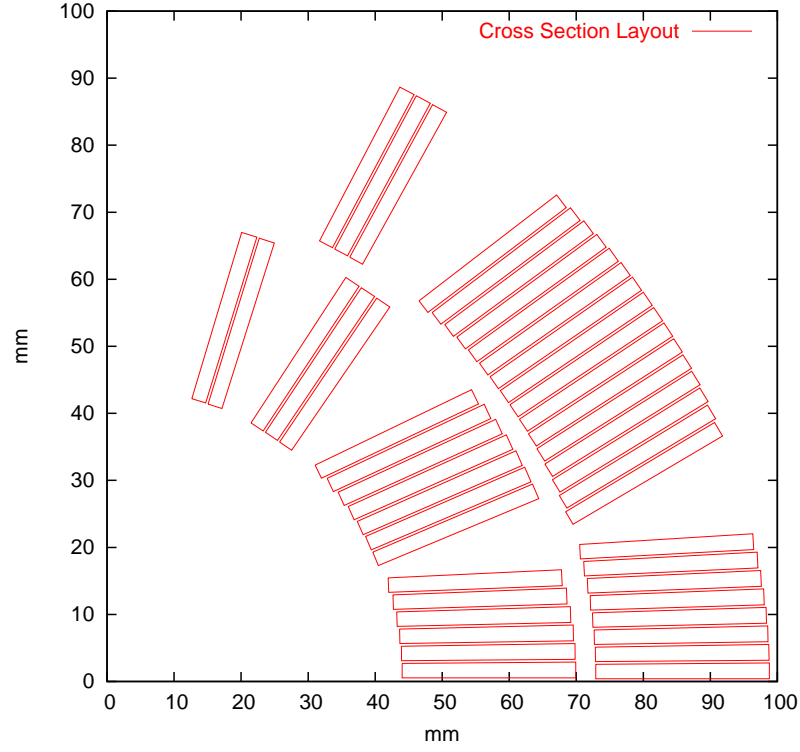


Figure 6.2: Coil cross section layout A.

Table 6.3: Salient electromagnetic properties for the coil cross section A at a margin on the load line of 10.56%.

Quantity	Value	Unit
Excitation current	25939	A
Main field B_1	-13.05	T
Peak field on conductor B_{peak}	13.46	T
Peak field / main field	1.031	-
Stored magnetic energy per unit length	1.471	MJ/m
Inductance per unit length	4.373	mH/m
Horizontal force F_x per side and per unit length	13.37	MN/m
Stress on the midplane (inner layer)	-109.9	MPa
Stress on the midplane (outer layer)	-125.2	MPa
Excitation current at 0% margin on the load line	29375	A
Peak field at 0% margin on the load line	15.01	T

Table 6.4: Relative multipole errors b_n in units for the coil cross section A in a circular iron yoke at a margin on the load line of 10.56%.

b_3	b_5	b_7	b_9	b_{11}	b_{13}	b_{15}
0.004	-0.022	0.024	0.871	2.354	-0.040	-0.134

6.4 Resulting Coil Cross Section C

The coil cross section C is obtained in several steps from the coil cross section A by changing the objectives of the optimization routine towards a more radial design accepting a decrease in field quality. The coil cross section is shown in fig. 6.3. Tables 6.5 and 6.6 show salient electromagnetic properties and the relative multipole errors of the coil cross section C (CCS C).

The coil cross section C is optimized for a margin on the load line of 90%, the excitation current is slightly higher as for CCS A resulting in a greater stored energy and inductance.

The new position of block 3 increases the peak field in block 7 and therefore the peak field to main field ratio.

The multipole b_5 could be further reduced whereas the multipole errors b_9 and b_{11} were increased.

The inclination of block 5 could be improved but remains still at the limits.

The minimum wedge size is for all wedges around 2 mm. The insulation on the midplane was fixed to 0.2 mm and not used for the steering of the field quality. This way the production process is simplified and an option for fine tuning remains.

6.4. Resulting Coil Cross Section C

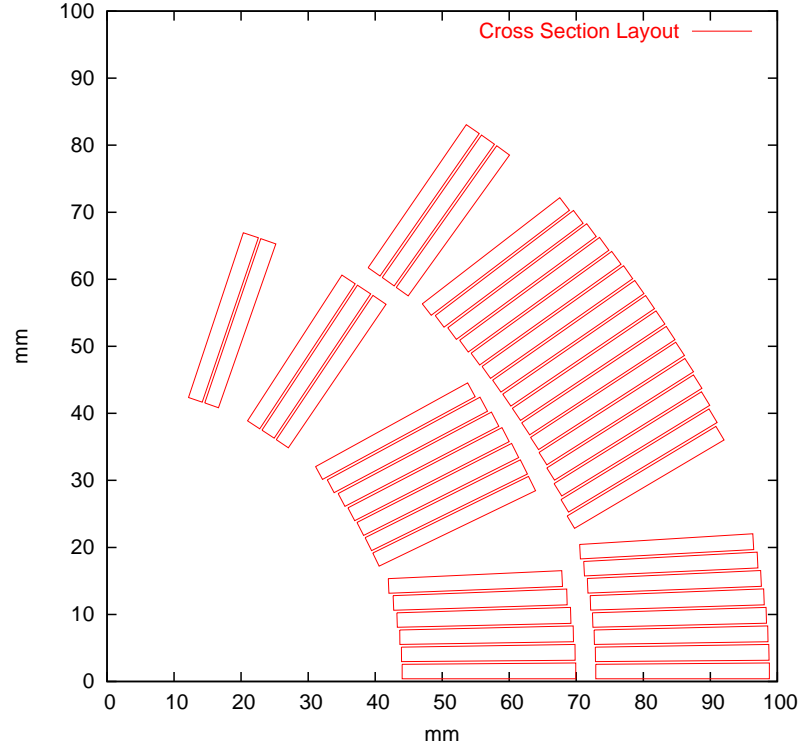


Figure 6.3: Coil cross section layout C.

Table 6.5: Salient electromagnetic properties for the coil cross section C at a margin on the load line of 10.0%.

Quantity	Value	Unit
Excitation current	25970	A
Main field B_1	-13.13	T
Peak field on conductor B_{peak}	13.55	T
Peak field / main field	1.032	-
Stored magnetic energy per unit length	1.499	MJ/m
Inductance per unit length	4.446	mH/m
Horizontal force F_x per side and per unit length	13.41	MN/m
Stress on the midplane (inner layer)	-112.0	MPa
Stress on the midplane (outer layer)	-124.4	MPa
Excitation current at 0% margin on the load line	29210	A
Peak field at 0% margin on the load line	15.02	T

Table 6.6: Relative multipole errors b_n in units of the coil cross section C in a circular iron yoke at 10.0% of the loadline.

b_3	b_5	b_7	b_9	b_{11}	b_{13}	b_{15}
0.001	0.001	0.072	1.407	2.681	-0.043	-0.171

7 Optimization of the Iron Yoke

Electromagnets usually consist of a coil which creates the magnetic field and an iron yoke which concentrates the magnetic flux. In normal conducting magnets the flux is guided by the permeable material and the field quality is mainly influenced by the shape of the poles.

For superconducting magnets the usage of the iron yoke is different. By means of the higher currents in superconducting magnets it is possible to obtain a higher field strength and so the limit of about 2 T [30, p. 68] for conventional magnets can be exceeded. At the same time the linear field range of the commonly used magnetic materials is left. The iron material saturates and cannot guide the magnetic flux in the same way as for conventional magnets.

The main purpose of the iron yoke in superconducting magnets is to increase the main field and to reduce the fringe field. Consequently, the iron yoke makes it possible to obtain higher main fields for the same excitation current. The simplest geometry serving this purpose is a hollow cylinder of permeable material surrounding the coil. In this way, the field quality is mainly determined by the position of the conductors. The magnetic behavior of such a geometry made of linearly permeable material is analytically studied in chapter 5.

The multipole errors of high-field superconducting magnets consist of three main components. The field error created by the distribution of the conductors, the field error created by the repercussion of the surrounding iron yoke and the field error induced by the persistent superconductor magnetization currents. In the subsequent sections it is shown for different shapes of the iron yoke how the magnetic field and its quality vary with increasing excitation current due to saturation of the material.

Based on these investigations the design for the iron yoke of the NED magnet is chosen and optimized. Changes in the shape of the surrounding iron yoke result in a second optimization of the chosen coil cross section.

7.1 Effect of the Iron Saturation

For the investigation of the influence of the iron saturation on the magnetic field of a superconducting magnet the optimized coil cross section from section 6.3 and the base line iron yoke of the NED collaboration (section 2.2.2) are used.

The optimization of the coil cross section was carried out for the operation point (at around 90% of the loadline) and there the iron saturation was already considered in the numerical calculations. Now, the variation of the main field and the multipole errors with increasing excitation current is investigated. The excitation range covers 10% to 100% of the current at the operation point.

7.1. Effect of the Iron Saturation

Figure 7.1 shows the variation of the main field and the lower order relative multipole errors with increasing excitation current. Figure 7.2 shows the distribution of the relative permeability of the circular iron yoke for three selected excitation currents.

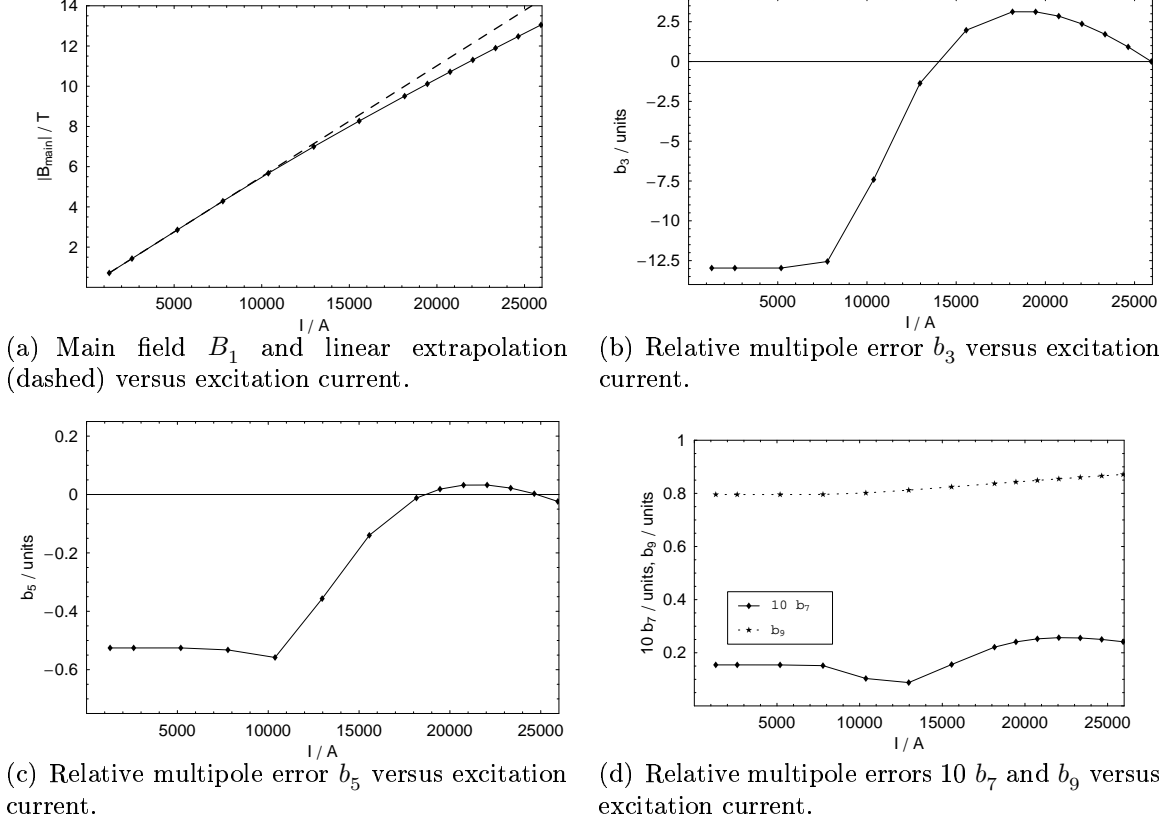


Figure 7.1: Variation of the main field and the lower order multipole errors due to iron effects for a circular iron yoke. The inner radius is set to 125.4 mm and the outer radius is set to 475.4 mm.

Both, the main field and the multipole errors show a linear behavior for excitation currents below approximately 7.5 kA. For the main field this is pointed out by the linear extrapolation (dashed line) shown in fig. 7.1 a). The relative multipole errors are constant and thus the multipole errors increase linearly with the excitation current. Figure 7.2 a) shows that the iron yoke at this excitation current is not saturated and the relative permeability is homogeneous and of high value. It can be expressed by means of the analytic solutions derived in chapter 5.

After the saturation level is reached, the yoke permeability decreases such that the increase of the main field stays below the linear extrapolation. Consequently, keeping the same current slope yields less and less increase in the main field. Regarding this in terms of the imaging method it can be seen that the weight of the image currents decreases with decreasing permeability of the iron yoke.

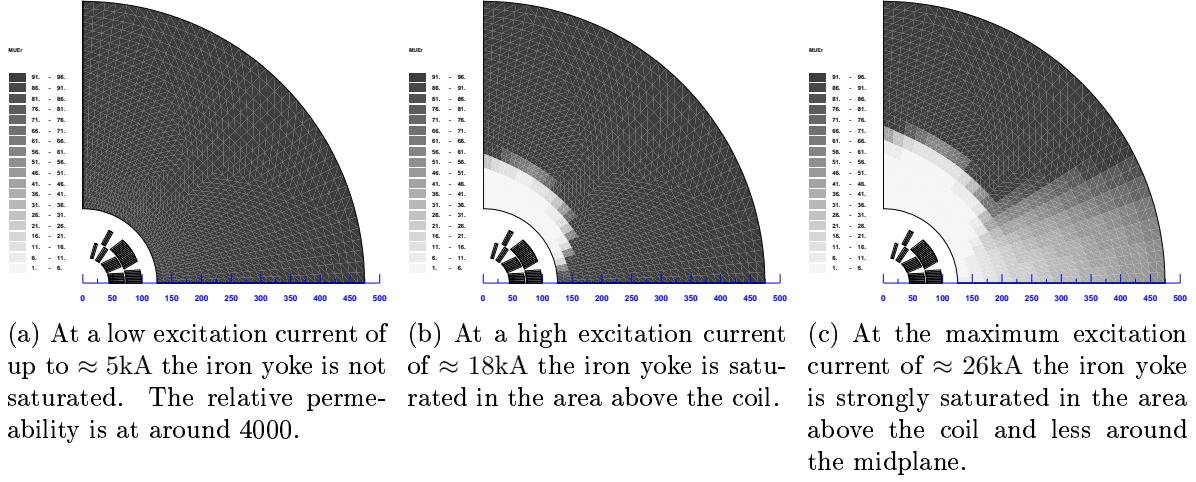


Figure 7.2: Distribution of the relative permeability of a circular iron yoke for different excitation currents. The lighter the color of the areas in the yoke, the smaller is the relative permeability. The calculation has been carried out with **ROXIE**.

With the saturation of the iron yoke, the relative multipole errors b_3 and b_5 increase until they reach an extreme value. The relative permeability of the iron yoke at the current where b_3 is extremal is shown in fig. 7.2 b). The yoke is saturated mainly in the area above the coil. When the excitation current is further increased, the iron yoke also starts to saturate around the midplane especially in close vicinity to the coil. The multipole errors decrease again until they reach the optimized values of the cross section.

Table 7.1 shows the width of the variation of the lower order relative multipole errors.

$$\Delta b_n = |\max(b_n) - \min(b_n)|.$$

The variation decreases with increasing multipole error, except for multipole b_9 for which the variation is slightly bigger than for b_7 . This might be due to the fact that the cross sections shows an inherent big value of b_9 . Because of the smaller influence of the iron yoke on the higher order multipole errors and their smaller relevance, only the variation of b_3 and b_5 is considered in the following studies.

Table 7.1: Value of the maximum variation Δb_n of the relative multipole errors for a current ramp from 1.3 kA to 26 kA.

Δb_3	Δb_5	Δb_7	Δb_9
16.1	0.59	0.017	0.076

The numerical calculation of the coil cross section is repeated without the iron yoke. For each excitation step, the obtained main field is compared with the results above and the relative difference is shown in fig. 7.3. In the non-saturated state, the contribution

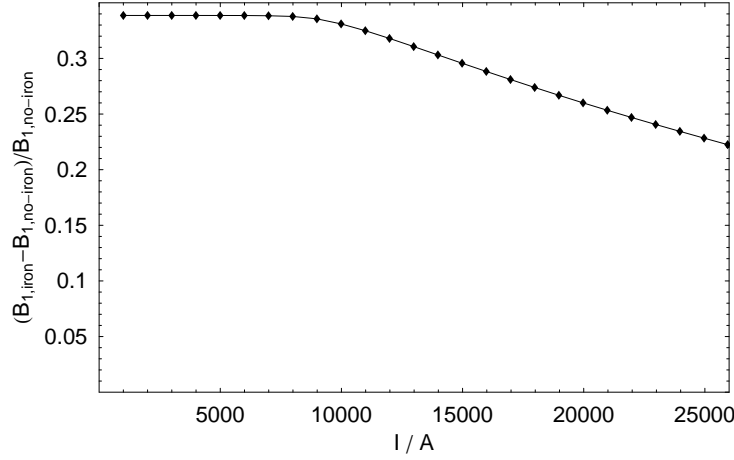


Figure 7.3: Iron contribution to the main field.

of the iron yoke to the main field is of around 33%. When the saturation starts the field enhancement begins to decrease and reaches 22% at the operating point. As shown in section 4.4, the number of conductors required to reach a certain field decreases directly with the iron yoke contribution. This relatively high contribution, even at high fields and saturation, is due to the small distance between the yoke and the coil¹. The reduction of the iron contribution due to saturation and the limitation of the current density in superconductors yield strong limits for the design of superconducting high-field magnets.

7.2 Optimization Goals

In the previous section the variation of the relative multipole errors with increasing excitation current is shown for a simple circular iron yoke. Depending on the precise application of the magnet, limits are given for each multipole error and their variation. For this study an application in a circular particle accelerator like the LHC is assumed.

For the LHC, the particles are accelerated by a chain of preaccelerators before the beam is injected into the LHC ring. After injection the energy of the particles and synchronously the magnetic field is further increased. Since the field quality influences the lifetime and quality of the beam, limits for the multipole errors are given for all excitation levels. Especially at beam injection and at maximum energy when the experiments take place, a

¹By means of Eq. (5.59) it is possible to calculate the mean positioning radius r_M of the considered design. An equivalent coil is assumed yielding the same iron contribution ($k_I - 1$) if incorporated in the iron yoke with inner radius a :

$$r_M = a\sqrt{k_I - 1} = 125.4 \text{ mm} \sqrt{0.33} = 72 \text{ mm}.$$

Note, that the thermal contraction factor cancels out and thus the obtained value for r_M is at room temperature. The calculated value is greater than the value widely assumed in chapter 5 (there it was $a/2$).

high field quality is necessary.

For the magnet geometry of the previous section (coil cross section A) the good-field-radius (section 3.6) is given in fig. 7.4. Although, as mentioned before, this value carries no precise meaning for the beam dynamics, it indicates well how the transversal space of high field quality changes with the excitation current.

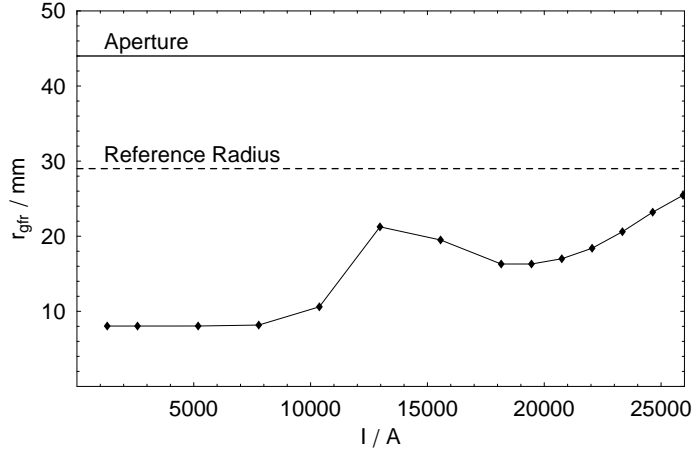


Figure 7.4: Good-field-radius for the optimized coil cross section A with the NED base line iron yoke.

By modifying the coil cross section, the field quality of a magnet can be optimized for a single value of the excitation current. If this is done, *e.g.*, for the operation point, the field quality during ramp up is not considered and usually deteriorates. By reducing the variation of the multipole errors, the optimization of the coil cross section for any working point also increases the field quality of the whole ramp cycle.

Note, that the field quality is further deteriorated if field errors induced by the so-called persistent superconductor magnetization currents are taken into account. These field errors show a hysteresis which, in a rough approximation, can be added symmetrically to the field error of the coil and the iron yoke and is strongest for low excitation current. Part of this effect could also be compensated by modifications of the iron yoke, but this is not considered here. Methods for the compensation are studied in chapter 8.

In addition to the intrinsic optimization of the field quality, *e.g.*, by changing the shape of the iron yoke, it is possible to correct field errors with corrector magnets which are attached at the ends of the dipole magnets and powered independently. Since corrector magnets are also limited in field strength, an upper limit for the possible correction is given: It has to be taken into account that corrector magnets are much shorter than the dipole and, in this way, the beam stays only a fraction of the time inside the field of the corrector magnet. Furthermore, a relative multipole field error b_n of 1 unit at low and high excitation represents a multipole error B_n of one magnitude difference. For this reason a design with low field errors at high excitation is more favorable.

7.3 Model of the Iron Yoke Saturation

In section 7.1 it was shown that the variation of the multipole errors is related to the change of saturation of the iron yoke. In order to derive methods for the reduction of the multipole variations this feature is studied in greater detail.

For the iron yoke laminations a saturation field of 2 T is assumed. This is little less than what can be read off from the BH-curve, it is simply representing the point where the relative permeability starts to decrease. For the circular iron yoke of the specifications the magnetic field is calculated by means of the field computation program **ROXIE** in steps of 2000 A. The contour of 2 T is marked inside the iron yoke. The result is denoted as saturation history and shown in fig. 7.5. It can be seen that, for the considered magnet

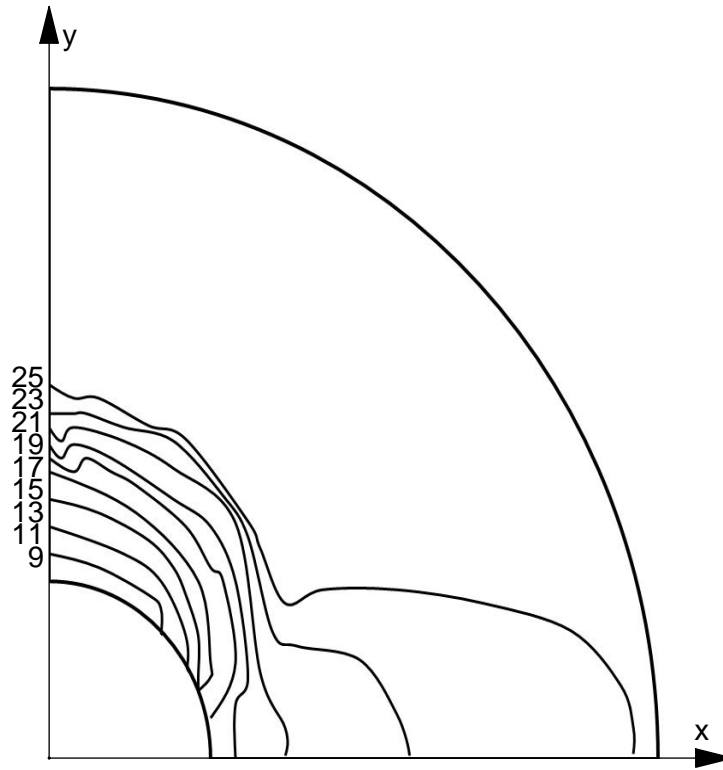


Figure 7.5: The saturation history of the iron yoke geometry according to the NED specifications and the coil cross section A for a current ramp from 0 to ≈ 26 kA. The line indicates the contour of 2 T for different excitation currents indicated on the ordinate.

cross section, the saturation starts at around 8 kA in the area above the coil and then propagates towards the midplane. The saturation in the midplane starts for a current at around 17 kA.

The influence of the saturation of the iron yoke on the multipole errors can be depicted by locally applying the imaging method and considering the multipole sensitivity as shown

in section. 3.4. In this rough estimation it is assumed that the permeable material is either of infinite permeability and non-saturated or of the same permeability as empty space and saturated. This way the inner contour of the iron yoke is given by the 2 T-contour in every excitation step.

For a given excitation step a small sector of the magnet cross section is considered. The saturation contour can be approximated by a circle. By applying the imaging method for all line currents in the considered sector the influence of the saturated iron yoke can be estimated. As shown in section 5.2.1, the radial position of the virtual image currents r_v is given by

$$r_v = \frac{R_{\text{img}}^2}{r_I}, \quad (7.1)$$

where R_{img} denotes the imaging radius and r_I is the radial position of the considered source current. With growing saturation and increasing imaging radius R_{img} the virtual image currents move outwards and their contribution to the multipole errors decreases.

For a non-saturated iron yoke the contribution of a line current to the total multipole error can be explained by means of the sensitivity scheme shown in fig. 3.5. Each line current and its image current contribute according to their radial and angular position. Comparing the non-saturated state to any step where the iron saturation has to be taken into account, the change of the multipole errors is caused only by the changing image currents. The angular position of the saturated area in combination with the number of conductors in one sector can be mapped to the influence on the multipole errors by means of the sensitivity scheme. The combination of the saturation history and the angular sensitivity scheme is shown in fig. 7.6 for the first three relative multipole errors.

Applying this approach to the results for the circular iron yoke shown in fig. 7.1, the curve propagation can easily be explained for b_3 and b_5 . The considered cross section covers a sector of approximately 75° of which the main part is below 50° . The saturation starts above the coil and only the outer blocks are affected. For b_3 this happens in the negative domain and thus the multipole error increases. For b_5 this happens in the positive domain at first but later also in the negative. Consequently, b_5 decreases first then the value starts to increase again. When the saturation of the midplane starts, the positive domains of both multipole errors are affected and they decrease. Because of the smaller angular size of the positive domain for b_5 , this decrease starts later than for b_3 .

This estimation is rather rough since it assumes only two states of saturation and it applies the imaging method very locally and sector-wise without taking into account saturation contours with acute angles like noses and corners. Nevertheless, it allows to get an overview of how the saturation affects the multipole errors and how these could be compensated.

For the reduction of the variation of the multipole errors two main approaches can be derived. The iron yoke shape can be adapted such that it behaves as if in saturated state, *e.g.*, by changing the shape of the inner contour, or the saturation history can be changed in order to amplify or damp certain contributions to multipole errors. This can be subdivided into the approach of preventing the iron yoke from saturation, for instance, by increasing

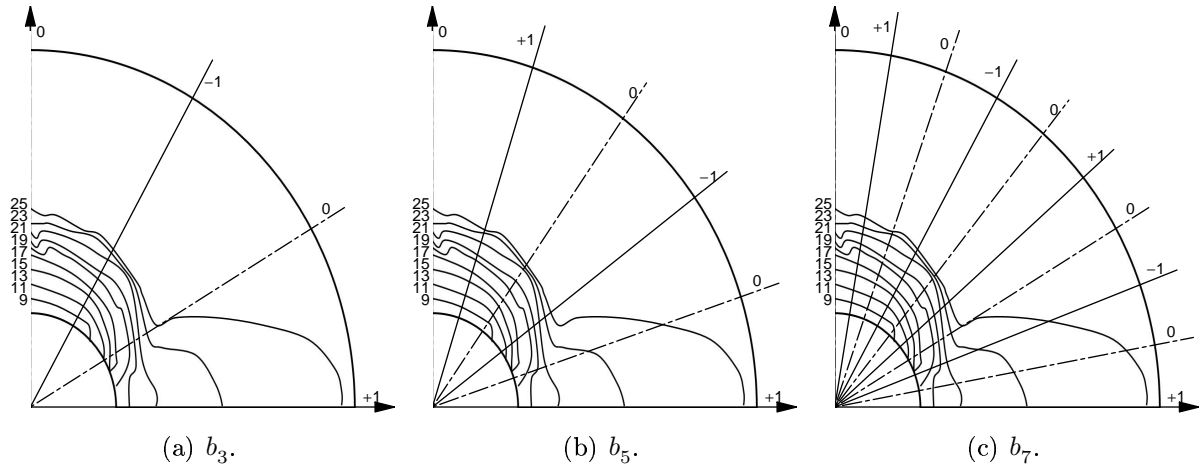


Figure 7.6: Angular multipole sensitivity scheme for the lower order multipole errors in combination with the saturation history of the coil cross section A inside the yoke specified for NED. The bigger the distance between yoke contour and saturation contour, the smaller is the contribution of all currents in this sector to the multipole error.

its size or by forcing the saturation to take place in certain parts by introducing holes in the yoke laminations.

7.4 Study of Different Approaches

Different modifications of the shape of the iron yoke are investigated starting from the coil cross section and iron yoke shown in section 7.1. The study demonstrates how the shape of the outer yoke contour, circular holes within the iron yoke domain and the shape of the inner yoke contour influence the relative multipole errors.

The different approaches are studied independently although a combination might be more effective as well as cancellation of the effects of two modifications could be possible.

7.4.1 Variation of the Outer Yoke Radius

The outer radius of the iron yoke is varied in steps of 100 mm. The geometry is shown in fig. 7.7. The basic yoke geometry for NED is indicated by the gray area.

Figure 7.7 c) and d) show the variation of the relative multipole errors b_3 and b_5 versus excitation current for different outer yoke radii. The graphs for different radii are stacked from the smallest radius on the bottom to bigger radii on the top (The graph of the calculation of b_5 for 175 mm is exceptional).

For all graphs, except the one for the very thin yoke, the first two calculated values are almost identical and only very little difference can be seen in the third. Therefore

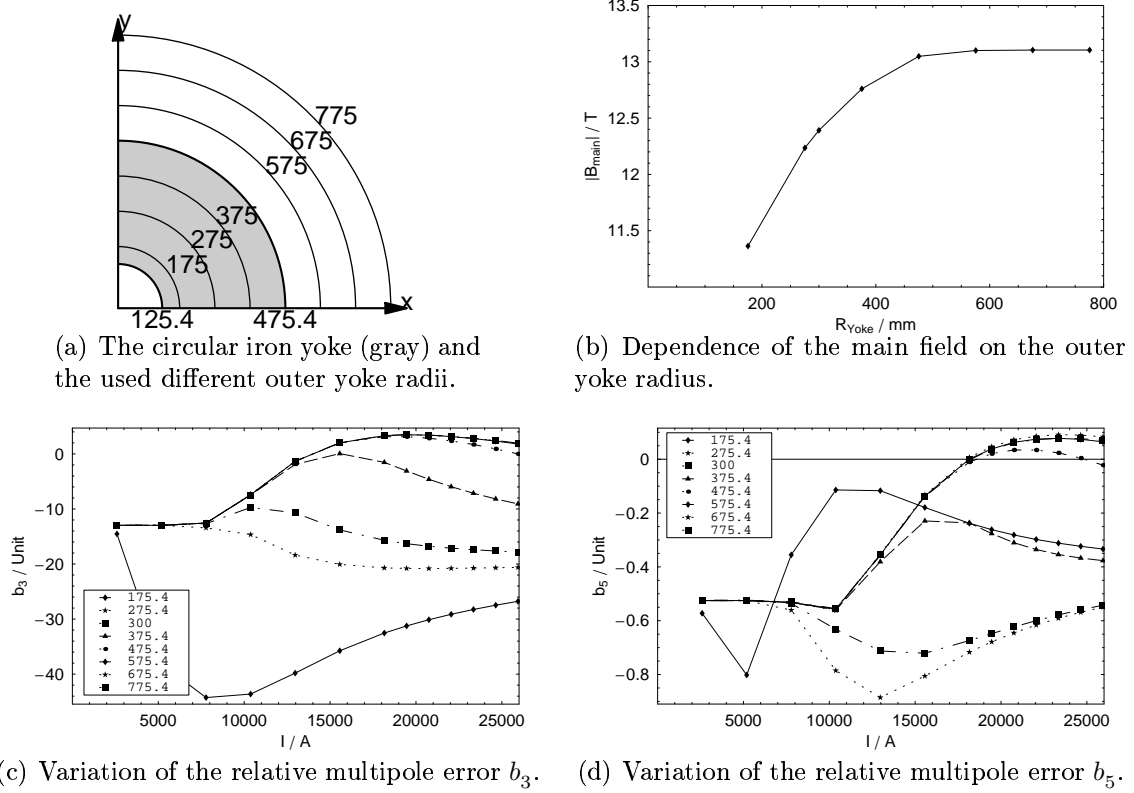


Figure 7.7: Dependence of the main field and the lower order multipole errors on the outer yoke radius.

an influence of the two parameters yoke radius and iron saturation can be ruled out and the multipole errors are given by means of the imaging method. The so-called saturation current is then located close to the third calculation step and given to approximately 7 kA. This is in very good agreement to the analytically determined value of 7.4 kA (see section 5.2.3) giving a numerical support to the analytical approach where the iron yoke was modeled by means of the imaging method.

The strong deviation of the graph for 175 mm is in good agreement to the analytical results presented in section 5.3.1. According to fig. 5.11 a deviation of more than -1% of the main field B_1 compared to the imaging method is expected for a ratio of outer to inner radius of $175/125 \approx 1.4$. At the same time the other multipole errors, *e.g.*, B_3 and B_5 are reduced less with increasing order. In this way the modulus of the relative multipole errors is bigger compared to the imaging method.

For all shown outer yoke radii, the multipole errors change synchronously up to an individually maximum current where they leave the common track. Up to this current the variation of the multipole errors is only due to the iron saturation and not influenced by the size of the iron yoke. This way a minimum thickness for a given excitation current or a maximum current for a given iron yoke can be estimated. For the NED radius of 475.5 mm

this current is given to ≈ 17 kA. For an outer yoke radius of more than 575 mm no effect of the yoke thickness can be seen.

The results for 257.4 mm and 357.4 mm signify the existence of a certain outer radius which is maximally reducing the variation of both multipole errors. This was found to approximately 300 mm and gives a variation of b_3 of only 8.1 units and at the same time a variation of b_5 of 0.19 units.

Figure 7.7 b) shows the modulus of the main field versus the outer yoke radius. It can be seen, that the main field decreases strongly with decreasing outer yoke radius. A compensation of the multipole variation by reducing the yoke radius is always paid by a reduction of obtainable main field. For the solution of 300 mm the main field is reduced by 0.66 T compared to the calculation using the NED specifications. On the other side, increasing the specified outer yoke radius by 100 mm yields a small increase in field strength of only 0.05 T, but the amount of iron material is increased by $\approx 150\%$.

In addition to the loss of obtainable main field, the reduction of the outer iron yoke radius comes with the flaw of increasing the fringe field (as shown in section 5.3.2) which must not exceed certain limits for security reasons [28].

7.4.2 Variation of the Outer Yoke Contour: Cut Off

In order to determine how a change of the outer iron yoke contour influences the main field and multipole errors, a segment of a circle is cut off either above and below parallel to the midplane or left and right perpendicular to the midplane. The height of the segment of the circle is denoted as cut off length and varied within the investigation.

From the mechanical point of view such a modification of the outer iron yoke shape is not very favorable because it makes it more difficult to apply a homogeneous pressure to the iron yoke. For this reason the shape of the cut off would have to be modified or a segment of a circle made of a non magnetic substitute material would have to be added.

Figure 7.8 a) to d) shows the results for a cut off above and below the iron yoke. It can be seen that the relative multipole errors are affected only for very big cut off lengths like 200 mm or 300 mm the relative multipole errors are affected.

The cut offs above and below the coil do not allow to reduce the variation of the relative multipole errors, but they indicate in which part of the iron yoke cross section necessary modifications could be placed without changing the field quality. These are, *e.g.*, heat exchanger holes for the liquid helium or bus bars which are used for the superconducting leads going to sequent magnets (for series connection).

Figure 7.9 a) to d) show the results for a cut off on both sides of the iron yoke. Contrary to the previous case this modification shows a big effect on the relative multipole errors directly proportional to the cut off length.

The cut offs at the sides are subject to the same restrictions as the reduction of the outer iron yoke radius: Considering the result for a cut off length of 200 mm, it can be seen that, although the variation of b_3 is reduced to a value of only 5 units, the main field is also reduced by 0.54 T. In addition the fringe field would have to be investigated more closely.

These results show that the iron around the midplane is more important than on the y -axis. This can also be seen from the plot of the relative permeability for very high excitation currents (fig. 7.2 c)) which shows big non saturated domains above the coil whereas the parts on the side are already saturated up to the outer yoke boundary.

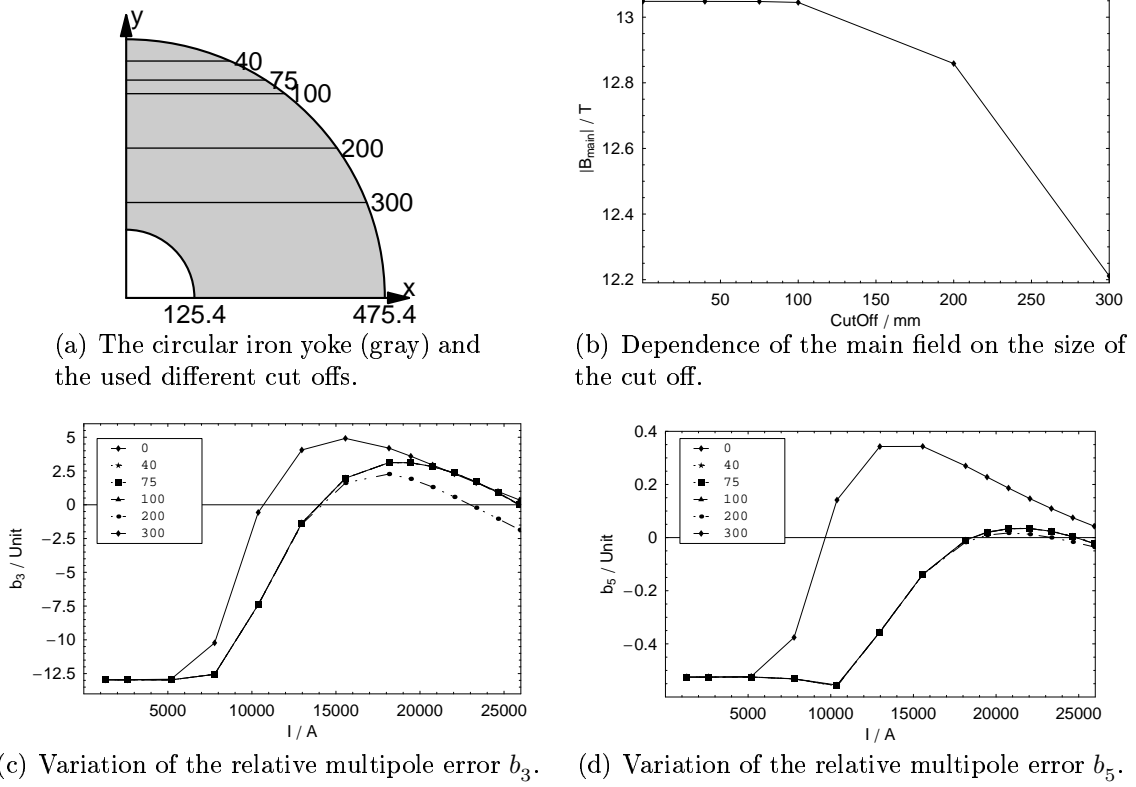


Figure 7.8: Main field and the lower order multipole errors for circular iron yoke with material cut off above the coil.

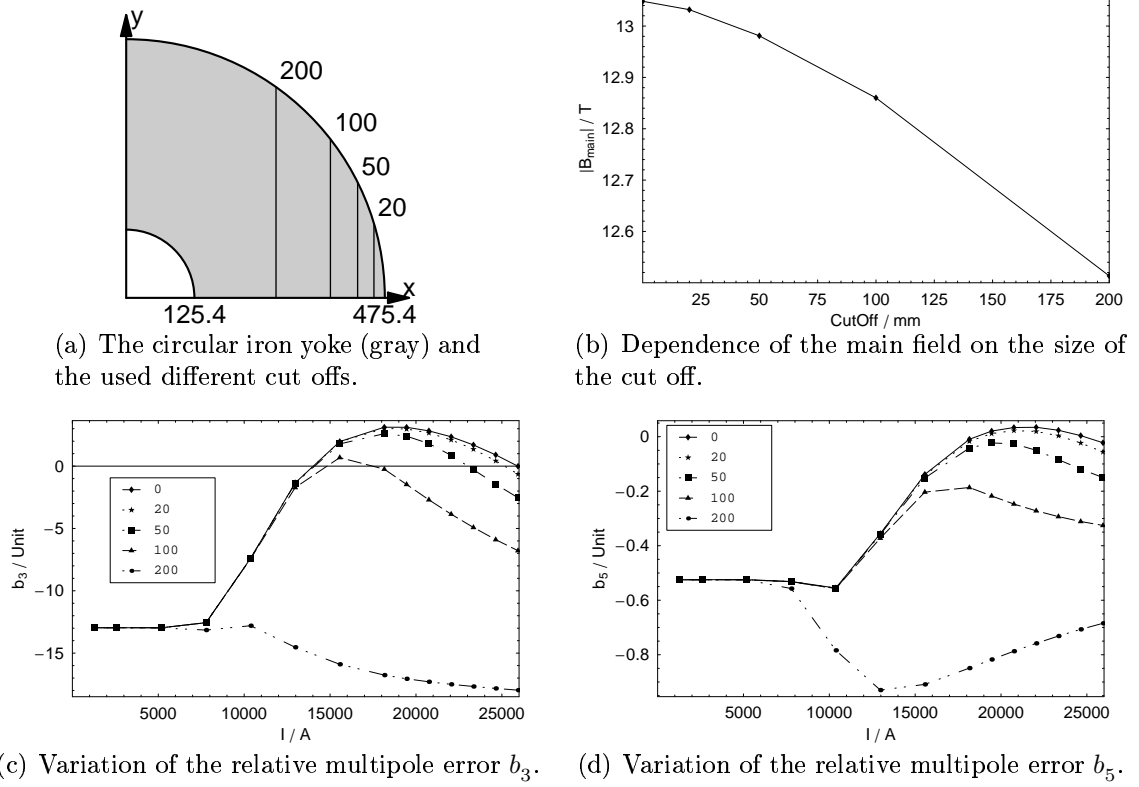


Figure 7.9: Main field and the lower order multipole errors for circular iron yoke with material cut off at the side.

7.4.3 Introducing Holes in the Yoke Laminations

By punching holes into the iron yoke laminations, the saturation history can be modified. Holes in the iron laminations act like fully saturated regions. In terms of the simplified model shown in section 7.3, the image currents are moved outwards and the corresponding multipole errors are strongly reduced. In addition, since the magnetic flux is guided around the hole, the flux density close to the hole is increased and forces the material into earlier saturation.

Figure 7.10 shows the NED iron yoke with an arbitrarily placed hole. The center of the hole is given by the radial ρ_H and angular ϕ_H position, and the hole radius is R_H .

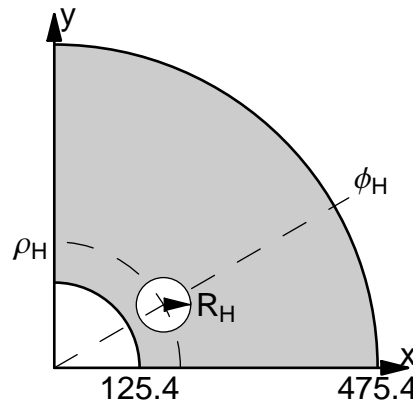


Figure 7.10: Definition of the hole punched into the iron yoke laminations.

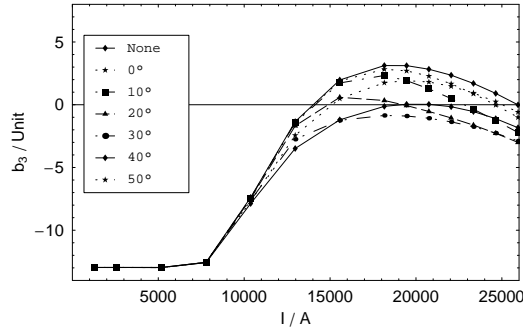
The iron yoke is used to transmit prestress from the shrinking cylinder to the collar and thus requires a certain mechanical rigidity and stability. This limits the maximum size of the hole and implies a minimum distance of the hole to the yoke boundary. These values are set to a minimum margin of 20 mm and a maximum hole radius of ≈ 40 mm.

For a hole of 15 mm radius and a radial distance to the magnet center of 160.4 mm, leaving the minimum margin of 20 mm, the relative multipole errors are calculated for varying angles ϕ_H . The results for b_3 (top) and b_5 (bottom) are shown in fig. 7.11 separated into results which decreased the variation (left) and those which cause an increase (right).

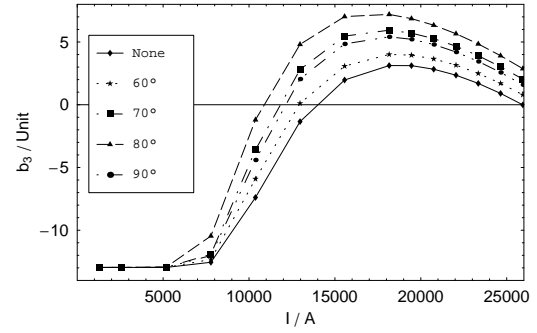
The angles reducing the variation of the multipole errors are different for b_3 and b_5 . For the multipole b_3 the variation is reduced for holes between 0° and 50° whereas the reduction is most pronounced around 30° . The variation of the relative multipole error b_5 is reduced for angles from 0° to 30° and from 80° to 90° . The maximum reduction is around 20° .

The correlation between the position angle of the punched hole and the reduction of the multipole variation is in good agreement with the theory of the saturation history. The uncertainty is of $\approx 10^\circ$ and related to the forced flux concentration.

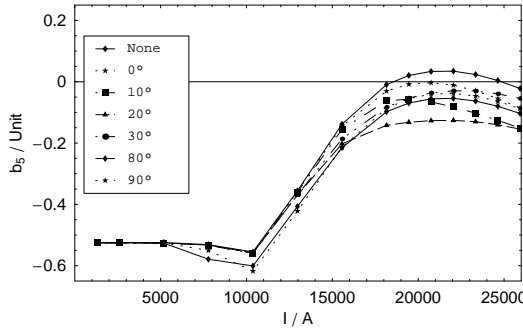
Since the optima for b_3 and b_5 are at different angles, a tradeoff has to be found. Because of the greater variation of b_3 and its stronger impact, the following calculations are carried



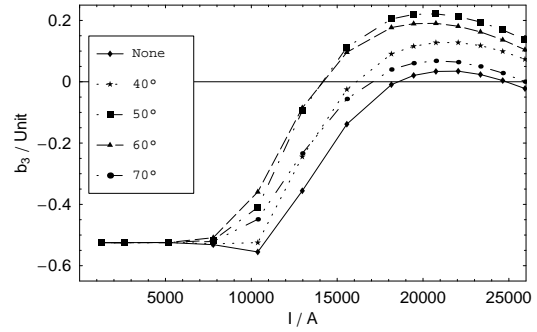
(a) Variation of the relative multipole error b_3 (decrease of the amplitude).



(b) Variation of the relative multipole error b_3 (increase of the amplitude).



(c) Variation of the relative multipole error b_5 (decrease of the amplitude).



(d) Variation of the relative multipole error b_5 (increase of the amplitude).

Figure 7.11: Dependence of the lower order multipole errors on the angular position of a hole punched into the iron laminations. The radial position is $\rho_H = 160.4$ mm and the hole radius is $R_H = 15$ mm.

out for a hole position angle ϕ_H of 30° . Figure 7.12 shows the multipole variation for different radial positions ρ_H .

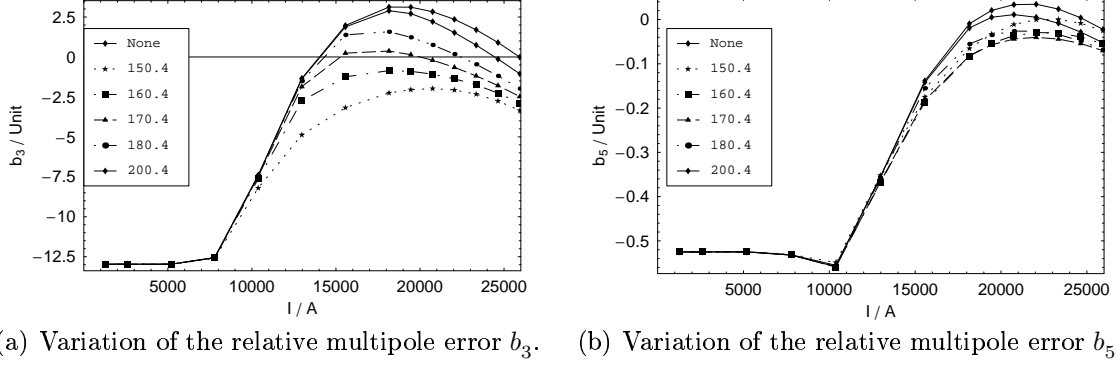


Figure 7.12: Dependence of the lower order multipole errors on the radial position of the hole punched into the iron laminations.

For b_3 , the influence of the hole inside of iron yoke clearly increases with decreasing distance. The same effect can be observed for b_5 down to a distance of below 30 mm (or radius of less than 170.4 mm). A further decrease of the margin to the inner contour reduces the influence again.

The influence of the hole radius R_H is studied at a positioning angle $\phi_H = 30^\circ$ and the constant distance of 20 mm. Therefore the radial position is given by the inner yoke radius r_{Yi} and the distance to:

$$\rho_H = r_{Yi} + 20 \text{ mm} + R_H$$

The influence on the relative multipole errors and the main field is shown in fig. 7.13. With increasing hole radii the main field is reduced as well as the variation of both multipoles.

Punching holes into the iron yoke laminations has demonstrated to be a flexible way to reduce the variation of the lower order multipoles. The best result was obtained for holes of 40 mm radius at 30° in a distance of 185.4 mm. The variation for b_3 is reduced to ≈ 5 units whereas the main field is reduced by 0.2 T at the same time.

The reduction of the main field as well as mechanical issues have to be investigated more closely.

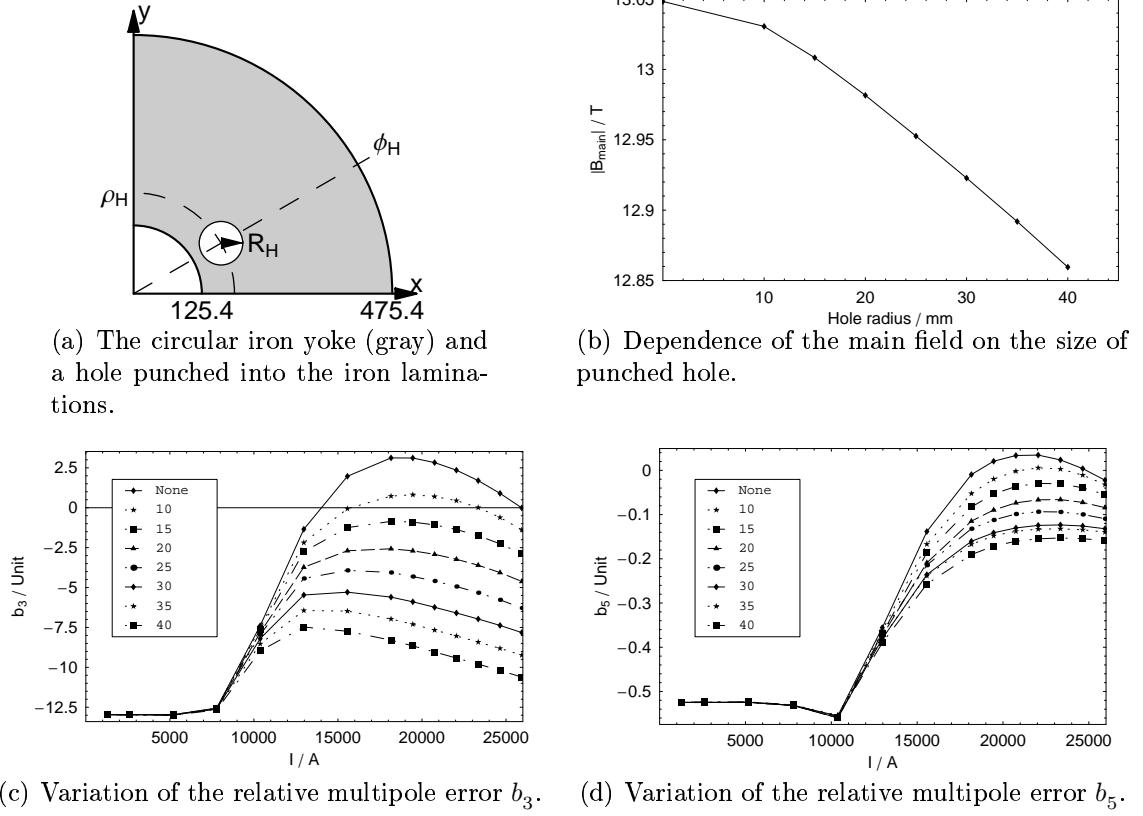


Figure 7.13: Dependence of the main field and the lower order multipole errors on the size of the hole punched into the iron yoke laminations.

7.4.4 Variation of the Inner Yoke Contour: Ellipse

For high excitation currents and thus high fields, the effective shape of the highly permeable domains inside the iron yoke differs strongly from the shape at low excitation which is given by the shape of the iron yoke. As shown in the saturation plot (fig. 7.5), the saturation starts first in the area above the coil. Only for very high currents (above ≈ 18 kA) it propagates towards the midplane. A reduction of the material in this area changes the multipole errors at low excitation currents in a similar way as they change by saturation at high fields.

For the inner contour an elliptical shape is chosen. The semi-minor axis is situated on the x -axis and fixed to the formerly specified inner iron yoke radius of 125.4 mm. The semi-major axis is situated on the y -axis and varies in this investigation. The simulation results are shown in fig. 7.14.

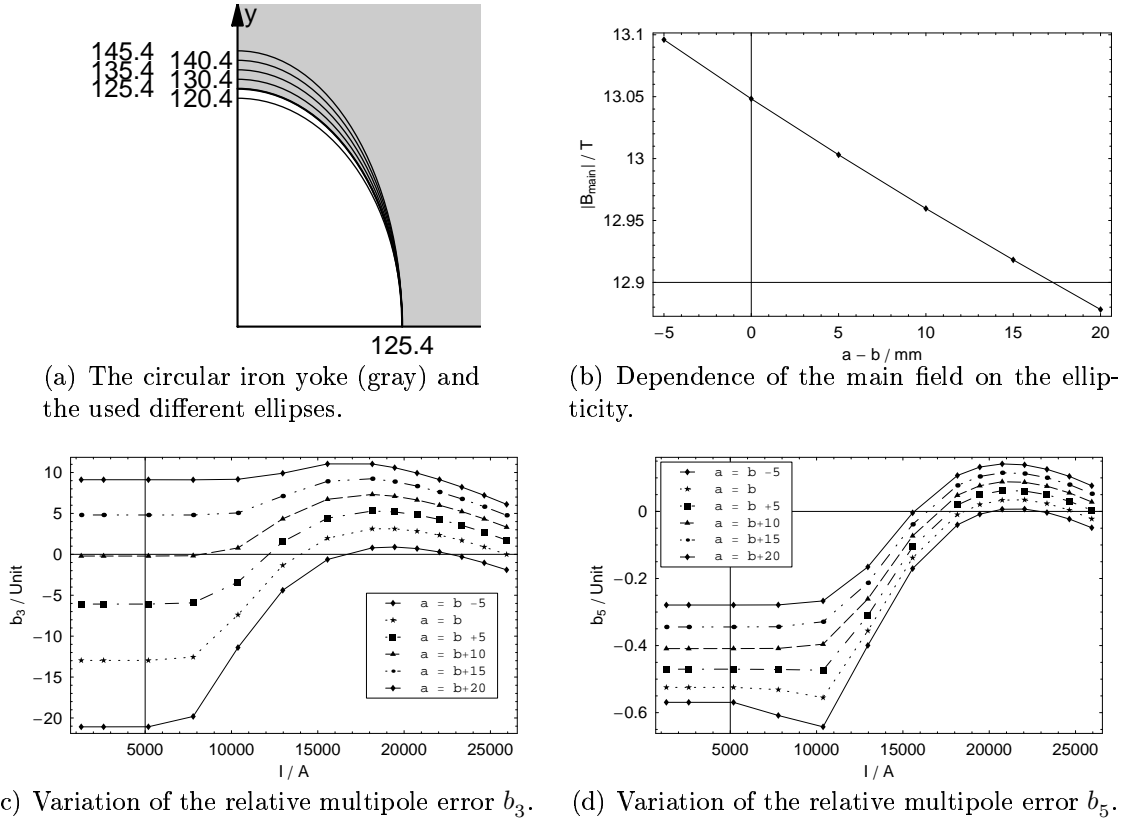


Figure 7.14: Dependence of the main field and the lower order multipole errors on the ellipticity of the inner yoke contour.

It can be seen that the main field decreases in first order linearly with increasing semi-major axis. This is due to the greater distance between the coil and the yoke contour which causes a reduction of the iron yoke contribution. A decrease of the semi-major axis, although not allowed because a minimum collar thickness has to be kept, would increase

the main field.

The increasing distance of the coil and the iron yoke contour is influencing sectors where the coil mainly contributes negatively to b_3 and b_5 . This causes a reduction of the negative fraction and consequently, the multipole errors lift at low excitation. At high excitation current constant but less strong offset can be observed.

The variation is reduced best for a semi-major axis which is approximately 10 to 15 mm larger than the semi-minor axis. The resulting variation is less than 5 units whereas the main field is reduced by around 0.1 to 0.15 T.

7.5 Final Iron Yoke Shape and Optimized Coil Cross Section

For the final shape of the iron yoke the elliptical inner yoke contour is used. This approach shows a small reduction of the main field obtained with only one single parameter and good improvement on multipoles b_3 and b_5 ².

The semi-major axis was optimized for a minimum variation of b_3 and b_5 and is given to 138.6 mm. Due to the offset on the multipole errors coming from the modification of the iron yoke, the coil cross section had to be reoptimized. The resulting coil cross section is shown in fig. 7.15. Salient magnet properties are shown in tab. 7.2 and the multipole errors at high field (8.54% margin on the load line) are shown in tab. 7.3.

Compared to the results of the coil cross section C with the circular iron yoke shown in section 6.4, the multipole errors show slightly higher values. The peak field at 0% margin on the load line decreased because of the smaller contribution of the iron in the region above the coil.

The variation of the multipole errors versus excitation current is shown in fig. 7.16. The total variation of the lower order multipole errors is given in tab. 7.4.

Figure 7.17 shows the good-field-radius for the final magnet cross section. It can be seen how the reduction of the multipole variation improved the field quality, especially at low excitation. The dip in the curve at inter-medium excitation is mainly due to the high values of b_3 . The good-field-radius is always greater than 12.5 mm. The two critical working points, beam injection and high field show a very good field quality.

²From the mechanical point of view, the punching of the ellipse as well as the force transmission between iron yoke and collar have to be further investigated.

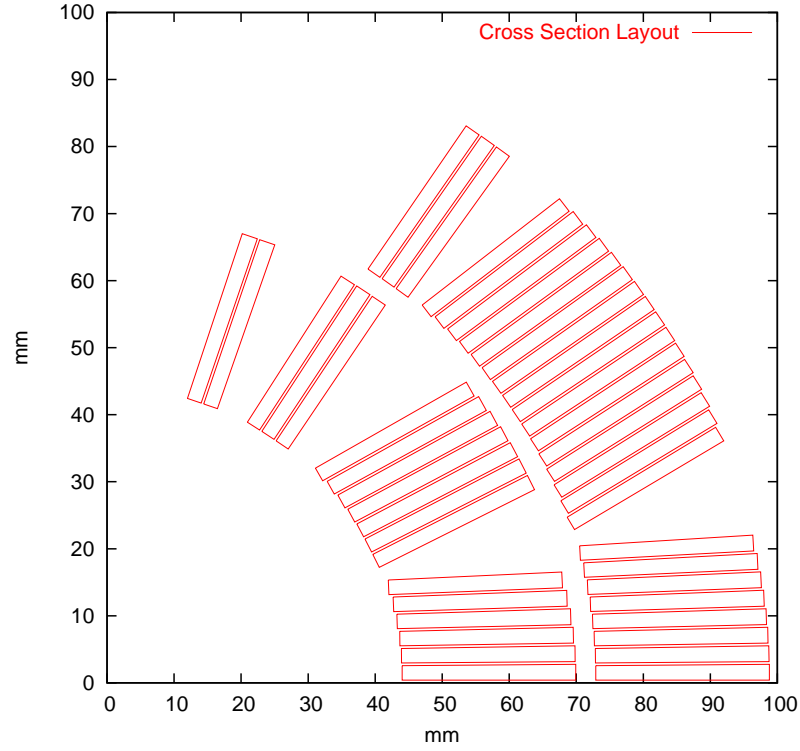


Figure 7.15: Coil cross section C optimized to be used with an elliptical iron yoke.

Table 7.2: Salient electromagnetic properties of the coil cross section C optimized for an elliptical iron yoke at a margin on the load line of 8.54%.

Quantity	Value	Unit
Excitation current	26670	A
Main field B_1	-13.31	T
Peak field on conductor B_{peak}	13.75	T
Peak field / main field	1.032	-
Stored magnetic energy per unit length	1.556	MJ/m
Inductance per unit length	4.375	mH/m
Horizontal force F_x per side and per unit length	13.79	MN/m
Stress on the midplane (inner layer)	-118.7	MPa
Stress on the midplane (outer layer)	-131.8	MPa
Excitation current at 0% margin on the load line	29440	A
Peak field at 0% margin on the load line	15.00	T

 Table 7.3: Relative multipole errors b_n in units for the coil cross section C optimized for an elliptical iron yoke at a margin on the load line of 8.54%.

b_3	b_5	b_7	b_9	b_{11}	b_{13}	b_{15}
-0.018	0.058	0.077	1.703	2.692	-0.046	-0.176

7.5. Final Iron Yoke Shape and Optimized Coil Cross Section

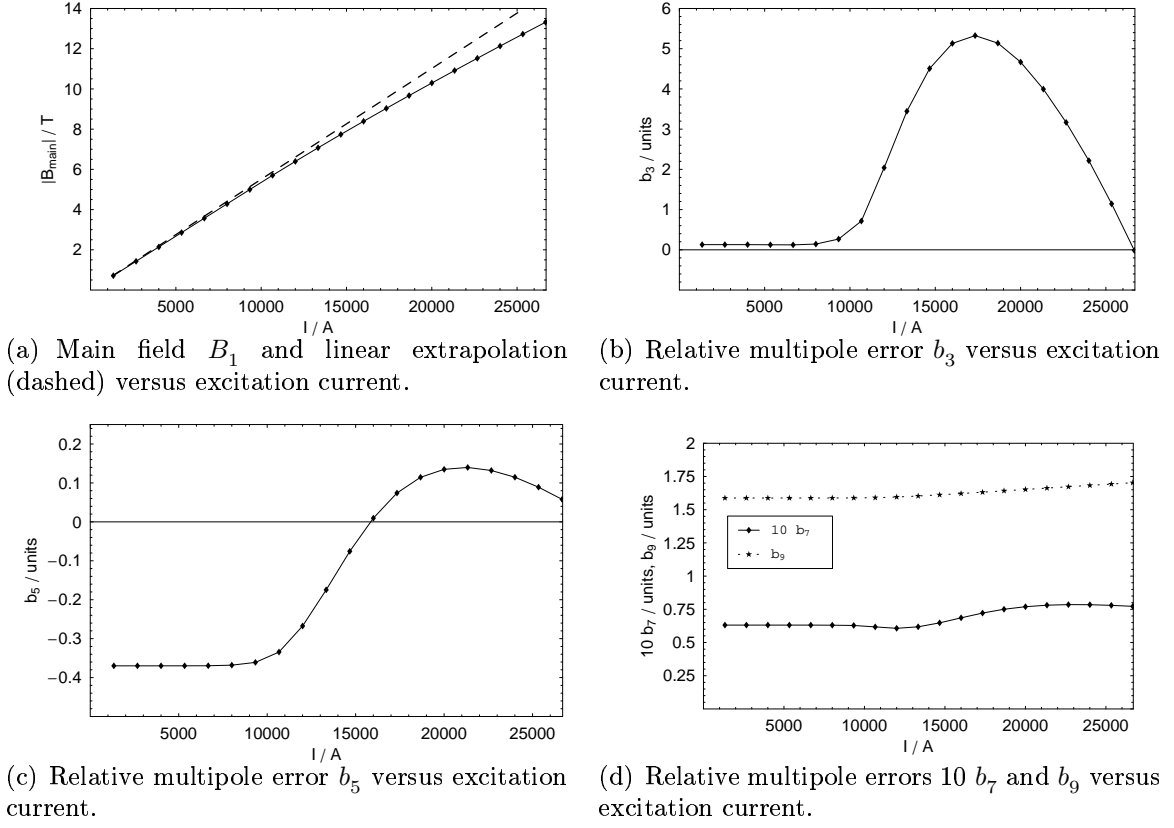


Figure 7.16: Improved variation of the main field and the lower order multipole errors for an iron yoke with elliptical inner contour. The semi-major axis is 138.6 mm and a semi-minor axis is 125.4 mm. The outer radius is set to 475.4 mm.

Table 7.4: Value of the maximum variation Δb_n of the relative multipole errors for a current ramp from 1.3 kA to ≈ 27 kA.

Δb_3	Δb_5	Δb_7	Δb_9
5.35	0.51	0.018	0.12

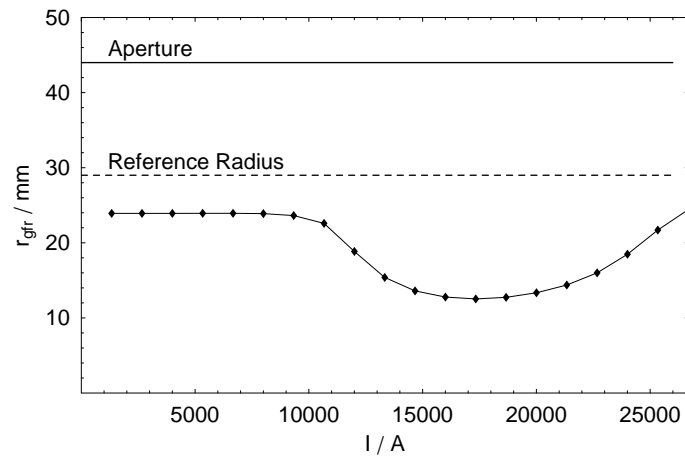


Figure 7.17: Good-field-radius for the optimized coil cross section C and the optimized elliptical iron yoke.

7.6 Conclusions

With the saturation history a satisfying tool was found for the estimation of possible yoke modifications and their impact on the multipole errors. The reliability could be demonstrated by means of all studied approaches.

Within the investigation the theoretical estimations of the saturation current and the minimum yoke thickness could be numerically supported.

Different modifications of the iron yoke in order to reduce the variation of the multipole errors were studied with the following results:

- By reducing the outer radius of the iron yoke it is possible to improve the variation of the relative multipole errors b_3 and b_5 by one half but at the same time the obtainable main field decreases by more than 4%.
- Cutting off segments of a circle at the outside of the iron yoke show that the multipole errors are much more influenced by iron yoke modifications around the midplane than in the area above the coil. This indicates on the one hand possible regions for yoke modification which should not influence the magnetic field but on the other hand does not give a proper way to reduce the variation of the relative field errors since it also suffers from a big loss in obtainable main field.
- Punching holes into the laminations of the iron yoke is a flexible way to reduce the variation of the lower order multipole errors. It has been shown that the effect can be steered by the hole position and size yielding three degrees of freedom. The relatively big hole size resulting in a reduction in obtainable main field of $\approx 1.5\%$ as well as mechanical restrictions have to be considered more closely.
- By an elliptical shape of the inner yoke contour it is possible to reduce the variation of the lower multipole errors. The main field is reduced by only 1%.

A final shape for the iron yoke was found and the coil cross section was reoptimized.

8 Study of Persistent Current Compensation Methods

The cables of superconducting magnets consist of strands and more detailed of superconducting filaments made of so-called hard superconducting materials. If such a filament is exposed to a magnetic flux density, superconductor magnetization currents are induced in order to screen the filament's center from the field. Due to the lack of resistivity, these bipolar currents do not decay with time. They persist and are denoted as persistent currents. In addition, for hard superconductors the dependence of the superconductor magnetization on the applied field of magnetic induction shows a hysteresis [20].

According to the critical state model [31], superconductors are always screened by the maximum current density - the critical current density. For low field this value is many magnitudes greater than the excitation current density. Since for any excitation current parts of the coil cross section of non negligible size remain in the low field range, the superconductor magnetization usually has to be taken into account for the calculation of the field quality [32].

The persistent current induced field errors can be calculated numerically, *e.g.*, by means of the intersecting ellipses model of VÖLLINGER [20] which is included in the field computation program **ROXIE**. Relying on the critical current density of the used strand, the screening from the field of magnetic induction is simulated for all strands of the magnet.

Since no measurement data of the critical current density of the strand going to be used for the NED magnet is available up to now, it had to be estimated by means of a similar but older strand [15]. This way a first estimation of the field errors for the NED magnet could be obtained.

Based on the calculated field errors including the superconductor magnetization, different compensation methods are studied.

8.1 Effect of the Superconductor Magnetization

For the calculation of the contribution of the persistent currents induced field errors on the total field error, the magnet cross section presented in section 7.5 is used - coil cross section C optimized for the use with an elliptical iron yoke. The critical current density of the NED strand was estimated in [15] and is shown in fig. 2.3.

For the calculation of the field errors the excitation current is ramped up to maximum current, ramped down to approximately 5% of the maximum current and ramped up again to maximum current. At the beginning of the calculation, the magnetization history is

8.1. Effect of the Superconductor Magnetization

blank and the filaments behave like directly after cool down. The first up ramp is the so-called virgin curve and it is not further investigated since in superconducting accelerator magnets, a pre-ramp is applied before beam injection.

Figure 8.1 shows the variation of the relative multipole errors for a complete current loop.

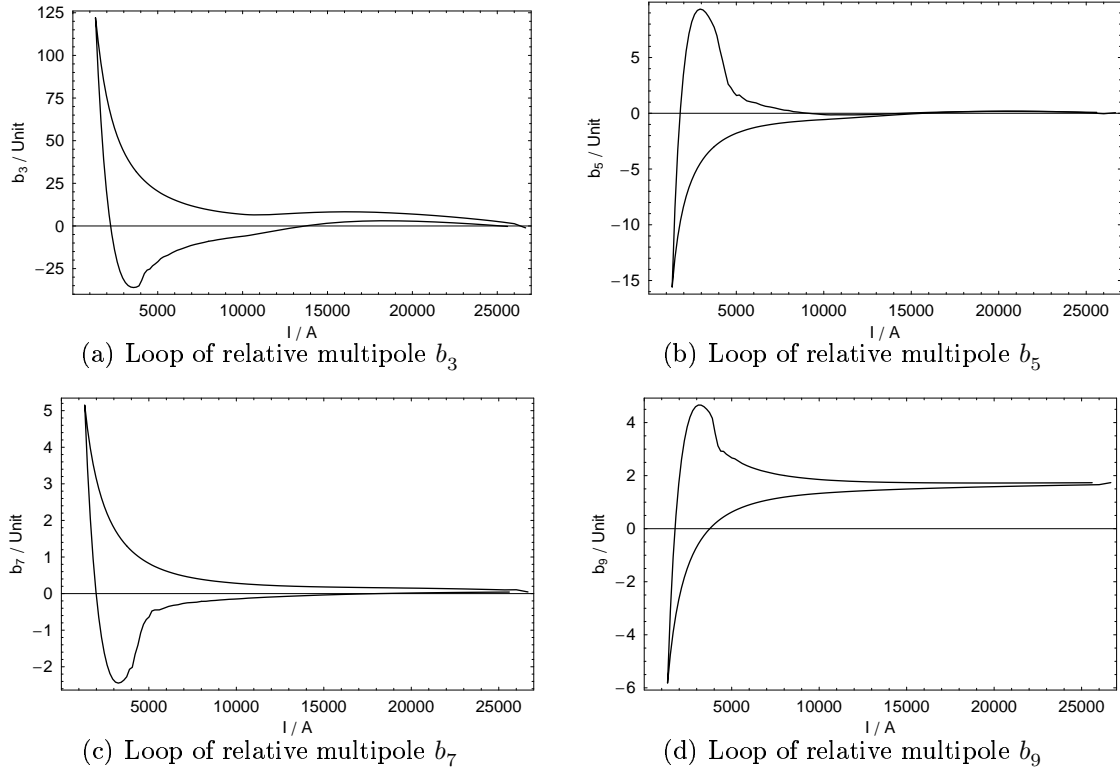


Figure 8.1: Field errors induced by the superconductor magnetization for the optimized coil cross section C with elliptical iron yoke. The current ramp cycle is from ≈ 1.5 kA up to ≈ 27 kA and down to ≈ 1.5 kA.

Like the superconductor magnetization itself, all multipole errors show a hysteresis. The loops are of different orientation, for b_3 and b_7 counter-clockwise and for b_5 and b_9 clockwise. All loops show a spike where the ramp direction is changed and a relative extreme at approximately 3 kA on the up ramp branch. The hysteresis width strongly decreases with increasing excitation current. The values at the operation point are in close vicinity of the optimized values of section 7.5.

The total variation of the relative multipole errors is much greater compared to the effect calculated for the iron yoke saturation (section 7.1). As explained in section 7.2, for accelerator applications the magnetic field is synchronously ramped up with increasing particle energy and thus only a small variation of the multipole errors during up ramp is allowed.

The strongest variation is between the spike at low excitation and the relative extreme

value. If the particles are accelerated to a higher energy with preaccelerators, only the up ramp branch needs to be considered and the strongly varying part at higher excitation currents above ≈ 3 kA can be left out. The variation above this current has to be compensated by additional elements in the cross section.

Table 8.1 shows the variation of the relative multipole errors Δb_n between the relative extreme value and approximately the value of maximum current.

Table 8.1: Variation of the multipole errors induced by superconductor magnetization currents on the up ramp branch. The variation from the extreme value at around 3 kA to the extreme value close to the maximum current is given.

Δb_3	Δb_5	Δb_7	Δb_9
40	9.5	2.2	2.4

Note that with the calculated hysteresis loops of the relative multipole errors, persistent currents induced field errors for the NED magnet are estimated for the first time.

8.2 Basic Idea of Compensation

The results of the previous section showed that the field quality is mainly deteriorated by the superconductor magnetization currents at low excitation. For high excitation the hysteresis width of the relative field errors decreases and the field error is dominated by the coil geometry and the iron yoke shape. The field error resulting from the coil cross section and iron geometry shall be denoted as geometrical field error in the following.

Figure 8.2 shows the relative multipole error b_3 calculated with the influence of the superconductor magnetization in comparison to the geometrical field error for the elliptical iron yoke. At high excitation currents it can be seen that the hysteresis loop follows the shape of the geometrical field error and in a rough approximation the persistent current induced field errors can be symmetrically added.

For the compensation of the persistent current induced field errors respectively for the reduction of the multipole variation on the up ramp branch, elements of opposite behavior are inserted. Since the effect of the persistent currents changes with excitation current and especially below the saturation current of the iron yoke, it can not be compensated by means of changing the coil cross section layout or the shape of the iron yoke.

However, ferromagnetic elements can be added to the cross section since they show a dipolar magnetic behavior which decreases with increasing saturation. By means of the position of such elements it is possible to obtain an effect on certain multipole errors and by their size it can be steered how soon their saturation starts.

With the used inserts, the geometric field error is manipulated, *e.g.*, the relative multipole errors b_3 and b_7 can be compensated by adding positive multipole values at low excitation. This way the geometrical field error is bent upwards. For an investigation of compensation techniques, it is sufficient to concentrate on the geometric field error first and to compensate

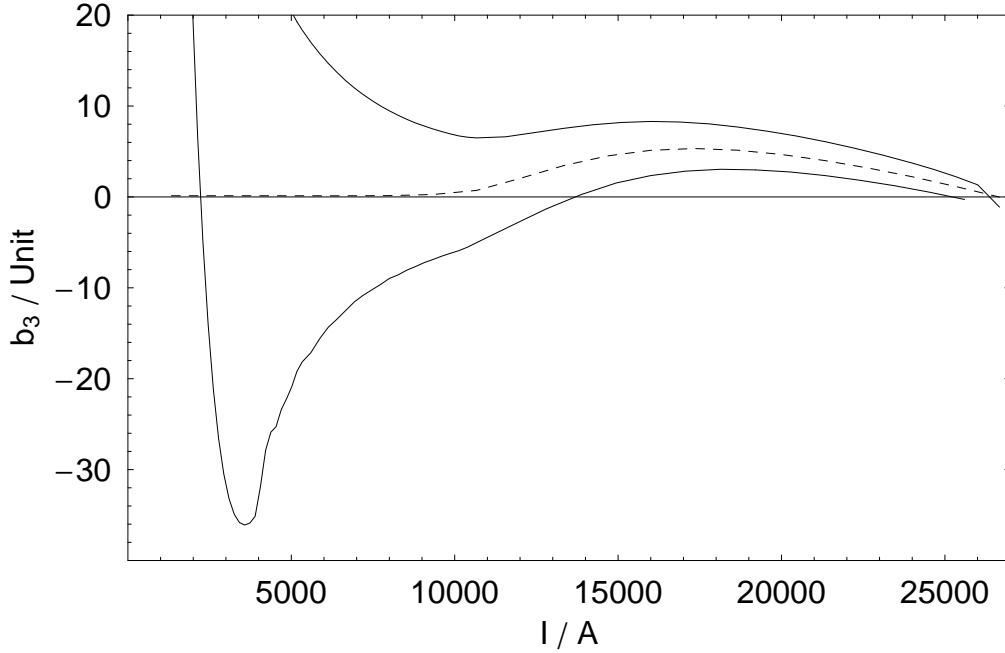


Figure 8.2: Variation of the relative multipole error b_3 due to iron saturation only (dashed line) and due to iron saturation and superconductor magnetization (continuous line).

the relative extreme value only. The effect on the persistent current induced field errors can be calculated in a second step.

Ferromagnetic shims which are placed close to the coil, are exposed to very high fields and fully saturate already for medium excitation. This way the contribution of the shims decreases with increasing excitation current. By varying their thickness, the saturation behavior and the strength of the effect can be steered.

A second way to add field errors is to place non powered superconductors in the coil cross section. These react in the same way on the field as the strands of the coil cross section and thus contribute to the total field error with the same dependence on the excitation current. Passive superconductors are not studied in this thesis. Note that both, ferromagnetic shims and passive superconductors show magnetic momenta with opposite orientation and this way their contribution is of opposite sign. Therefore the estimation shown below is also applicable for passive superconductors.

8.3 Model for the Contribution of Ferromagnetic Elements

The magnetic moment of a ferromagnetic shim is approximated by the moment of a thin rod made of permeable material. For a given field inside a magnet cross section the induced

multipole errors can be calculated by means of the analytic expression given in section 3.7. The positions of high sensitivity for the compensation of a certain multipole error can be determined.

8.3.1 Magnetic Moment of a Thin Ferromagnetic Cylinder

A thin rod inside the bore of the iron yoke is considered. The field of magnetic induction is assumed to be homogeneous as well as of linear permeability μ_{rod} . The magnetization \mathbf{M}_{rod} reads

$$\mathbf{M}_{\text{rod}} = \frac{1}{\mu_0} \mathbf{B}_{\text{rod}} - \mathbf{H}_{\text{rod}} = \frac{\mu_{\text{rod}}/\mu_0 - 1}{\mu_{\text{rod}}} \mathbf{B}_{\text{rod}}, \quad (8.1)$$

where \mathbf{B}_{rod} denotes the magnetic induction and \mathbf{H}_{rod} the magnetic field at the considered position. By multiplying the magnetization by the cross sectional area of the rod the magnetic moment per unit length \mathbf{m}'_{rod} is given¹:

$$\mathbf{m}'_{\text{rod}} = \pi r_{\text{rod}}^2 \mathbf{M}_{\text{rod}}. \quad (8.2)$$

Eqs. (8.1) and (8.2) show how the magnetic moment, representing the rod, depends linearly on the local magnetic induction, quadratically on the rod radius and decreases to zero with, due to saturation, decreasing permeability.

8.3.2 Multipole Contribution

For a known field distribution inside the bore of the iron yoke, the contribution of the thin ferromagnetic rod can be calculated analytically.

For this first estimation the coil cross section C is used inside a circular iron yoke. This way the field distribution within the magnet cross section can be calculated analytically by means of the imaging method as long as no saturation effects have to be taken into account. The field lines of the magnetic flux density, the iron yoke and the strands of the coil are shown in fig. 8.3.

¹ The rod of homogeneous magnetization \mathbf{M}_{rod} can also be replaced by the equivalent magnetization current sheet \mathbf{J}'_{mag} given by

$$\mathbf{J}'_{\text{mag}} = \mathbf{M}_{\text{rod}} \times \mathbf{n} = |\mathbf{M}_{\text{rod}}| \sin(\phi + \gamma) \mathbf{e}_z$$

where \mathbf{n} is a vector normal to the surface of the rod and γ denotes the angle of the magnetization with respect to the x -axis. In this way the rod is replaced by an ideal $\cos\theta$ dipole configuration and the magnetic moment per unit length \mathbf{m}'_{rod} is determined by the integration of the infinite small momenta $D(\phi)J'_{\text{mag}}(\phi)r_{\text{rod}} d\phi$:

$$|\mathbf{m}'_{\text{rod}}| = \int_{\gamma}^{\gamma+\pi} |\mathbf{J}'_{\text{mag}}(\phi)| D(\phi) r_{\text{rod}} d\phi = |\mathbf{M}_{\text{rod}}| \pi r_{\text{rod}}^2,$$

where $D(\phi) = \sin(\phi + \gamma) r_{\text{rod}}$ denotes the distance between pairs of infinite small line currents.

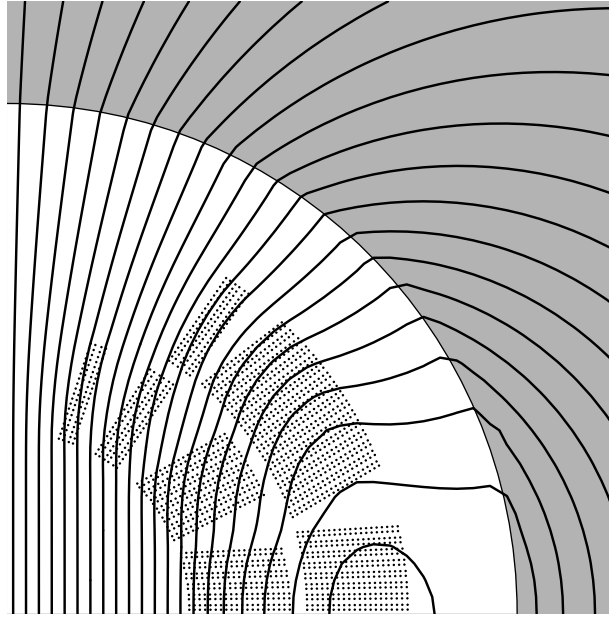


Figure 8.3: Analytical calculation of the field of magnetic induction for coil cross section C in a circular iron yoke. The calculation has been carried out by means of the imaging method and the iron yoke was taken into account by its relative permeability of 500 which represents the iron yoke at low field thus in non-saturated state.

Using this field map, the multipole contribution of such a thin rod can be calculated by means of Eq. (3.17). The sensitivity of the relative multipole errors on the rod position is calculated within the bore of the iron yoke and shown in fig. 8.4. This way, the position for compensating ferromagnetic shims can be estimated, *e.g.*, the relative multipole b_3 needs to be corrected by additional positive multipole errors and thus all white areas are of interest. At the same time b_5 has to be corrected downwards and so the best position is given by the intersection of the white domains of b_3 and the black domains of b_5 in fig. 8.4. This can be found at approximately in the area between 45° and 60° .

Note that the positive contribution for b_3 is very much limited to one sector for small radii and spreads for larger radii towards the midplane. This results from the fact that the field around the midplane at the outer coil radius is oppositely oriented to the field at the inner radius.

8.4 Study of Different Approaches

For the compensation of the persistent current induced field errors many different approaches have been suggested and published [4, 3, 5]. Although the basic ideas of the compensation approaches presented here are already known, their applicability has to be tested for every type of cable and magnet cross section individually.

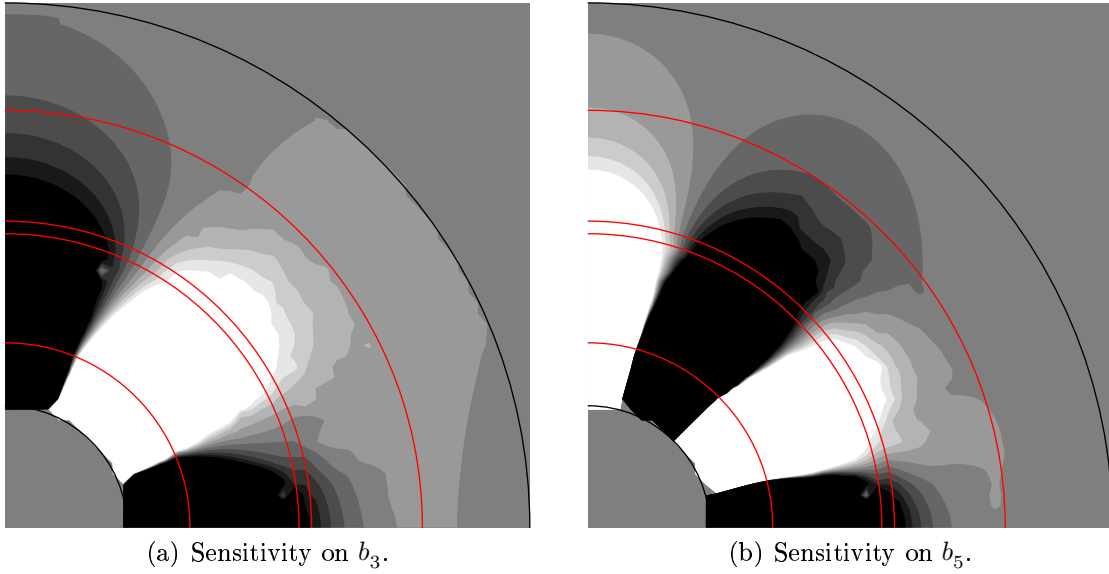


Figure 8.4: Sensitivity of the relative multipole errors b_3 and b_5 on the position of a thin ferromagnetic cylinder within the coil cross section. The dark color indicates a negative contribution, the light one a positive contribution. The circles indicate from the inside to the outside the reference radius r_0 , the aperture radius r_A , the outer radius of the inner layer, the inner radius of the outer layer r_{L2} , the outer radius of the outer layer and the inner radius of the iron yoke r_{Yi} . The calculation is carried out for radii between the reference radius and the inner yoke radius ($r_0 < r < r_{Yi}$) only.

All calculations are carried out for the coil cross section C with elliptical iron yoke. The material properties of the ferromagnetic inserts is identical to those of the iron yoke laminations.

8.4.1 Ferromagnetic Shims in Cables

As mentioned above, ferromagnetic material shows a magnetization opposite to the superconductor magnetization if exposed to the same field. By adding ferromagnetic material to the cables, the overall magnetic moment of both, the strands and the shim, could be canceled out.

A ferromagnetic shim of 20 mm width and 0.1 mm thickness is inserted between the two strand layers of the RUTHERFORD-type NED cables. Since the same cable is used for the inner and outer layer of the NED magnet, it is only possible to grade the method by the thickness of the shim.

The geometric field error including the contribution of the shims inside the cables is shown in fig. 8.5.

As a result, the relative multipole error b_3 is bend up by approximately 40 units and

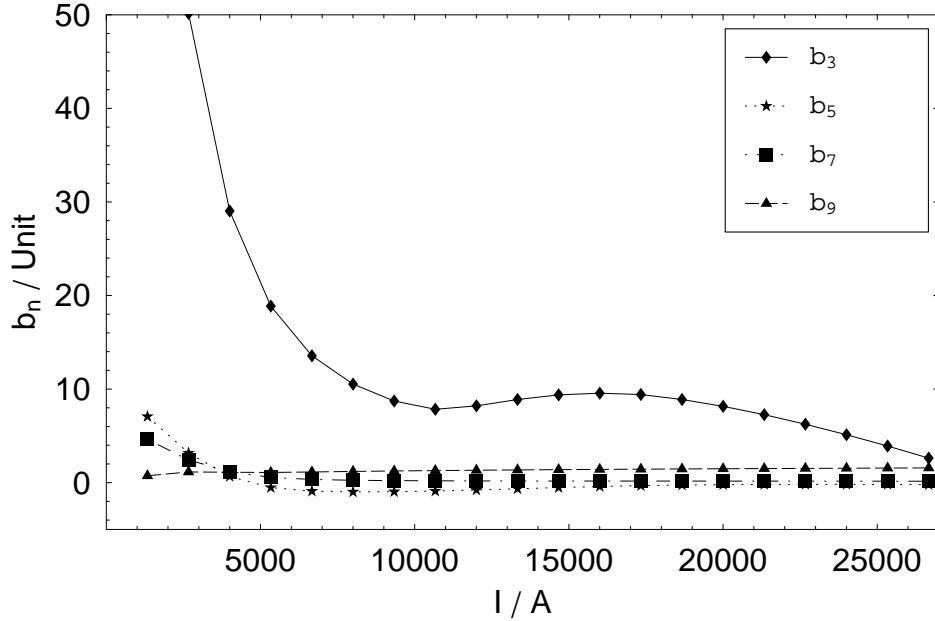


Figure 8.5: Variation of the lower order relative multipole errors due to iron saturation for the coil cross section C with elliptical iron yoke and ferromagnetic shims inside the cables. The shims are of 20 mm width and 0.1 mm thickness. They show the same permeability as the iron yoke.

would well compensate the original variation of about 40 units. The effect on b_5 is much less pronounced but nevertheless deteriorated. The effect on b_7 and b_9 is very small.

In [5], the effect of ferromagnetic shims was studied for the LHC main bending magnets for which the effect was too strong and it was assumed that for thicker strands the method would work better. The results shown in this section support this statement.

The method of ferromagnetic compensation shims inside the cables is not considered because it shows only limited possibilities for steering, the permeable material is stress sensitive and the deformation of the shims during cabling, winding and operation is unknown.

However, the deformation of the shims should show only little effect on the compensation since the local changes are small compared to the distance to the magnet center. Nevertheless, mechanically damages of the strands resulting from sharp and hard edges of the shims can not be excluded.

For the NED magnet the same cable is used for all blocks of all layers. Consequently, the ferromagnetic shims would be included in all cables in the coil cross section. Thus, steering is only possible via the geometrical size, mainly the shim thickness. However, this would have to be done during the cabling process and, once applied, does not allow any future modifications.

For the study of the effect the same permeability as for the iron yoke is assumed. In

order to stay with this example, the maximum permeability decreases with increasing stress. This would result in an inhomogeneous permeability distribution and thus decrease the effect in some areas of the coil. A feature which was not taken into account.

8.4.2 Shims on Cold Bore Tube

As shown in fig. 8.4, the area close to the reference radius and between 45° and 60° shows the required influence on the lower order relative multipole errors b_3 and b_5 . Starting from this estimation, a ferromagnetic sector is placed on the so-called cold bore tube (CBT) assumed at a radius of 42 mm.

By numerical optimization techniques the angular position and the thickness of the shim is varied until the geometric values are adequate for the compensation of the variation. The final result was found for a shim of 0.507 mm thickness between 41.73° and 60.96° . The geometric value is shown in fig. 8.6.

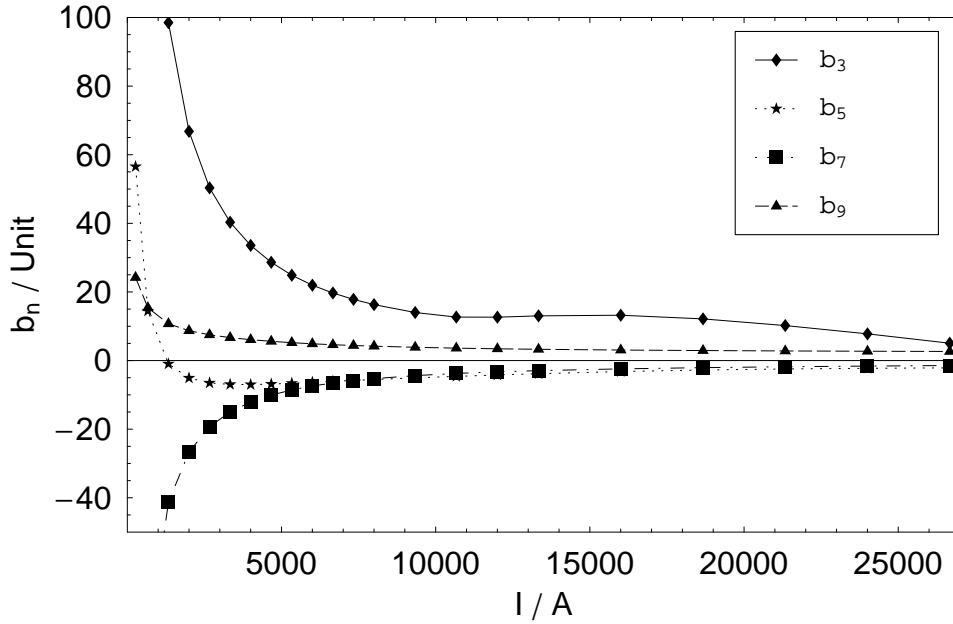


Figure 8.6: Variation of the lower order relative multipole errors due to iron saturation for the coil cross section C with elliptical iron yoke and a ferromagnetic shim on the cold bore tube. The shim is placed at an inner radius of 42 mm and covers the angular range from 41.73° to 60.96° . The thickness is 0.507 mm. It shows the same permeability as the iron yoke.

The method works well for the compensation of b_3 . The multipole error b_5 is compensated above 3 kA but shows an overall positive bending contrary to the analytical model. For b_7 the effect is negative and would further deteriorate this multipole.

By increasing the distance of the ferromagnetic sector to the magnet center the influence on the higher order multipole errors could be decreased. Therefore simulations with a ferromagnetic sector on the coil protection sheet (CPS) were carried out but showed only a very small overall effect.

The cold bore tube is inserted into the coil during pre-collaring. This causes on the one hand the problem of a precise alignment and on the other hand gives the possibility of applying compensations after production since the CBT can be exchanged without de-collaring.

8.4.3 Shims on Wedges

In [4] the compensation of persistent currents was studied by means of ferromagnetic wedges replacing the non magnetic copper wedges. The study showed a very strong effect on b_3 , much stronger than needed for the compensation.

By reducing the size of the ferromagnetic part of the wedge the saturation starts earlier and the overall effect can be reduced. For this study this is done by so-called wedge shoes², which are shims on one or both broad surfaces of the wedge.

According to fig. 8.4, the wedge shoes were applied on the wedge between blocks 2 and 3 as well as for the wedge between blocks 5 and 6. The thickness of the shims could be varied within the optimization. Starting with 4 shoes, the optimization algorithm increased the thickness of the shims above blocks 2 and 5 while the upper two were reduced to the minimum allowed size. Continuing with the two thick wedge shoes gave the results shown in fig. 8.7.

The shims are of 26.4 mm width and for the inner layer (on top of block 5) of 0.702 mm and for the outer layer (on top of block 2) of 1.5 mm thickness. The compensation of b_3 and b_5 is as required. The multipoles b_7 and b_9 are deteriorated due to the wrong orientation of the bending when the wedges are applied.

Figure 8.8 shows the simulated multipole errors including the calculation of persistent current induced field errors for the compensation with two shims.

It can be seen that the variation of b_3 is strongly reduced. The variation of b_5 is decreased and slightly over compensated. As expected, the variation of b_7 and b_9 has been amplified. Table 8.2 shows the calculated variation of the relative multipole errors.

Table 8.2: Variation of the multipole errors induced by superconductor magnetization currents on the up ramp branch. The variation from the extreme value at around 4 kA to the extreme value close to the maximum current is given.

Δb_3	Δb_5	Δb_7	Δb_9
10	5	10	7.4

²by C. VÖLLINGER

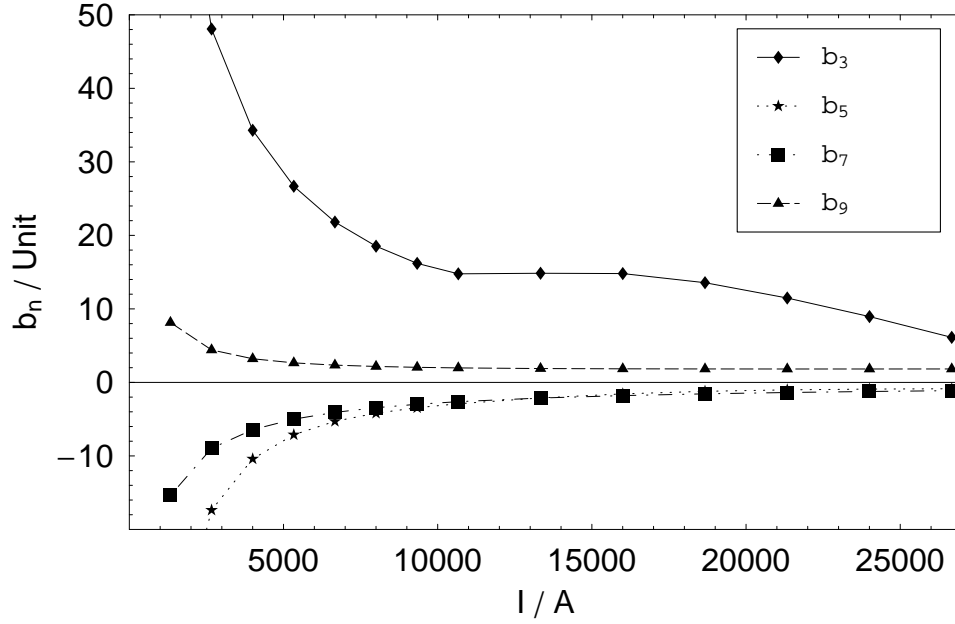


Figure 8.7: Variation of the lower order relative multipole errors due to iron saturation for the coil cross section C with elliptical iron yoke and one ferromagnetic wedge shoe on top of block 2 and one on top of block 5. The shims have a width of 26.4 mm and thickness of 1.5 mm in the outer and 0.702 mm in the inner layer.

8.5 Conclusions

Based on the estimation of the critical current density of the NED strand, a first estimation of the influence of the superconductor magnetization on the field quality could be given for the NED cable used in the $\cos\theta$ layer design.

For the study of compensation methods an analytical tool was derived, showing the local sensitivity on ferromagnetic inserts. The shown numerical results are in fair agreement with the analytical calculation. This should be further investigated.

Three common ways to compensate the persistent current induced field errors were studied for the NED cable within the $\cos\theta$ layer design:

- The results for the ferromagnetic shims inside the cables are sufficient for the compensation of b_3 but the method was not further considered due to mechanic and construction disadvantages.
- A ferromagnetic sector mounted on the cold bore tube gave an improvement for b_3 and partly for b_5 but strongly deteriorated b_7 . This method should be further investigated since the cold bore tube can be exchanged later during production.
- By inserting ferromagnetic wedge shoes into the coil cross section, the variation of the relative multipole errors b_3 and b_5 could be reduced. For b_7 and b_9 this method

8.5. Conclusions

further deteriorated the multipole values.

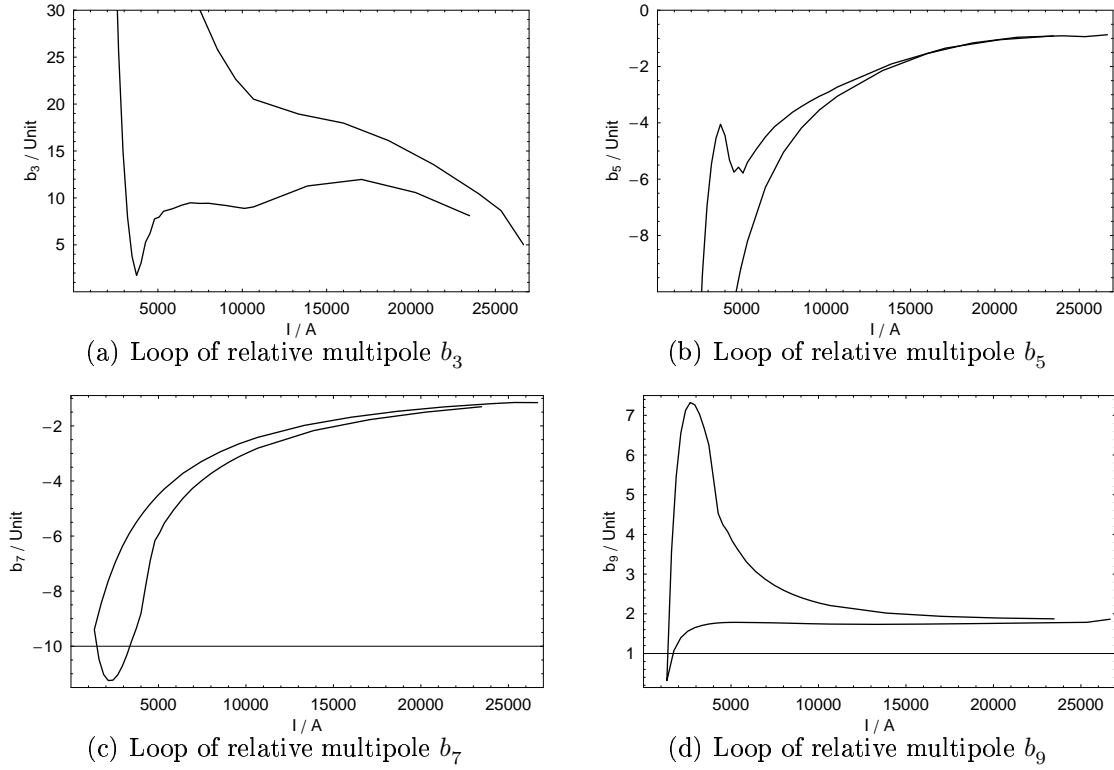


Figure 8.8: Field errors induced by the superconductor magnetization for the optimized cross section C with elliptical iron yoke and ferromagnetic shims for the compensation. The current ramp cycle is from ≈ 1.5 kA up to ≈ 27 kA and down to ≈ 1.5 kA. The variation of b_3 and b_5 could be strongly decreased on the up ramp branch above ≈ 4 kA. The cross section has not been reoptimized.

9 Conclusions

The electromagnetic design study of a 15 T large bore superconducting dipole magnet is subdivided into a theoretical preparation including analytical calculations of basic geometries and first estimations for the magnet, and into the numerical computation and optimization of the magnet cross section.

9.1 Analytical Results

By means of the field of a single line current, the harmonic multipole errors are studied, different current distributions are calculated and the effect of a circular iron yoke is demonstrated.

- The field and vector potential of the basic element of superconducting magnets, the **line current**, are calculated and expressed in terms of the FOURIER expansion for the calculation of multipole errors.
- It is shown that the number of allowed multipole errors reduces due to by **symmetries** of the current positions, and the **sensitivity of the multipole errors on the current position** is calculated. For magnetic **line dipoles** resulting from magnetization the sensitivity on the local field and the position is derived. It is shown that the **allowed multipole errors** for line currents and line dipoles are identical and only dependent on the magnet symmetry.
- The field and vector potential of the two most common ideal dipole configurations, the **intersecting circles** and the $\cos\theta$ **configuration** are calculated. From the analytic solution for a **current arc**, the field and vector potential of **symmetric current shell coils** and the so-called **No- B_3 -No- B_5 -coil** are derived.
- For an **excentric line current** the problem of three arbitrary materials with circular boundary is solved. Using this results, the iron yoke of superconducting accelerator magnets can be described by a **bore in permeable material** or a **hollow cylinder made of permeable material** and the effect on the multipole errors can be studied. This way the imaging method can be obtained for the circular bore and it can be shown how the boundary conditions can be fulfilled for a single line current inside an infinitely permeable bore without having field lines perpendicular to the boundary.

9.2 Estimations

Based on the analytical results different aspects of the superconducting magnets can be estimated:

- By means of the intersecting circle configuration the **required amount of superconductors** can be estimated depending on the desired field strength and the aperture size taking into account the characteristics of the cable used.
- From the comparison of the multipole errors resulting from a line current inside a permeable bore and from a line current inside a hollow cylinder made of permeable material, it can be estimated for which **yoke size and material** the calculations can be carried out by means of the **imaging method only**. These results are numerically confirmed.
- The so-called **saturation current**, the maximum current up to which the iron yoke can be considered as linear is estimated for a basic coil inside a circular iron yoke. This result is numerically confirmed.
- Considering a basic coil inside a hollow cylinder of permeable material, the dependence of the **stray field** on the yoke thickness and the yoke material is estimated although no saturation effects are taken into account.
- Combining the saturation history and the multipole sensitivity of line currents the effect of **modifications of the iron yoke shape** on the field quality can be estimated.
- The field of a coil cross section is calculated analytically for a circular iron yoke and the **multipole sensitivity in case of additional ferromagnetic rods** is estimated within the bore of the yoke.
- From the scaling of multipole errors to different reference radii, a new quantity for the description of the overall field quality is derived: The **good-field-radius** denoting the maximum radius where the total field quality does not exceed a certain limit.

9.3 Numerical Results

Starting from the preliminary design of the NED magnet the coil cross section and the iron yoke of the NED magnet are optimized.

- The **coil cross section** is optimized for a circular iron yoke at maximum excitation current mainly subject to the multipole errors but also to design guidelines representing a stable design.

- For the optimized coil cross section the effect of the iron saturation on the multipole errors for varying excitation current is studied. Different modifications of the **iron yoke shape** are studied in order to **reduce the multipole variation**. This includes the modification of the outer iron yoke contour, punching virtual holes into the iron laminations and the change of the inner contour to an elliptic shape. With the inner ellipse the variation of the multipole errors can be reduced best and the coil cross section is optimized for the new iron yoke¹.
- On the optimized coil cross section with elliptical iron yoke, the **effect of the superconductor magnetization** on the multipole errors is studied. Different **compensation techniques** like ferromagnetic shims inside the cables, mounted on the cold bore tube or the copper wedges are investigated.

9.4 Outlook

Further work will have to include:

- Mechanical calculations and analysis of the magnet cross section with respect to stress and deformations,
- Calculations of the quench behavior,
- 3D calculations considering the coil ends,
- eventually the stress sensitivity of the permeable material and the superconductor, and
- new results from the NED cable.

¹The resulting cross section will serve as Reference Design V. 2 within the NED collaboration.

Bibliography

- [1] A. Devred, *et al.*, “Status of the Next European Dipole (NED) Activity of the Collaborated Accelerator Research in Europe (CARE) Project,” in *Transactions on Applied Superconductivity*, vol. 15, no. 2, June 2005, pp. 1106–1112. [Online]. Available: <http://doc.cern.ch/archive/electronic/cern/preprints/at/at-2005-002.pdf>
- [2] S. Russenschuck, *et al.*, “Integrated Design of Superconducting Magnets with the CERN Field Computation Program ROXIE,” in *6th International Conference on Computational Accelerator Physics*, Darmstadt, Germany, 2000. [Online]. Available: <http://doc.cern.ch/archive/electronic/cern/preprints/lhc/lhc-project-report-446.pdf>
- [3] S. Russenschuck, *Electromagnetic Design and Optimization of Accelerator Magnets*, 2nd ed. Geneva, Switzerland: CERN, June 2005, ISBN: 92-9083-242-8.
- [4] D. Leroy and O. Vincent-Viry, “Preliminary Magnetic Designs for Large-Bore and High-Field Dipole Magnets,” CERN, Geneva, Switzerland, Tech. Rep., Dec. 2004. [Online]. Available: <http://doc.cern.ch/archive/electronic/cern/preprints/at/at-2004-022.pdf>
- [5] C. Völlinger, M. Aleksa, and S. Russenschuck, “Compensation of Magnetization Effects in Superconducting Accelerator Magnets,” in *17th International Conference on Magnet Technology MT-17*, Geneva, Switzerland, Sept. 2001. [Online]. Available: <http://doc.cern.ch/archive/electronic/cern/preprints/lhc/lhc-project-report-530.pdf>
- [6] A. Devred, *et al.*, “High Field Accelerator R&D in Europe,” in *18th International Conference on Magnet Technology MT 18*, Morioka, Japan, 2003, pp. 339–344. [Online]. Available: <http://doc.cern.ch/archive/electronic/cern/preprints/at/at-2004-010.pdf>
- [7] B. Bellesia, *et al.*, “Trends in Cable Magnetization and Persistent Currents during the Production of the Main Dipoles of the Large Hadron Collider,” in *Applied Superconductivity Conference: Harnessing the Magic ASC 04*. Jacksonville, FL, USA: CERN, Oct. 2004. [Online]. Available: <http://doc.cern.ch/archive/electronic/cern/preprints/lhc/lhc-project-report-804.pdf>
- [8] W. Buckel, *Supraleitung*, fifth ed. Weinheim, Germany: VCH Verlagsgesellschaft mbH, 1993.
- [9] K.-H. Mess, P. Schmüser, and S. Wolff, *Superconducting Accelerator Magnets*. New Jersey, USA.: World Scientific Publishing Co., 1996.

- [10] F. Trillaud, A. Devred, F. Ajela, and P. Tixador, "Experimental Investigation of the Stability of Cu/NbTi Multifilament Composite Wires," 19th International Conference on Magnet Technology MT19, Genova, Italy, Sept. 2005, submitted to IEEE Trans. Appl. Supercon. for publication.
- [11] A. Devred, P. Loveridge, and N. Schwerg, "Yoke Radii for NED," Private communication, June 2005.
- [12] A. Devred, "Practical Low-Temperature Superconductors For Electromagnets," CERN, Geneva, Switzerland, Tech. Rep. CERN-2004-006, 2004. [Online]. Available: <http://doc.cern.ch/yellowrep/2004/2004-006/p1.pdf>
- [13] L. Roebel, "Winding for electrical machines," Patent, USA, Apr. 1927, no. 18441127.
- [14] T. Bödefeld and H. Sequenz, *Elektrische Maschinen*, 7th ed. Wien, Austria: Springer, 1965.
- [15] N. Schwerg, A. Devred, and C. Völlinger, "Estimation of the Critical Current Density for the Strand Used for NED," Technical Note, CERN, Geneva, Switzerland, Sept. 2005, to be published.
- [16] F. Toral-Fernandez, "Brainstorming Meeting at RAL on 14.06.2005," NED WGMDO Minutes, NED, July 2005, minimum wedge size.
- [17] P. Loveridge, "Thermal Contraction Factors for NED," Private communication, RAL, Oxford, Great Britain, Apr. 2005.
- [18] P. Fessia, "Stress and forces in the coil cross section of superconducting magnets," Private communication, CERN, Geneva, Switzerland, Mar. 2005.
- [19] A. Devred, "Reference Radii for NED," Private communication, Feb. 2005.
- [20] C. Völlinger, "Superconductor Magnetization Modeling for the Numerical Calculation of Field Errors in Accelerator Magnets," Ph.D. dissertation, Technische Universität Berlin, CERN, Switzerland, Oct. 2002. [Online]. Available: <http://doc.cern.ch/archive/electronic/cern/preprints/thesis/thesis-2003-022.pdf>
- [21] M. N. Wilson, *Superconducting Magnets*. New York, USA: Monographs on Cryogenics, Oxford University Press, 1983.
- [22] J. P. Koutchouk, "Implications of the 'good-field-radius' for the beam," Private communication, May 2005.
- [23] S. Russenschuck, *Electromagnetic Design and Optimization of Accelerator Magnets*, 1st ed. Geneva, Switzerland: CERN, Apr. 2005, ISBN: 92-9083-242-8.
- [24] I. N. Bronstein, K. A. Semendajew, G. Musiol, and H. Mühlig, *Taschenbuch der Mathematik*, fifth ed. Thun und Frankfurt am Main, Germany: Harri Deutsch, 2000.

- [25] S. Caspi, P. Ferracin, and S. Gourlay, “The stress in graded high field Nb₃Sn dipole magnets,” 19th International Conference on Magnet Technology MT19, Genova, Italy, Sept. 2005, submitted to IEEE Trans. Appl. Supercon. for publication.
- [26] H. Henke, *Elektromagnetische Felder*, 1st ed. Heidelberg, Germany: Springer, 2001.
- [27] A. Devred and D. Trassart, “Magnetic Field Produced by a Single Current Line near or within a Ferromagnetic Cylinder or Tube,” Departmental Report, Geneva, Switzerland, July 2005. [Online]. Available: <http://doc.cern.ch/archive/electronic/cern/preprints/at/at-2005-010.pdf>
- [28] “Safety Rules for the Use of Static Magnetic Fields at CERN,” IS36 Rev. 2, Geneva, Switzerland, June 2005. [Online]. Available: https://edms.cern.ch/file/335801/3/IS36_E.pdf
- [29] J. D. Jackson, *Classical Electrodynamics*, 3rd ed. New York, USA: John Wiley and Sons, 1999.
- [30] K. Wille, *Physik der Teilchenbeschleuniger und Synchrotronstrahlungsquellen*. Stuttgart, Germany: Teubner, 1996.
- [31] C. P. Bean, “Magnetization of High Field Superconductors,” *Review of Modern Physics*, vol. 36, pp. 31–39, 1964.
- [32] N. Schwerg and C. Völlinger, “Development of a Current Fit Function for NbTi to be Used for Calculation of Persistent Current Induced Field Errors in the LHC Main Dipoles,” 19th International Conference on Magnet Technology MT19, Genova, Italy, Sept. 2005, submitted to IEEE Trans. Appl. Supercon. for publication.
- [33] H. Henke, “The magnetic energy and the vector potential,” Private communication, Nov. 2005.
- [34] O. Brüning, *et al.*, Eds., *LHC design report - The LHC main ring*. Geneva, Switzerland: CERN, 2004, vol. 1.
- [35] J. P. Koutchouk, “Comparing NED multipole errors with LHC specifications,” Private communication, June 2005.
- [36] J. P. Koutchouk, “LHC Error Table for Multipole Errors on the Main Bending Magnets,” Private communication, 2005.
- [37] N. Schwerg, “Determination of a Fit Function for the Critical Current Density for NbTi Cables used in LHC Main Bending Magnets,” Student research project, Technische Universität Berlin, Geneva, Switzerland, 2005. [Online]. Available: <http://doc.cern.ch/archive/electronic/cern/preprints/thesis/thesis-2005-020.pdf>

- [38] L. Bottura, “A Practical Fit for the Critical Surface of NbTi,” in *16th International Conference on Magnet Technology MT16*, Ponte Vedra Beach, USA, 1999. [Online]. Available: <http://doc.cern.ch/archive/electronic/cern/preprints/lhc/lhc-project-report-358.pdf>

A Theoretical Excursions

A.1 Cylindrical/Polar Coordinate System

A.1.1 Variables

$$\rho = \sqrt{x^2 + y^2}, \quad (\text{A.1})$$

$$\phi = \arctan\left(\frac{y}{x}\right) + \begin{cases} \pi & x < 0 \\ 0 & x \geq 0 \end{cases}. \quad (\text{A.2})$$

$$x = \rho \cos(\phi), \quad (\text{A.3})$$

$$y = \rho \sin(\phi). \quad (\text{A.4})$$

A.1.2 Unit Vectors

$$\mathbf{e}_\rho = \cos(\phi)\mathbf{e}_x + \sin(\phi)\mathbf{e}_y \quad (\text{A.5})$$

$$= \frac{x}{\sqrt{x^2 + y^2}}\mathbf{e}_x + \frac{y}{\sqrt{x^2 + y^2}}\mathbf{e}_y, \quad (\text{A.6})$$

$$\mathbf{e}_\phi = -\sin(\phi)\mathbf{e}_x + \cos(\phi)\mathbf{e}_y \quad (\text{A.7})$$

$$= -\frac{y}{\sqrt{x^2 + y^2}}\mathbf{e}_x + \frac{x}{\sqrt{x^2 + y^2}}\mathbf{e}_y. \quad (\text{A.8})$$

$$\mathbf{e}_x = \cos(\phi)\mathbf{e}_\rho - \sin(\phi)\mathbf{e}_\phi, \quad (\text{A.9})$$

$$\mathbf{e}_y = \sin(\phi)\mathbf{e}_\rho + \cos(\phi)\mathbf{e}_\phi. \quad (\text{A.10})$$

A.1.3 Modulus of a vector in cylindrical coordinates

$$\begin{aligned} |\mathbf{B}| &= |B_\rho \mathbf{e}_\rho + B_\phi \mathbf{e}_\phi + B_z \mathbf{e}_z| \\ &= |B_\rho (\cos(\phi)\mathbf{e}_x + \sin(\phi)\mathbf{e}_y) + B_\phi (-\sin(\phi)\mathbf{e}_x + \cos(\phi)\mathbf{e}_y) + B_z \mathbf{e}_z| \\ &= \sqrt{(B_\rho \cos(\phi) - B_\phi \sin(\phi))^2 + (B_\rho \sin(\phi) + B_\phi \cos(\phi))^2 + B_z^2} \\ &= \sqrt{B_\rho^2 + B_\phi^2 + B_z^2} \end{aligned} \quad (\text{A.11})$$

A.1.4 The Curl

For a 2D problem expressed in polar coordinates the vector potential reads $\mathbf{A} = A_z \mathbf{e}_z$ and the curl is given by:

$$\nabla \times \mathbf{A} = \frac{1}{\rho} \begin{vmatrix} \mathbf{e}_\rho & \rho \mathbf{e}_\phi & \mathbf{e}_z \\ \partial/\partial\rho & \partial/\partial\phi & \partial/\partial z \\ 0 & 0 & A_z \end{vmatrix} = \frac{1}{\rho} \frac{\partial A_z}{\partial \phi} \mathbf{e}_\rho - \frac{\partial A_z}{\partial \rho} \mathbf{e}_\phi \quad (\text{A.12})$$

A.2 Magnetic Vectorpotential **A**

A.2.1 Continuity for 2D problems

From the flux conservation law for the magnetic flux density \mathbf{B} , which is given by $\nabla \cdot \mathbf{B} = 0$, the continuity of the magnetic vector potential can be shown for 2D problems.

Considering an arbitrary area F on the boundary either between two different materials or just virtually, the flux Ψ passing through this surface is equal on both sides.

$$\begin{aligned} \Psi_1 &= \Psi_2 \\ \Leftrightarrow \iint_F \mathbf{B}_1 \cdot d\mathbf{F} &= \iint_F \mathbf{B}_2 \cdot d\mathbf{F} \end{aligned} \quad (\text{A.13})$$

where $d\mathbf{F}$ denotes the differential area element and \mathbf{B}_i is the magnetic flux density in the respective area. For 2D problems, the magnetic flux density has no z -component, thus the magnetic flux per unit length is given by the integration along the boundary line S :

$$\int_S \mathbf{B}_1 \cdot d\mathbf{s}' = \int_S \mathbf{B}_2 \cdot d\mathbf{s}'. \quad (\text{A.14})$$

The differential line element $d\mathbf{s}'$ is given by

$$\begin{aligned} d\mathbf{s}' &= d\mathbf{s} \times \mathbf{e}_z \\ &= (d\rho \mathbf{e}_\rho + \rho d\phi \mathbf{e}_\phi) \times \mathbf{e}_z \\ &= -d\rho \mathbf{e}_\phi + \rho d\phi \mathbf{e}_\rho \end{aligned} \quad (\text{A.15})$$

and thus is orthogonal to the common differential line element $d\mathbf{s}$. By inserting the magnetic vector potential \mathbf{A} this can be expressed as:

$$\begin{aligned} \int_S (\nabla \times \mathbf{A}_1) \cdot d\mathbf{s}' &= \int_S (\nabla \times \mathbf{A}_2) \cdot d\mathbf{s}' \\ \Leftrightarrow \int_S \left(\frac{1}{\rho} \frac{\partial A_{1,z}}{\partial \phi} \mathbf{e}_\rho - \frac{\partial A_{1,z}}{\partial \rho} \mathbf{e}_\phi \right) (-d\rho \mathbf{e}_\phi + \rho d\phi \mathbf{e}_\rho) &= \\ \int_S \left(\frac{1}{\rho} \frac{\partial A_{2,z}}{\partial \phi} \mathbf{e}_\rho - \frac{\partial A_{2,z}}{\partial \rho} \mathbf{e}_\phi \right) (-d\rho \mathbf{e}_\phi + \rho d\phi \mathbf{e}_\rho) &= \\ \Leftrightarrow \int_S \frac{\partial A_{1,z}}{\partial \phi} d\phi + \int_S \frac{\partial A_{1,z}}{\partial \rho} d\rho &= \int_S \frac{\partial A_{2,z}}{\partial \phi} d\phi + \int_S \frac{\partial A_{2,z}}{\partial \rho} d\rho \end{aligned} \quad (\text{A.16})$$

For a contour S from $\mathbf{s}_{\text{start}}$ to \mathbf{s}_{end} the term results to:

$$A_{1,z}(\mathbf{s}_{\text{end}}) - A_{1,z}(\mathbf{s}_{\text{start}}) = A_{2,z}(\mathbf{s}_{\text{end}}) - A_{2,z}(\mathbf{s}_{\text{start}}) \quad (\text{A.17})$$

Since the contour and therefore the two points $\mathbf{s}_{\text{start}}$ and \mathbf{s}_{end} can be arbitrarily chosen, the vector potential must be continuous for every point on the boundary $\mathbf{r}_{\text{boundary}}$:

$$A_{1,z}(\mathbf{r}_{\text{boundary}}) = A_{2,z}(\mathbf{r}_{\text{boundary}}) \quad (\text{A.18})$$

This shows the identity of the continuity of the normal flux density and the vector potential.

Note that for a discontinuity of the magnetic vector potential the curl would also cause infinitely large field strengths at the boundary.

A.2.2 Constant Offset Free of Choice

The magnetic vector potential is often used as a tool to solve magnetostatic problems. The physical relevant quantity, the magnetic flux density \mathbf{B} , is given by the curl of the vector potential \mathbf{A} :

$$\mathbf{B} = \nabla \times \mathbf{A}.$$

The magnetic flux density is independent of all constants added to the vector potential because of the derivative and thus the constant added to the vector potential is free of choice.

It is common to calculate the magnetic energy not only by means of the magnetic field but also by means of the magnetic vector potential and the current density \mathbf{J} . It shall be shown that the derivation [26] of the latter relation does not limit the freedom of choice for the constant.

The magnetic energy W_m in a volume V is given by

$$\begin{aligned} W_m &= \frac{1}{2} \iiint_V \mathbf{H} \cdot \mathbf{B} \, dV, \\ &= \frac{1}{2\mu} \iiint_V \mathbf{B}^2 \, dV \end{aligned} \quad (\text{A.19})$$

By means of the identities $\nabla \cdot (\mathbf{A} \times \mathbf{B}) = \mathbf{B} \cdot (\nabla \times \mathbf{A}) - \mathbf{A} \cdot (\nabla \times \mathbf{B})$ and $\nabla \times \mathbf{B} = \mu \mathbf{J}$ this can be written

$$W_m = \frac{1}{2} \iiint_V \mathbf{A} \cdot \mathbf{J} \, dV + \frac{1}{2\mu} \iiint_V \nabla \cdot (\mathbf{A} \times \mathbf{B}) \, dV. \quad (\text{A.20})$$

An arbitrary magnetic vector potential consisting of a constant \mathbf{A}_0 and a divergence free part \mathbf{A}^* is considered:

$$\mathbf{A} = \mathbf{A}_0 + \mathbf{A}^*.$$

Due to the linearity, the magnetic energy can be split up into the contribution of the constant and the divergence free part.

$$W_m = W_{m,0} + W_m^*.$$

Using $\nabla \times \mathbf{B} = \mu \mathbf{J}$ and $\nabla \times \mathbf{A}_0 = \mathbf{0}$ the contribution to the magnetic energy of the constant vector potential can be determined to zero [33]:

$$\begin{aligned}
W_{\text{m},0} &= \frac{1}{2} \iiint_V \mathbf{A}_0 \cdot \mathbf{J} \, dV + \frac{1}{2\mu} \iiint_V \nabla \cdot (\mathbf{A}_0 \times \mathbf{B}) \, dV \\
&= \frac{1}{2\mu} \iiint_V \mathbf{A}_0 \cdot (\nabla \times \mathbf{B}) \, dV + \frac{1}{2\mu} \iiint_V \mathbf{B} \cdot (\nabla \times \mathbf{A}_0) - \mathbf{A}_0 \cdot (\nabla \times \mathbf{B}) \, dV \\
&= 0
\end{aligned}$$

The expression for the latter energy can be expressed by the sum of a volume and a surface integral.

$$W_{\text{m}}^* = \frac{1}{2} \iiint_V \mathbf{A}^* \cdot \mathbf{J} \, dV + \frac{1}{2\mu} \iint_{\partial V} \mathbf{A}^* \times \mathbf{B} \, d\mathbf{O}$$

For geometries of zero current sum the vector potential is proportional to $1/r$ and the magnetic induction to $1/r^2$. This way, the surface integral vanishes for increasing radius and the magnetic energy is given to

$$W_{\text{m}}^* = \frac{1}{2} \iiint_V \mathbf{A}^* \cdot \mathbf{J} \, dV. \quad (\text{A.21})$$

The total magnetic energy does not depend on the constant offset and thus the constant is totally free of choice.

B Values and Constants

B.1 Linear Approximation of the Critical Current Density for LHC

Table B.1: High field approximation for the critical current density $J(B)$ for the strands of the inner cable of the LHC main bending magnets [34]. The values of the NED strand [1] are shown for comparison.

	LHC main bending magnet (inner cable)	NED
J_0 at T_0 and B_0	1433 A/mm ²	1500 A/mm ²
T_0	1.9 K	4.2 K
B_0	10 T	15 T
dJ/dB	500 A/mm ² /T	500 A/mm ² /T
Cu/nonCu	1.6	1.25

B.2 Scaled Allowed Multipole Errors for LHC

For an estimation of the multipole errors of the NED dipole it is useful to compare them with the values of the LHC main bending magnets. Since the multipole errors of LHC are not evaluated at a reference radius of 2/3 of the aperture radius, they need to be rescaled in order to obtain similar systems [35].

By using Eq. (3.13) the allowed geometric multipole errors of the LHC, which are given at a reference radius of 17 mm, are scaled to a reference radius of 2/3 of the aperture radius ($r_{\text{LHC,Aperture}} = 28$ mm).

$$B_{\text{LHC},n}(r_{\text{LHC},2/3}) = \left(\frac{2/3 \cdot 28}{17} \right)^{n-1} B_{\text{LHC},n}(17 \text{ mm})$$

Table B.2 shows the odd normal relative multipole errors as target values for the LHC main bending magnets [36] and the resulting rescaled values.

Table B.2: Relative multipole errors as target values for the LHC main bending magnets and the values rescaled to 2/3 of the aperture radius.

	Target LHC (geometric)	Rescaled (geometric)
b_3	1.33	1.60
b_5	-0.30	-0.44
b_7	0.32	0.56
b_9	0.13	0.27
b_{11}	0.53	1.35

C ROXIE

C.1 Double Bending Fit Function

The double bending fit function derived for NbTi [37] and presented in [32] was slightly adapted and used for the calculation of Nb₃Sn strands at fixed temperature.

$$J_{c,Nb_3Sn}(B) = C_0 (1 + ae^{-bB}) (1 + ce^{-dB}) \left(1 - \frac{B}{B_{c2}}\right) \quad (C.1)$$

In **ROXIE** all cable properties are defined in the so-called `roxie.cadata`-file (see appendix D). The section **REMFIT** was originally designed for the scaling power law fit [38] with 4 parameters including a temperature dependency (type 1). For this reason the interpretation of the different constants had to be changed inside the program in order to use the new fit function (type 7). Tab. C.1 shows the mapping of **ROXIE** constants to the mathematical constants in Eq. (C.1).

Table C.1: Mapping of the **ROXIE** constants to the mathematical constants of the double bending fit function.

Mathematical	ROXIE	Unit
a	GAMMA	-
b	ALPHA	1/T
c	DJCS	-
d	BETA	1/T
C_0	C0	kA/mm ²
B_{c2}	BC2	T

C.2 Added: Radial Constrain

For the design of the cable cross section of superconducting dipole magnets it is very common to aim at a layout with radially oriented conductors. From the mechanical point of view this yields a better force distribution.

In addition, the multipole errors are less affected by the iron yoke. Calculating the effect of the iron yoke by means of the so-called imaging method yields for a radial cross section also radial distributed image currents. If the angular distribution of the source currents is to minimize the multipoles, the resulting geometry shows the same behavior.

A symmetrically trapezoidal conductor shall be given. The vectors \mathbf{p}_1 and \mathbf{p}_2 point from the origin to the inner two corners. The vectors \mathbf{n}_{14} and \mathbf{n}_{23} point from these corners to the outer corners. Then the position of the center of the front edge is given by $\mathbf{p} = (\mathbf{p}_1 + \mathbf{p}_2)/2$ and the direction of the midplane is given by $\mathbf{n}_{\text{incl}} = (\mathbf{n}_{14} + \mathbf{n}_{23})/2$.

The so-called positioning angle of the center α_{center} and the inclination angle ϕ_{center} are then given by

$$\begin{aligned}\alpha_{\text{center}} &= \arccos\left(\frac{\mathbf{p} \cdot \mathbf{e}_x}{|\mathbf{p}|}\right) \\ \phi_{\text{center}} &= \arccos\left(\frac{\mathbf{n}_{\text{incl}} \cdot \mathbf{e}_x}{|\mathbf{n}_{\text{incl}}|}\right)\end{aligned}$$

where \mathbf{e}_x denotes the unit vector in x -direction. For a radial design the positioning angle and the inclination angle are the same. In this way the difference of these two gives an indicator of the misalignment δ_{center} .

$$\delta_{\text{center}} = \alpha_{\text{center}} - \phi_{\text{center}}$$

Normally the keystoneing of a cable is not ideal and thus any combination of cables to so-called blocks leads to a non-radial alignment. Taken this into account the misalignment δ_{center} is summed up over all conductors of one block in order to allow a compensation of the single misalignments. This results in blocks with a mean radial alignment.

In contrary to the positions of the conductors, the positions of the blocks are within certain restrictions independent of each other and for this reason a compensation of alignment errors is unwanted. The modulus of the alignment errors is summed and yields the total alignment error δ_{total}

$$\delta_{\text{total}} = \sum_{i=1}^N \left| \sum_{j=1}^{M_i} \delta_{\text{center}}^{i,j} \right|$$

where N denotes the number of blocks in the first quadrant, M_i denotes the number of conductors in block i and $\delta_{\text{center}}^{i,j}$ denotes the misalignment in block i and conductor j .

This value was added to **ROXIE** as **INCLM** in the **Global**-section of the objectives and can be minimized by means of the known optimization techniques.

It should be mentioned, that for commonly used layouts blocks in close vicinity to the midplane are usually not inclined and since the symmetry of upper and lower coil is not considered for the calculation, the misalignment can not be reduced to zero. This has to be considered when weighting the optimization goals.

C.3 Added: Good Field Radius

The so called good-field-radius is described in section 3.6 and was added to the **ROXIE** objectives as **GDFIER**. Unlike the theoretical introduction it is possible to change the target value. This target value has to be defined as so-called design variable **GDFIEL** and is given in units of 10^{-4} . Furthermore, a starting value **GDFSV** is required for **NEWTON**'s method which can be set to the reference radius r_0 in mm.

D ROXIE Input Files

D.1 BH-Curve

```
BHiron2
33 0.985
0.000000 0.000000
0.800000 159.200000
1.200000 294.400000
1.400000 501.300000
1.500000 795.800000
1.550000 1154.000000
1.600000 1795.000000
1.650000 2862.000000
1.700000 4383.000000
1.750000 6044.000000
1.800000 8122.000000
1.850000 10590.000000
1.900000 13160.000000
2.000000 21170.000000
2.050000 26750.000000
2.100000 33760.000000
2.150000 43800.000000
2.200000 66000.000000
2.249000 99740.000000
2.275000 120960.000000
2.300000 141210.000000
2.344300 169600.000000
2.399600 212170.000000
2.490500 283130.000000
2.562700 339890.000000
2.670600 425040.000000
2.849800 566950.000000
3.207400 850760.000000
4.278200 1702300.000000
4.813400 2128000.000000
5.705200 2837700.000000
6.418600 3405100.000000
7.488700 4256700.000000
```

D.2 Cable Definition

INSUL 1									
No	Name	1 NB_INSUL	Radial	0.0.2	'Kapton insulation				'
				Azinut	Comment				
REMFI 1									
No	Name	1 FIT1	7	3.89.2	3.538	0.527	0.991	15	18 'Fit NB3SN - see SRP '
	Type	DJSC	T_CO	Alpha	Beta	Gamma	CO	BC20	Comment
FILAMENT 1									
No	Name	1 INNER	50	31.6	FIT1	FIT1	'INNER LHC LAYER FILAMENTS		'
		fildiao	fildiai	fit	fit-		Comment		
STRAND 1									
No	Name	1 ST_CK3	1.25	1.25	100	4.2	15	1350	450 'strand for CK3
			diam.	cu/sc	RRR	Tref	Bref	Jc@BrTr	dJc/dB Comment
TRANSIENT 1									
No	Name	1 TRANS1	1E-06	1E-06	0 0 0 0 0	'LHC CABLE ISS RES			'
			Rc	Ra	Comment				
CABLE 1									
No	Name	1 CA_CK6	26	2.175	2.375	40	150	0	'for cable CK6
			height	width_i	width_o	ns	transp.	degrd	Comment
CONDUCTOR 1									
No	Name	1 CK6	1 CA_CK6	ST_CK3	INNER	NB_INSUL	TRANS1	4.2	'Nb3Sn case 6 both layers
		Type	Cable	Strand	Filament	Insul	Trans	T_o	Comment